Scuola Internazionale Superiore di Studi Avanzati - Trieste

Astrophysics Sector

Evolution of Very Low Mass Stars and Very Massive Stars in PARSEC

Thesis submitted for the degree of Doctor Philosophy

CANDIDATE

Yang Chen

SUPERVISORS

Prof. Alessandro Bressan

Dr. Léo Girardi

Prof. Xu Kong

October 2015

SISSA - Via Bonomea 265 - 34136 TRIESTE - ITALY

To all the great females caring about me

Acknowledgments

Firstly, I would like to express my deep gratitude to my supervisors Prof. Alessandro Bressan, Dr. Léo Girardi and Prof. Xu Kong, for kind mentoring, supports and encouragements, and thanks to Prof. Fuzhen Cheng for advices and encouragement. Secondly, I would like to thank all my collaborators for the fruitful accomplishment, especially, Dr. Guanwen Fang and Dr. Lulu Fan for the work on galaxies. I thank all the lecturers both in SISSA and in USTC. I also thank all the people, to whom I asked for help in my research.

It would have been much more difficult to go through the four years of my Ph.D. period, without the friends being around. Special thanks go to Dr. Zhenyi Cai for the accompany in those lonely nights and weekends in SISSA, and for improving my thesis. I would like to thank Dr. Claudia Antolini for the helps and caring. I thank Dr. Ye Luo for a lot of computational techniques. I thank all the TS play-buddies (Dr. Xiaochuan Ge, Dr. Qintao Chen, Mr. Zhongli Wen, Ms. Xiaoting Fu, Ms. Jingjing Shi, etc.), and Dr. Juan Manuel Carmona Loaiza for the nice travelings. I thank the secretaries of SISSA, especially Dr. Riccardo Iancer for prompt helps. I would like to thank the medialab people for the collaborations and playing games together.

Back to those days in Hefei, I would like to thank all the colleagues, classmates, teachers. I especially would like to thank my tutor in my bachelor study for being with me in my dark days.

Finally, I would like to thank my family and Ms. Luhua Cheng for the always supports and eternal love.

I apologize for not listing all the names of the nice people, who help me, encourage me and love me.

Publications

1. Y. Chen, A. Bressan, L. Girardi, P. Marigo, X. Kong, and A. Lanza.
   PARSEC evolutionary tracks of massive stars up to 350 $M_{\odot}$ at metallicities $0.0001 \leq Z \leq 0.04$.
   MNRAS, 452:1068–1080, September 2015.

2. Y. Chen, L. Girardi, A. Bressan, P. Marigo, M. Barbieri, and X. Kong.
   Improving PARSEC models for very low mass stars.
   MNRAS, 444:2525–2543, November 2014.

3. G.-W. Fang, M. Wang, Z.-Y. Ma, Y. Chen, and X. Kong.
   Research Progress on Extremely Red Objects at z$\sim$1.
   Chinese Astronomy and Astrophysics, 39:277–294, July 2015.

4. G.-W. Fang, Z.-Y. Ma, Y. Chen, and X. Kong.
   The Evolution of Star Formation of Galaxies in the COSMOS Field.
   Chinese Astronomy and Astrophysics, 39:307–318, July 2015.

5. G.-W. Fang, Z.-Y. Ma, Y. Chen, and X. Kong.
   Morphology and structure of BzK-selected galaxies at $z\sim2$ in the CANDELS-COSMOS field.
   Research in Astronomy and Astrophysics, 15:819–827, June 2015.

6. G.-W. Fang, Z.-Y. Ma, Y. Chen, and X. Kong.
   Morphology and structure of extremely red objects at $z\sim1$ in the CANDELS-COSMOS field.
   Research in Astronomy and Astrophysics, 15:811–818, June 2015.

7. M. Loli Martínez-Aldama, D. Dultzin, P. Marziani, J. W. Sulentic, A. Bressan, Y. Chen, and G. M. Stirpe.

O I and Ca II Observations in Intermediate Redshift Quasars.
ApJS, 217:3–31, March 2015.

8. G. W. Fang, Z. Y. Ma, Y. Chen, and X. Kong.
The Star-forming Evolution of Galaxies with Redshift in the COSMOS Field.
Acta Astronomica Sinica, 56:7–16, January 2015.

9. G. W. Fang, Z. Y. Ma, Y. Chen, and X. Kong.
Morphology and Structure of Ultraluminous Infrared Galaxies at $z \approx 2$ in the EGS Field.
Acta Astronomica Sinica, 55:458–465, November 2014.

10. F. Shi, Y.-Y. Liu, X. Kong, Y. Chen, Z.-H. Li, and S.-T. Zhi.
A support vector machine to search for metal-poor galaxies.
MNRAS, 444:L49–L53, October 2014.

11. M. L. Martínez-Aldama, D. Dultzin, P. Marziani, J. W. Sulentic, Y. Chen, A. Bressan, and G. M. Stirpe.
Low ionization lines in high luminosity quasars: The calcium triplet.
Advances in Space Research, 54:1375–1381, October 2014.

12. L. Fan, G. Fang, Y. Chen, J. Li, X. Lv, K. K. Knudsen, and X. Kong.
Structure and Morphology of X-Ray-selected Active Galactic Nucleus Hosts at $1<z<3$ in the CANDELS-COSMOS Field.
ApJ, 784:L9–13, March 2014.

13. G. Fang, J.-S. Huang, S. P. Willner, X. Kong, T. Wang, Y. Chen, and X. Lin.
Selection and Mid-infrared Spectroscopy of Ultraluminous Star-forming Galaxies at $z \sim 2$.
ApJ, 781:63–75, February 2014.

14. F. Shi, Y.-Y. Liu, X. Kong, and Y. Chen.
Artificial neural network to search for metal-poor galaxies.
A&A, 562:A36–41, February 2014.

15. F. An, X. Zheng, Y. Meng, Y. Chen, Z. Wen, and G. Lü.
The nature of [S III] $\lambda\lambda$9096, 9532 emitters at z = 1.34 and 1.23.
Science China Physics, Mechanics, and Astronomy, 56:2226–2235, November 2013.

16. L. Fan, G. Fang, Y. Chen, Z. Pan, X. Lv, J. Li, L. Lin, and X. Kong.
The Structure of Massive Quiescent Galaxies at $z \sim 3$ in the CANDELS-COSMOS Field.
ApJ, 771:L40–44, July 2013.

17. L. Fan, Y. Chen, X. Er, J. Li, L. Lin, and X. Kong.
Large size scatter of passively evolving lensed Galaxies at $z\sim2$ in CLASH.
MNRAS, 431:L15–L19, April 2013.

18. F. Shi, X. Kong, J. Wicker, Y. Chen, Z.-Q. Gong, and D.-X. Fan.
Star Formation Rate Indicators in Wide-Field Infrared Survey Preliminary Release.
Journal of Astrophysics and Astronomy, 33:213–220, June 2012.

19. G. Fang, X. Kong, Y. Chen, and X. Lin.
Passive and Star-forming Galaxies at $1.4\leq z\leq2.5$ in the AEGIS Field.
ApJ, 751:109–119, June 2012.

Abstract

During my Ph.D. study, I have been concentrating on the evolutionary tracks and atmosphere models of very low mass stars (VLMSs; $\sim 0.1 - 0.6\,M_{\odot}$) and very massive stars (VMSs; $\sim 12-350\,M_{\odot}$), based on the PAdova-TRieste Stellar Evolution Code (PARSEC).

For the very low mass models, it appeared that the previous models computed with PARSEC were unable to correctly predict some basic observational relations. These relations include the mass–radius relation and the colour-magnitude relations of cool dwarfs. We replace the approximate boundary conditions used in PARSEC with those provided by more realistic atmosphere modelling. We implement the T–τ relations from Phoenix/BT-Settl model atmospheres as the outer boundary conditions in the PARSEC code, finding that this change alone reduces the discrepancy in the mass–radius relation from 8 to 5 per cent. Furthermore, we convert the theoretical quantities to the magnitudes and colors with the stellar spectral libraries from Phoenix/BT-Settl. We compare the models with multi–band photometries of clusters Praesepe, M 67, 47 Tuc and NGC 6397, showing that the use of T–τ relations clearly improves the description of the optical colours and magnitudes. However, using both Kurucz and Phoenix model spectra, the models are still systematically fainter and bluer than the observations. We then apply a shift to the above T–τ relations, increasing from 0 at $T_{\rm eff} = 4730\,{\rm K}$ to $\sim$14 per cent at $T_{\rm eff} = 3160\,{\rm K}$, to reproduce the observed mass–radius relation of dwarf stars. Taking this experiment as a calibration of the T–τ relations, we can reproduce the optical and near-infrared CMDs of low mass stars in the old metal–poor globular clusters NGC 6397 and 47 Tuc, and in the intermediate–age and young Solar–metallicity open clusters M 67 and Praesepe. Thus, we extend PARSEC models using this calibration, providing VLMS models that are more suitable for the lower main sequence stars over a wide range of metallicities and wavelengths.

For the very massive stars, the Padova models were computed more than 20 years

ago and were not distributed to the community because suitable bolometric corrections for these models were not yet implemented. In this project, we complement the PARSEC data base with the stellar evolutionary tracks of massive stars, from the pre-main sequence phase to the central Carbon ignition. We consider a broad range of metallicities, $0.0001 \leq Z \leq 0.04$ and initial masses up to $M_{\rm ini}$=350 $M_{\odot}$. The main difference with respect to our previous models of massive stars is the adoption of a recent formalism accounting for the mass-loss enhancement when the ratio of the stellar luminosity to the Eddington luminosity, Γ_e, approaches unity. With this new formalism, the models are able to reproduce the Humphreys-Davidson limit observed in the Galactic and Large Magellanic Cloud colour-magnitude diagrams, without an *ad hoc* mass-loss enhancement. We also follow the predictions of recent wind models indicating that the metallicity dependence of the mass-loss rates becomes shallower when Γ_e approaches unity. We thus find that massive stars may suffer from substantial mass-loss even at low metallicity. We also predict that the Humphreys-Davidson limit should become brighter at decreasing metallicity. We supplement the evolutionary tracks with new theoretical bolometric correction tables, useful for comparing tracks and isochrones with the observations. For this purpose, we homogenize existing stellar atmosphere libraries of hot and cool stars (PoWR, ATLAS9 and Phoenix) and add, where needed, new atmosphere models computed with *WM-basic*. The model grids are fully adequate in mass, age and metallicity for performing detailed investigations of the properties of very young stellar systems in both local and distant galaxies. The new tracks supersede the previous old Padova models of massive stars.

Therefore, my work together with the already updated PARSEC models of the other masses could depict the full evolution of stars across the mass range from $\sim$ 0.08 $M_{\odot}$ to 350 $M_{\odot}$ and over a wide range of metallicity from super-Solar ($Z = 0.04$) to extreme metal-poor ($Z = 0.0001$). Consequently, they would provide paramount information for studies not only on stars or star clusters but also on galaxy formation and evolution.

Contents

Chapter 1

Introduction: stellar structure and evolution

As we all know the stellar mass is the key property governing the evolution of a star. The lower mass limit of the stars is about $0.08\,M_{\odot}$. This is the lowest mass required for Hydrogen burning, though Deuterium can burn in even smaller objects (e.g., brown dwarfs). The upper mass limit is still uncertain, however, studies have claimed star of initial mass $\sim 350\,M_{\odot}$ (Crowther et al. 2010; Bestenlehner et al. 2011). According to the stellar mass, stars can be roughly divided into low mass stars, intermediate stars and massive stars. Low mass stars are defined as those developing an electron degenerate Helium core after central Hydrogen burning. The maximum mass for low mass stars is about $2\,M_{\odot}$ (the Helium flash mass limit, $M_{\rm HeF}$) depending on their initial chemical composition. In low mass stars, because of the Helium core degeneracy, Helium burns in the form of Helium flash until the degeneracy is alleviated. The division between intermediate mass stars and massive stars is at $\sim 8M_{\odot}$. The distinguish is whether they experience an AGB phase. For a more detailed description of the mass division, the readers are referred to Chiosi et al. (1992).

Stars with masses close to the Sun are the best studied class relative to the others. Firstly, our Sun, benefiting from its proximity, is the preferred object for all means of observational techniques from radio to gamma-ray and, therefore, is the best understood star. Secondly, in the Solar neighbourhood, stars with masses similar to the Sun are numerous (Bastian et al. 2010) and they are more luminous compared to lower mass stars. However, there are also a lot of un-answered questions in the advanced stages of

Solar mass to intermediate mass stars, like red giant branch (RGB), Helium burning and asymptotic giant branch (AGB) phases. The study of low mass stars is hindered by the both facts that 1) they are too faint to be well observed and 2) their atmospheres are very difficult to be modelled, owing to the relatively low temperature, the deep convection envelope, as well as the presense of super-adiabatic regions above the envelope. For massive stars, modelling the mass loss is one of the most challenging issues.

During my Ph.D. study, I have been concentrating on the aforementioned two extreme mass range: very low mass ($\sim 0.1 - 0.8\,M_{\odot}$) and very massive stars ($\sim 12 - 350\,M_{\odot}$). This thesis is organized as following.

- In this chapter, I make a very brief summary of the equations for the stellar structure and evolution. Equations describing the properties of stellar matter necessary for solving these equations are then discussed. Boundary conditions and initial conditions are also introduced. Most of the material in this chapter refers to the book "Stellar Structure and Evolution" by R. Kippenhahn and A. Weigert. Afterwards, I present the main ingredients of our PARSEC code, which is the basis for our studies. Finally, some other popular evolutionary codes are discussed.

- In the next chapter, I present our work on the new evolutionary tracks for very low mass stars. In this project, we replace the approximate grey-atmosphere model with the more realistic Phoenix atmosphere models as the boundary conditions for solving the equations of the stellar structure.

- In the third chapter, I show the new PARSEC evolutionary tracks for massive stars. The novelty compared to our previous and other models is the introduction of new mass loss recipes.

- In the fourth chapter, I present the second part of my work on massive stars: modelling their atmospheres. I first introduce the stellar wind and then present our new computation of atmosphere models for massive stars with the WM-basic code. They are appropriate for main sequence stars, like O, B stars. For the Wolf-Rayet stars, the PoWR models are discussed.

- In the fifth chapter, I summarize the atmosphere models used in my research.

- In the sixth chapter, I briefly summarized my work on high-redshift galaxies and structure analysis of the galaxies.
- In the last chapter, our results are concluded.

1.1 Equations of stellar structure and evolution

Under the assumptions of spherical symmetry (neglecting rotation) and complete equilibrium (mechanical and thermal equilibrium), the equations describing the structure and evolution of stars are:

$$\text{Mass conservation:} \quad \frac{\partial m}{\partial r} = 4\pi r^2 \rho, \tag{1.1}$$

$$\text{Hydrostatic equilibrium:} \quad \frac{\partial P}{\partial r} = -\rho \frac{Gm}{r^2}, \tag{1.2}$$

$$\text{Thermal conservation:} \quad \frac{\partial L}{\partial r} = 4\pi r^2 \rho q, \tag{1.3}$$

$$\text{Radiative transfer:} \quad \frac{\partial T}{\partial r} = -\frac{3}{4ac}\frac{\kappa\rho}{T^3}\frac{L}{4\pi r^2}, \tag{1.4}$$

$$\text{Nuclear reaction:} \quad \frac{\partial X_i}{\partial t} = \frac{A_i}{\rho}(\Sigma r_{ji} - \Sigma r_{ik}), \quad i = 1, ..., I. \tag{1.5}$$

In the above equations, there contain two independent variables: the radial coordinate r and the evolutionary time t. The dependent variables to be solved are: the stellar mass m enclosed in r, the pressure P, the luminosity L, the temperature T, and the mass fraction X_i of any element i considered. In the above equations, they are written as implicit functions of r and t. The derivatives are written in partial derivatives. Other quantities are related to the properties of stellar matter: the density $\rho = \rho(P, T, X_i)$, the opacity $\kappa = \kappa(\rho, T, X_i)$, the nuclear energy generation rate q (here we ignore the gravitational energy for simplicity), the nuclear reaction rate r_{ji} between elements i and j, and the corresponding atomic mass A_i of the element i. To solve the unknown variables m, P, T, L and X_i, we need to know the above property functions of stellar matter, which will be covered in the next section. Finally, $G = 6.6738 \times 10^{-11} \mathrm{m^3\,kg^{-1}\,s^{-2}}$ is the gravitational constant, $a = 7.5657 \times 10^{-16} \mathrm{J\,m^{-3}\,K^{-4}}$ the radiation-density constant, and $c = 2.9979 \times 10^{8} \mathrm{m\,s^{-1}}$ the light velocity.

The above stellar structure and evolution equations can be divided into two categories. The first four equations describe the stellar structure, while the last one is for the evolution

of the chemical composition. Actually, the last one is a set of equations, with each sub-equation for every involved elements. As we know the pace of the evolution is controlled by the nuclear burning (although the gravitational force is the ultimate driver), if at a given time (e.g., t_0), the chemical distribution within the star (chemical profile) is given, then the first four equations can be solved to give the stellar structure (e.g., the pressure and temperature profiles). Then the chemical profile of the next step ($t = t_0 + \Delta t$) can be calculated with the results from the last step. So on and so forth, the evolutionary track of a star of given mass can be computed.

In the meantime, for solving the above partial derivative equations, we also need four "boundary conditions" for the structure equations (spatial derivative) and a set of "initial conditions" for the equations of the chemical composition (time derivative). I will introduce the boundary conditions in section 1.3 and the initial conditions in section 1.4, respectively.

Finally, the equation (1.4) is only valid for radiative regions, while in the presence of convection it has to be modified to include the convection transported flux. I will introduce the convection in section 1.2.

During the evolution of stars, their masses generally do not change in appreciable ways (e.g., the Solar wind or nuclear burning have only negligible influence on the mass), except for the massive stars and some stages of intermediate stars, such as RGB and AGB stages. In contrast, the radius of the stars would change dramatically to the extent of hundreds and even thousands of times with respect to that on the main sequence. So, it is a convention to use m (Lagrange coordinate) instead of r (Euler coordinate) as the independent variable to describe the structure of the stars. A particular example showing the advantages of using m is the description of the chemical composition. In the absence of nuclear reaction or any mixing processes, the chemical fraction of a certain type of particle $X_i(m, t)$ will remain constant during stellar expansion or contraction, while in the case of taking r as the independent variable, $X_i(r, t)$ would change. Actually, to any "mass element", a m is assigned at a given moment t_0, then this value remains for any other moment. Taking m as the independent variable, the above four equations which

involve the spatial variables become:

$$\frac{\partial r}{\partial m} = \frac{1}{4\pi r^2 \rho}, \tag{1.6}$$

$$\frac{\partial P}{\partial m} = -\frac{Gm}{4\pi r^4}, \tag{1.7}$$

$$\frac{\partial L}{\partial m} = q, \tag{1.8}$$

$$\frac{\partial T}{\partial m} = -\frac{3}{64ac}\frac{\kappa}{T^3}\frac{F}{\pi^2 r^4}. \tag{1.9}$$

By solving these equations, any stellar property (Ψ) can be expressed as $\Psi = \Psi(m, t)$, where m varies between 0 and the total mass $M_{\rm tot}$ of the star.

1.2 Properties of stellar matter

To solve the differential equations of stellar models, we need to specify some quantities describing the stellar matter. These quantities are formulated with basic variables such as P, T, and the chemical compositions X_i, under the condition of local thermodynamic equilibrium (LTE). As we know that if a system (of given chemical composition) is in thermodynamic equilibrium, then its thermodynamic properties (such as the state occupation distribution of atoms) are specified uniquely with two thermodynamic variables (e.g., temperature and pressure). In thermodynamic equilibrium, there is no net exchange of matter or energy within the system or between systems. However, we know it is not valid in the star, because there is energy flow from the stellar deep interior to the outer space (or to say, the stars have an open boundary that the photons escape into space). Despite of the failure of this global thermodynamic equilibrium, it can be approximated locally, to say LTE. Assuming that matter particles (ions, electrons, atoms, and molecules) are in LTE with each other, they can be described uniquely by the local temperature and pressure (and chemical composition). LTE simplifies the statistic calculation of the particles. The LTE is established due to collisions among particles and results in Maxwellian velocity distribution and Saha-Boltzmann statistics of the excitation and ionization of particles. The influence from the radiation field to the energy distribution is ignored. However, the radiation field is allowed to depart from LTE to allow radiation transferring out of stars. In the deep stellar interior, the interactions between particles and photons

are so intensive that the mean free path of photons is very small, thus, the energy distribution of radiation field is close to the Planckian distribution. Towards the atmosphere, the energy distribution of radiation field departs from black body distribution gradually. In the meantime, the LTE assumption is broken by the relatively increasing interactions with the radiation field, as the interactions among particles become less frequent in the atmosphere. In this case, it is called non-LTE. For example, the electron scattering with the radiation field can drive the system away from LTE. In non-LTE case, the statistic distributions of the states of the atoms/ions are affected by the radiation, and vice versa, the radiation field is also influenced by the stellar matter. So the statistical equilibrium equations are coupled with the radiation transfer equations, and they have to be solved simultaneously. Moreover, as the radiation transfers between different layers, different layers within the stellar models are coupled and have to be computed iteratively. Finally suffice it to mention that, if the interactions between stellar matter and radiation are vigorous enough (or to say the photon free path is small enough compared to the dimension of the system) that the equilibrium between them is achieved, then they have the same temperature and the radiation field is described by the black body. For example, in the stellar deep interior, LTE and black body are valid to describe the thermodynamic state. However, in the atmosphere of massive stars, because of the energetic radiation, relatively tenuous plasma and the strong stellar wind, both the assumptions have to be relaxed. For cool stars, the non-LTE effects are reviewed in Bergemann & Nordlander (2014).

In stars, the related physical components are radiation, electrons (and positrons), ions, atoms, molecules and neutrinos. Modelling the thermal-dynamical and chemical properties of stellar matter is a basic step in modelling stellar evolution. In the following I give a description of the property functions of the stellar matter.

Equation of state

The equation of state is introduced so that the density ρ can be expressed as $\rho = \rho(P, T, X_i)$ or $P = P(\rho, T, X_i)$. For an ideal gas, it is quite simple as $P = nkT = \frac{R}{\mu}\rho T$. For a completely degenerate non-relativistic electron gas, it is $P_e \propto \rho^{5/3}$. However, these idealistic EOSs are not enough for modelling the stellar interior or atmosphere. The FreeEOS by Alan W. Irwin (Irwin 2012)[1] is a more popular, realistic and complete one.

[1] http://freeeos.sourceforge.net/.

Some other EOS sources include ÆSOPUS (Marigo & Aringer 2009) at the low temperature regime, OPAL 2005 EOS (Rogers & Nayfonov 2002) (a byproduct of the opacity calculation), SCVH EOS (Saumon et al. 1995) for the low temperature range, and MHD EOS (Hummer & Mihalas 1988, and refs. thereafter). Finally, Phoenix uses an ideal EOS but contains a large number of elements and molecules (FreeEOS accounts for several non-ideal effects but includes fewer elements and only molecules that involve H and He, Dotter et al. 2008).

The effect of using different EOSs has been investigated by many authors. The most recent study concerns very low mass stars. For example, di Criscienzo et al. (2010) has shown that different EOS equations do affect the tracks of low mass stars ($M < 0.5 M_{\odot}$) with respect to that of more massive stars.

Opacity

The opacity κ is a physical quantity that describes the reduction (dI) of the radiation intensity I by the matter along the propagation path length dr:

$$dI = -\kappa I \rho dr. \tag{1.10}$$

In the stellar matter, the main sources of opacity κ are the following.

- **Electron scattering:** The opacity induced by electron scattering is independent of the frequency. It represents the basal value of the opacity in stars at temperature $\gtrsim 10^4$ K (Ezer & Cameron 1963). If the stellar matter is fully ionized then the opacity is

$$\kappa_{\nu} = \frac{8\pi}{3} \frac{r_e^2}{\mu_e m_u} = 0.20(1+X)\mathrm{cm}^2\mathrm{g}^{-1}, \tag{1.11}$$

  where r_e is the classical electron radius and m_u is the atomic mass unit (= 1amu = 1.66053×10^{-24}g). X is the mass fraction of Hydrogen. The second equality is made under the assumption that the ratio of molecular weight μ_i to the charge number Z_i $\mu_i/Z_i \approx 2$ for elements heavier than Helium (assuming fully ionized). Because of the frequency independence of the electron scattering opacity, the Rosseland mean (defined below) is the same as in equation (1.11).

- **Free-free absorption:** When a free electron passes by an ion, the system formed by the electron and the ion can absorb (or emit) radiation. The opacity resulted from this process is

$$\kappa_\nu \sim Z^2 \rho T^{-1/2} \nu^{-3}, \tag{1.12}$$

and the corresponding Rosseland mean is

$$\kappa_{\rm bf} \propto \rho T^{-7/2}. \tag{1.13}$$

It is well known as the Kramers opacity.

- **Bound-free absorption:** A bound system composed of electrons and a nucleus can absorb the radiation and releases an electron (or a successive release of electrons). The bound-free absorption opacity also takes the above Kramers opacity form, but with different coefficients and different dependence on the chemical composition as:

$$\kappa_{bf} \approx \kappa_{ff} \frac{10^3 Z}{X+Y}. \tag{1.14}$$

Compared to the bound-free absorption, the free-free absorption is more important at low metallicity.

- **Bound-bound absorption:** A bound system can absorb the radiation and an electron is excited to a higher bound state. The bound-bound absorption can become a major contributor to the opacity at $T < 10^6\,\mathrm{K}$.

- H^-: The H^- ions are formed through the reaction $H + e^- \rightleftharpoons H^-$. The dissociation energy is 0.75 eV, which corresponds to 1.65 μm. The condition for the formation of H^- is that the temperature should be $3000\,\mathrm{K} \lesssim T_{\rm eff} \lesssim 8,000\,\mathrm{K}$. The upper limit of the temperature range ensures a large amount of neutral Hydrogen, while the lower limit prevents the amount of free electrons, contributed by the metals and neutral Hydrogen, from being depleted by molecules (H_2, H_2O, etc.). The approximation form of H^- opacity is $\kappa_{H^-} \propto Z\rho^{1/2}T^9$. H^- is the major opacity source in the Solar atmosphere. H^- can be treated in the same way as normal atoms or ions, to take into account its contribution to the bound-free and free-free opacities.

- **Molecules:** In the outer atmosphere of stars with effective temperatures $T_{\rm eff} \leq 4000\,{\rm K}$, molecules dominate the opacity. Among them, the most important ones are H_2, CN, CO, H_2O, and TiO. The related transitions are vibrational and rotational transitions, as well as photon dissociation. An approximate form for the opacity of molecules is $\kappa_{\rm mol} \propto T^{-30}$. To appreciate the complexity of the molecular opacities, the reader can refer to the figure 4 of Marigo & Aringer (2009).

- **Dust:** The dust opacity contribution can be important in cool giants or supergiants. Suppose a dust particle is of size A_d and of density ρ_d, and a fraction X_d of the stellar material mass is locked in dust, then the dust opacity is:

$$\kappa_d = \left\{ \begin{array}{ll} \dfrac{3X_d}{4A_d\rho_d}, & \lambda << A_d \\ \\ \left(\dfrac{\lambda}{A_d}\right)^{-\beta}, & \lambda \geq A_d \end{array} \right\}, \tag{1.15}$$

  with $\beta = 4$ for simple Rayleigh scattering with dust particles in smooth spherical shape of constant size A_d, and $\beta \approx 1-2$ for the compound dust with a size and shape distribution (Owocki 2013; Li 2005).

- **Rosseland mean opacity:** As we have seen, only the opacity by electron scattering is frequency independent, while the others may change abruptly with the frequency. It is quite useful to define some frequency averaged opacity to evaluate the global effect to the radiation field by the stellar matter. One of the mostly used is the Rosseland opacity, which is defined as

$$\frac{1}{\kappa_{\rm Ross}} = \frac{\int_0^\infty \frac{1}{\kappa_\nu} u_\nu d\nu}{\int_0^\infty u_\nu d\nu}, \tag{1.16}$$

  where u_ν is the radiation energy density. By nature of this harmonic average, the Rosseland mean is weighted towards the frequency ranges of maximum energy flux throughput. For example, the stellar photosphere is defined at a radius where $\kappa_{\rm Ross} = 2/3$. As $e^{-2/3} \approx 0.5$, it means half of the flux can escape from this radius freely. Another often used average/representative opacity is the opacity at the wavelength of 5000 Å.

Finally, a note here is that opacity is still a source of error for modern stellar evolutionary codes. For example, a recent result from Bailey et al. (2015) has shown that

iron opacity is 30-400 per cent (wavelength dependent) higher than previously predicted, under the conditions of solar interior (1.9-2.3 million kelvin and electron densities of (0.7-4.0)$\times 10^{22}$ per cubic centimetre).

Nuclear reactions

In the following, I give a very rough summary on some of the nuclear reactions occurring in the stars. In my Ph.D. projects, the stellar models are calculated until Carbon ignition, thus suffice it to just pay more attention to the Hydrogen and Helium burning.

The basic idea of thermonuclear reactions is that particles overcome Coulomb barrier through the quantum tunnelling, which is found by G. Gamow. After the discovery of the quantum tunnelling, thermonuclear reactions were proposed to power the stars.

Because of the "strong nuclear force" between/among nucleons, the resulting particles have lower potential energy than when that they are apart at infinity. Therefore, after the particles overcome the Coulomb repulsion, they fall into the potential well and release energy in either radiation or neutrinos. The energy released depends on the mass defect between the original particles and the resulting ones:

$$E = \Delta M c^2 = \left(\sum_i M_i - \sum_j M_j \right) c^2. \tag{1.17}$$

The binding energy of a nucleus of mass M_i with Z protons (m_p) and N neutrons (m_n) can be calculated similarly:

$$E_{\rm binding} = \Big[Z m_p + N m_n - M_i \Big] c^2. \tag{1.18}$$

An instructive quantity to evaluate the nuclear energy reservoir is the binding fraction:

$$f = \frac{E_{\rm binding}}{(Z+N)}. \tag{1.19}$$

For example, the Iron nucleus ^{56}Fe has the largest binding fraction relative to the others. Thus, the lighter nuclei can release energy through fusion until the Iron, while the heavier nuclei can release energy through fission until the Iron. On the other hand, however, the nuclei with mass close to or heavier than Iron have similar binding fractions and therefore

the fission is more efficient for providing the energy as the case in the stars. On the other hand, the Hydrogen nucleus has the smallest binding fraction, and their fusion can release the most energy per unit mass. In the following, I give a very short list of the nuclear burning processes.

- **Deuterium:**

  A Deuterium ^{2}H can combine with a proton to form ^{3}He. It burns when the temperature exceeds $\sim 10^6$ K and its reaction rate is very sensitive to the temperature. The Deuterium burning can occur in protostars or in very low mass stars, as well as during the early cosmic nuclear synthesis.

- **Hydrogen:**

  In 1938, H. Bethe and Ch. Critchfield found the *pp* chain channel for the Hydrogen burning and C.F. von Weizsäcker and H. Bethe discovered the CNO cycle independently. When the temperature is above $\sim 4 \times 10^6$ K but less than $\sim 1.7 \times 10^7$ K, the Hydrogen burning through *pp* chain channel is the main source of nuclear energy in the star, while burning through CNO cycle takeovers when the temperature is hot enough. For example, in the Sun, *pp* chain is the main channel.

  Proton-proton chain: The first two steps of *pp* chain channel proceed as:

$$^1\mathrm{H} + ^1\mathrm{H} \rightarrow ^2\mathrm{H} + \mathrm{e}^+ + \nu \tag{1.20}$$

$$^2\mathrm{H} + ^1\mathrm{H} \rightarrow ^3\mathrm{He} + \gamma \tag{1.21}$$

  Thereafter, depending mainly on the temperature, there are three branches:
  *pp*I:

$$^3\mathrm{He} + ^3\mathrm{He} \rightarrow ^4\mathrm{He} + 2^1\mathrm{H} \tag{1.22}$$

  *pp*II:

$$^3\mathrm{He} + ^4\mathrm{He} \rightarrow ^7\mathrm{Be} + \gamma \tag{1.23}$$

$$^7\mathrm{Be} + \mathrm{e}^- \rightarrow ^7\mathrm{Li} + \nu \tag{1.24}$$

$$^7\mathrm{Li} + ^1\mathrm{H} \rightarrow ^4\mathrm{He} + ^4\mathrm{He} \tag{1.25}$$

*pp*III:

$$^3\mathrm{He} + ^4\mathrm{He} \rightarrow ^7\mathrm{Be} + \gamma \tag{1.26}$$

$$^7\mathrm{Be} + ^1\mathrm{H} \rightarrow ^8\mathrm{B} + \gamma \tag{1.27}$$

$$^8\mathrm{B} \rightarrow ^8\mathrm{Be} + \mathrm{e}^+ + \nu \tag{1.28}$$

$$^8\mathrm{Be} \rightarrow ^4\mathrm{He} + ^4\mathrm{He} \tag{1.29}$$

The first reaction (1.20) is the slowest and acts as the bottleneck for the Hydrogen burning. The net result of burning four protons into one ^{4}He is to release an energy of 26.731 MeV. However, due to the energy loss by neutrinos, the radiation energies released are 26.20, 25.67, 19.20 MeV for the three channels respectively. The *pp*I, *pp*II and *pp*III chains dominate at $T \sim 10 - 14 \times 10^6$ K, $T \sim 14 - 23 \times 10^6$ K, and $T \gtrsim 23 \times 10^6$ K, respectively. The relative dominance of different chains also depends on the chemical composition (e.g., availability of ^{4}He).

CNO cycle: The Hydrogen burning through the CNO cycles is illustrated as the following.

CNO cycle I ($^{12}\mathrm{C} \rightarrow ^{13}\mathrm{N} \rightarrow ^{13}\mathrm{C} \rightarrow ^{14}\mathrm{N} \rightarrow ^{15}\mathrm{O} \rightarrow ^{15}\mathrm{N} \rightarrow ^{12}\mathrm{C}$):

$$^{12}\mathrm{C} + ^1\mathrm{H} \rightarrow ^{13}\mathrm{N} + \gamma$$

$$^{13}\mathrm{N} \rightarrow ^{13}\mathrm{C} + \mathrm{e}^+ + \nu$$

$$^{13}\mathrm{C} + ^1\mathrm{H} \rightarrow ^{14}\mathrm{N} + \gamma$$

$$^{15}\mathrm{O} \rightarrow ^{15}\mathrm{N} + \mathrm{e}^+ + \nu$$

$$^{15}\mathrm{N} + ^1\mathrm{H} \rightarrow ^{12}\mathrm{C} + ^4\mathrm{He}$$

CNO cycle II $\left({}^{15}\mathrm{N} \rightarrow {}^{16}\mathrm{O} \rightarrow {}^{17}\mathrm{F} \rightarrow {}^{17}\mathrm{O} \rightarrow {}^{14}\mathrm{N} \rightarrow {}^{15}\mathrm{O} \rightarrow {}^{15}\mathrm{N}\right)$:

$$
\begin{aligned}
{}^{15}\mathrm{N} + {}^{1}\mathrm{H} &\rightarrow {}^{16}\mathrm{O} + \gamma \\
{}^{16}\mathrm{O} + {}^{1}\mathrm{H} &\rightarrow {}^{17}\mathrm{F} + \gamma \\
{}^{17}\mathrm{F} &\rightarrow {}^{17}\mathrm{O} + \mathrm{e}^{+} + \nu \\
{}^{17}\mathrm{O} + {}^{1}\mathrm{H} &\rightarrow {}^{14}\mathrm{N} + {}^{4}\mathrm{He} \\
{}^{14}\mathrm{N} + {}^{1}\mathrm{H} &\rightarrow {}^{15}\mathrm{O} + \gamma \\
{}^{15}\mathrm{O} &\rightarrow {}^{15}\mathrm{N} + \mathrm{e}^{+} + \nu
\end{aligned}
$$

CNO cycle III $\left({}^{17}\mathrm{O} \rightarrow {}^{18}\mathrm{F} \rightarrow {}^{18}\mathrm{O} \rightarrow {}^{15}\mathrm{N} \rightarrow {}^{16}\mathrm{O} \rightarrow {}^{17}\mathrm{F} \rightarrow {}^{17}\mathrm{O}\right)$:

$$
\begin{aligned}
{}^{17}\mathrm{O} + {}^{1}\mathrm{H} &\rightarrow {}^{18}\mathrm{F} + \gamma \\
{}^{18}\mathrm{F} &\rightarrow {}^{18}\mathrm{O} + \mathrm{e}^{+} + \nu \\
{}^{18}\mathrm{O} + {}^{1}\mathrm{H} &\rightarrow {}^{15}\mathrm{N} + {}^{4}\mathrm{He} \\
{}^{15}\mathrm{N} + {}^{1}\mathrm{H} &\rightarrow {}^{16}\mathrm{O} + \gamma \\
{}^{15}\mathrm{O} + {}^{1}\mathrm{H} &\rightarrow {}^{17}\mathrm{F} + \gamma \\
{}^{17}\mathrm{F} &\rightarrow {}^{17}\mathrm{O} + \mathrm{e}^{+} + \nu
\end{aligned}
$$

CNO cycle IV $\left({}^{19}\mathrm{F} \rightarrow {}^{16}\mathrm{O} \rightarrow {}^{17}\mathrm{F} \rightarrow {}^{17}\mathrm{O} \rightarrow {}^{18}\mathrm{F} \rightarrow {}^{18}\mathrm{O} \rightarrow {}^{19}\mathrm{F}\right)$:

$$
\begin{aligned}
{}^{19}\mathrm{F} + {}^{1}\mathrm{H} &\rightarrow {}^{16}\mathrm{O} + {}^{4}\mathrm{He} \\
{}^{16}\mathrm{O} + {}^{1}\mathrm{H} &\rightarrow {}^{17}\mathrm{F} + \gamma \\
{}^{17}\mathrm{F} &\rightarrow {}^{17}\mathrm{O} + \mathrm{e}^{+} + \nu \\
{}^{17}\mathrm{O} + {}^{1}\mathrm{H} &\rightarrow {}^{18}\mathrm{F} + \gamma \\
{}^{18}\mathrm{F} &\rightarrow {}^{18}\mathrm{O} + \mathrm{e}^{+} + \nu \\
{}^{18}\mathrm{O} + {}^{1}\mathrm{H} &\rightarrow {}^{19}\mathrm{F} + \gamma
\end{aligned}
$$

The last two branches are only significant in massive stars. The CNO cycle dominates over the *pp* chain at $\mathrm{T} \gtrsim 17 \times 10^{6}\,\mathrm{K}$. The reaction of ${}^{14}\mathrm{N} + {}^{1}\mathrm{H} \rightarrow {}^{15}\mathrm{O} + \gamma$ is the slowest (bottleneck). So nearly all the initial C, N (${}^{13}\mathrm{N}$ and ${}^{15}\mathrm{N}$) and O are transformed into ${}^{14}\mathrm{N}$. The energy produced in a whole cycle is 24.97 MeV. For our Sun, the central

temperature is of $\sim 15.7 \times 10^6$ K, thus only a very small fraction of the energy comes from the CNO cycle. The CNO cycle has a very strong temperature dependence with a power to > 13.

- **Helium & α elements:**
  Only stars with mass $\gtrsim 0.5\, M_\odot$ have enough core temperature to burn Helium. Those with a temperature below this threshold end their lives with Helium cores. Helium burns successively into Carbon, Oxygen, Neon, Magnesium, etc. Specifically, the reaction of Helium into Carbon is called *triple-alpha reaction*. It occurs at temperature $\gtrsim 10^8$ K. For every ^{12}C formed, 7.275 MeV energy is released, which is much smaller than the Hydrogen burning per unit mass. Once enough Carbon is built up through the triple-alpha reaction, ^{16}O can be formed by α capture. Then ^{20}Ne can be formed by the further α capture of ^{16}O. In principle the α capture reaction can proceed until ^{60}Zn is formed. However, those reactions beyond Neon are at a very low rate under the typical temperature and density conditions of stars. The elements produced "mainly" by the alpha (^{4}He) capture reaction, are called α elements. These elements generally include (C, O), Ne, Mg, Si, S, Ar, Ca, Ti ($Z \leq 22$). However, since C and O can also be produced by other reactions, some people do not think them as α elements. The definition may also depend on the metallicity when the elements are produced. For example, in low-metallicity stars, O is an α element. The α elements are synthesized prior to the Silicon fusion (into Iron), a precursor to type II Supernovae. Thus, they are indicators of massive star nucleo-synthesis.

- **Carbon, Neon, Oxygen and Silicon:**
  After the central Helium burning, the stellar cores are left with Carbon and Oxygen. When the temperature ($\gtrsim 5\times10^8$ K for Carbon, $\gtrsim 1.2\times10^9$ K for Neon, and $\gtrsim 1.5\times10^9$ K for Oxygen) or density is high enough, Carbon, Neon and Oxygen burning can occur successively. The end products of Carbon burning are mainly Oxygen, Neon, Magnesium and Silicon. After the Carbon core burning, an Oxygen-Neon-Magnesium core is built up, while after core Oxygen burning a large amount of Silicon is found. Finally, when Silicon is accumulated in the core and the temperature exceeds $\sim 2.7 \times 10^9$ K, Silicon starts to burn. Once Silicon has burnt into Iron, no further fusion is possible, as we know ^{56}Fe has the largest binding energy. Then the star may explode as Type II Supernovae.

- **Electron screening:**

  As we said, the nuclear reaction is enabled through overcoming the Coulomb barrier. The electrostatic force between two nuclei is $Z_1 Z_2 e^2 / r_{12}^2$. In stellar interiors, the plasma density is very high that, even the ions are fully ionized, the average distance between a nucleus and neighbouring electrons and nuclei is very small. Therefore, the nucleus is screened by electrons, and the Coulomb barrier between two nuclei is effectively reduced. This effect should be taken into account, especially in the low energy regime.

- **Resonant nuclear reaction:**

  In general, the cross-sections for the nuclear reactions increase with increasing energy of the relative motion between the involved particles. However, there are also some quasi-stationary energy levels where the compound nucleus from the original particles can easily form, which is called resonant reactions. So, superimposed on the smooth continual function of cross-section versus energy are some strong resonant peaks. This brings large uncertainties on measuring the cross-sections.

In present-day stellar evolutionary codes, the uncertainties resulted from nuclear reactions are negligible. However, the only uncertain major reaction worth mentioning is $^{12}\mathrm{C}(\alpha,\gamma)^{16}\mathrm{O}$, whose cross-section has an uncertainty by a factor of ~ 2. This uncertainty affects the nucleosynthesis yields of massive stars (Greggio & Renzini 2011).

Convection, mixing, & diffusion

- *Convection:* It is well known, convectively instable regions are present in the cores of massive stars and in the envelopes of low mass stars, while very low mass stars ($\lesssim 0.25 M_\odot$) can be almost fully convective. Let's consider a mass "element" which moves upward from its equilibrium position because of a certain fluctuation, but maintains pressure equilibrium with the surrounding matter. If after a small distance, the buoyancy diminishes, the region is dynamically stable and the element is pulled back to its equilibrium position. On the contrary, if the buoyancy pushes it even further, then the region is dynamically instable and macroscopic matter motions (convective motions) set in. It is possible to show that convection is a means of energy transport, because, while there is no net transfer of matter across any ideal surface ($\delta(\rho v) = 0$), velocities and temperature fluctuations are positively correlated so that the average quantity

which expresses the heat flow across the unit surface, $C_P \rho v \delta T \geq 0$ is positive. In the deep stellar interiors, owing to the high densities, convection is very efficient. On the surface, the density is very low and convection (if presents) may be quite inefficient. A result of the commonly adopted theory to deal with convection, the Mixing Length Theory (MLT; Böhm-Vitense 1958, but see Arnett et al. (2015) for the most recent alternative approach), states that in the deep interior the average gradient of matter is practically the adiabatic one ($\nabla = \nabla_{\rm ad}$ in the usual notations), while in the inefficient regions it is comprised of the adiabatic one and the radiative one. The latter is a fictitious gradient that is necessary for radiation to account for the whole energy flux, thus $\nabla_{\rm ad} \leq \nabla \leq \nabla_{\rm rad}$. In the latter case we speak of super-adiabatic convection.

There are two oft-used criteria for checking if the "element" is stable against convection. One is the Schwarzschild criterion (Schwarzschild 1958) and the other one is the Ledoux (Ledoux 1947). Assuming that a mass element experiences adiabatic process, in a region of homogeneous chemical composition, the Schwarzschild criterion for convective stability is:

$$\nabla_{\rm rad} < \nabla_{\rm ad}, \tag{1.30}$$

where,

$$\nabla_{\rm rad} \equiv (\frac{d \ln T}{d \ln P})_{\rm rad} = \frac{3}{16 \pi a c G} \frac{\kappa l P}{m T^4}, \tag{1.31}$$

and

$$\nabla_{\rm ad} \equiv (\frac{d \ln T}{d \ln P})_{\rm ad} = \frac{P \delta}{T \rho c_P}. \tag{1.32}$$

A note here is that $\nabla_{\rm rad}$ is linked to the spatial derivative in the star, while $\nabla_{\rm ad}$ is the thermal variation of the same mass element during a process of adiabatic compression. In a chemically inhomogeneous region, the Ledoux criterion for convective stability is:

$$\nabla_{\rm rad} < \nabla_{\rm ad} + \frac{\phi}{\delta} \nabla_\mu, \tag{1.33}$$

where, $\phi \equiv (\frac{\partial \ln \rho}{\partial \ln \mu})$ and $\delta \equiv -(\frac{\partial \ln \rho}{\partial \ln T})$. Depending on the sign of ∇_μ, the second term on the right-hand size could act as a stabilizing or de-stabilizing factor. Note also that all the above gradients can be computed from the local thermodynamic and structural properties at any point of the star, and, for this reason, the above criteria for instability are local criteria. These criteria assume that the mass element does not

exchange heat with the surrounding matter. Suppose the element oscillates around its equilibrium position and radiates energy to its surrounding when it moves upward. Then under certain circumstances ($\nabla_\mu > 0$ is large enough and $\nabla_{\rm element} - \nabla_{\rm surrounding} < 0$, but (1.33) is still satisfied), the amplitude of the oscillation can become larger and larger, and instability emerges. This is called vibrational instability. The vibrational instability does not occur in chemically homogeneous region. The energy transportation or mixing through vibrational instability is less efficient compared to convection. In stellar evolution modelling, a semi-convective mixing region is often defined outside the convective core for massive stars (Spruit 2013; Zaussinger & Spruit 2013). It is interpreted as a result of vibrational instability (Noels 2015).

- *Mixing-length theory:* Convection is not only one of the main energy transport mechanisms, but also mixes the chemical compositions. In the main stellar evolutionary phases (i.e., central H-and He-burning), convective mixing may be very fast compared to the change brought by the majority of nuclear reaction. Thus, under these circumstances, convective regions are assumed to be chemically homogeneous. Through mixing, the opacities, thermodynamical properties and nuclear reaction rates are changed, therefore, the stellar structure and evolution are changed, correspondingly.

  Convective heat transport and mixing are two difficult processes to be modelled because they are produced by the same physical process, but operate on the opposite sides of a wide range of scales. In our current understanding, heat transport is mainly provided on the largest scales while mixing occurs on the smallest ones. Furthermore, there may be strong radiative losses that render the efficiency of convection very difficult to be modelled. A recent paper by Arnett et al. (2015) summarizes the reasons of these difficulties. For these reasons, in present-day stellar evolutionary codes, the semi-empirical mixing-length theory by Böhm-Vitense (1958) is still the most popular one. The basic idea is that on average, the fluid elements travel over their mean free path and then dissolve into the surrounding medium. This mean free path $l_{\rm MLT}$ is called the mixing length. It is parameterized in units of the pressure scale as $l_{\rm MLT} = \alpha_{\rm MLT} H_P$. With this mixing length parameter $\alpha_{\rm MLT}$, the convective flux can be analytically formulated and be inserted into the equation (1.9). The mixing length has to be determined through comparison with the observations.

- *Overshooting:* As already noted, the above criteria for convective instability are local criteria. However, when the convective elements reach the border of the unstable region, their velocity is not zero. They will cross the border to a certain distance before being eventually mixed with the surrounding. This phenomenon, called overshooting (e.g., Bressan et al. 1981), is generally modelled with a parameter indicating the size of the mixed stable layers in units of the pressure scale H_P. The main effect is that with larger overshooting, there is more material available for the central Hydrogen burning. Thus, the star will stay longer on the main-sequence. During the core Helium burning phase, the blue loops are inhibited by a sizable core overshooting (Bertelli et al. 1985). However, an amount of envelope overshoot helps the development of the blue loops (Alongi et al. 1991a).

- *Diffusion:* Diffusion is a macroscopic process that can redistribute the chemical composition in the stars. There are three types of diffusion: 1) concentration diffusion, caused by abundance gradients; 2) temperature diffusion, by which heavier atoms migrate towards higher temperature regions; 3) pressure diffusion, also called sedimentation or gravitational settling, by which heavier elements migrate towards higher pressure regions. In the outer layers of the star radiative levitation is another process that may counteract sedimentation (Zemskova et al. 2014). Furthermore, it should be noted that some slow (compared to hydrostatic time-scale) mixing processes are also modelled as a diffusive process, e.g., semi-convection (Spruit 2013; Zaussinger & Spruit 2013), diffusive overshoot (Herwig 2000) and rotational mixing (Meynet & Maeder 1997, and refs. thereafter). A nice example on how to observationally determine the value of the diffusion with the star cluster NGC 6397 is provided by Korn et al. (2006).

1.3 Boundary conditions

The solution of equations (1.6)–(1.9) requires four boundary conditions. One of the major problem in stellar models is that the boundary conditions are set at the two opposite sides, that is, we have to deal with a two boundaries problem. Two of the boundary conditions

are naturally set in the stellar center, with

$$m = 0: \qquad r = 0; \tag{1.34}$$

$$m = 0: \qquad F = 0, \tag{1.35}$$

while the other two need to be found in the outer surface. The simplest forms of the latter conditions for isolated stars are:

$$m = M: \qquad P = 0; \tag{1.36}$$

$$m = M: \qquad T = 0. \tag{1.37}$$

However, these conditions are of little use and a better way is to define them at a typical radius which has some observational counterparts. This is the so-called 'photospheric' radius which divides the star into its interior region and its outer stellar atmosphere. At this radius, the stellar interior model can match the structure resulting from stellar atmosphere models. For example, the radius can be defined as the radius where the Rosseland mean optical depth $\tau_{\rm Ross}$ in a given atmosphere model equals to 2/3 (e.g., VandenBerg et al. 2008a):

$$\tau_{\rm Ross} \equiv \int_R^\infty \kappa_{\rm Ross} \rho dr = 2/3. \tag{1.38}$$

Then at this radius, the boundary conditions can be set as

$$T = T(\tau_{\rm Ross} = 2/3); \tag{1.39}$$

$$P = P(\tau_{\rm Ross} = 2/3). \tag{1.40}$$

From the atmosphere models, people can compute the $T(\tau_{\rm Ross} = 2/3)$ and $P(\tau_{\rm Ross} = 2/3)$. A common practice to derive the surface temperature and pressure is to skip the radiative transfer integration by using a relation obtained from atmosphere models (e.g., a T–τ relation), and integrate the hydrostatic equation from $\tau = \infty$ to $\tau = 2/3$. This avoids dealing with the complex problem of calculating stellar atmosphere models, that are generally computed by different groups. The most simplified case of T–τ relation is the Eddington gray body one. Under the assumption of gray body, the optical depth and the emissivity are independent of the frequency. With this approximation, one can solve the

radiative transfer equation to obtain:

$$T(\tau)^4 = \frac{3}{4}T_{\rm eff}^4(\tau + \frac{2}{3}). \tag{1.41}$$

The exact solution for the gray body is

$$T(\tau)^4 = \frac{3}{4}T_{\rm eff}^4(\tau + q(\tau)), \tag{1.42}$$

where $q(\tau)$ is the Hopf function. The value of $q(\tau)$ is listed in the Table 3-2 of Mihalas (1978). Under the assumption of gray body, the T–τ relation is independent of metallicity, or to say the properties of the underlying material. The hydrostatic equation is then solved by assuming "plane parallel model", which gives

$$\frac{dP}{dr} = -\rho\frac{GM}{R^2}, \tag{1.43}$$

where, M and R are the mass and radius of the star, respectively, and are going to be assumed constant in the integration. By utilizing the definition of τ ($d\tau = -\kappa\rho dr$), we can get

$$dP/d\tau = GM/\kappa R^2 = g_{\rm surf}/\kappa, \tag{1.44}$$

where $\kappa = \kappa(P, T, Z)$ is the opacity. When $\tau \to 0$, $P = P(\tau \to 0) = P_{\rm rad} = \dfrac{aT^4(\tau \to 0)}{3}$, (at locations far away from the star, density is very low, so radiation pressure dominates).

Thus, P_R can be obtained through integration. By using the T–τ relation, we can get the two boundary conditions at the photosphere:

$$T_R = T(\tau = \tau(R)), \tag{1.45}$$

$$P_R = P(\tau = \tau(R)). \tag{1.46}$$

With the advent of more powerful computers, more realistic stellar atmosphere models are being computed and used. This topic will be discussed in detail in chapter 2.

1.4 Initial conditions and time evolution

The equations of the stellar structure contain the time derivative in two distinct terms. One is the gravitational energy source term arising from the first principle of the thermodynamics during the slow expansion or contraction phases. In these phases, the hydrostatic (in mere generality LTE) equilibrium is supposed to hold. But, in a given layer, there must be a balance between the internal energy, the heat flow (gained or lost) and the work:

$$dQ/dt = dU/dt + PdV/dt, \tag{1.47}$$

with dQ/dt being $\epsilon_{\rm nuc}$-$\epsilon_{\rm neutrino} - dL/dm$ and these quantities being per unit mass. Thus, we have the complete equation for the energy conservation:

$$\frac{dL}{dm} = \epsilon_{\rm nuc} - \epsilon_{\rm neutrino} - \frac{dU}{dt} - \frac{PdV}{dt} \tag{1.48}$$

$$= \epsilon_{\rm nuc} - \epsilon_{\rm neutrino} - \frac{C_v dT}{dt} - \frac{Pdm}{\rho dt}. \tag{1.49}$$

The case where time derivative is needed concerns the chemical equation (1.5). As we have already seen, solving the structure at continuous time steps provides the evolution of a star of given mass. This requires an initial model to be set up at the beginning of the evolutionary track calculation. This is generally done by using analytical approximations or, more simply, by taking tabulated homogeneous chemical composition models either on the main sequence or, better, starting from the pre-main sequence phase where the central temperature and densities are so low that nuclear reactions are not important. Then the evolution is driven by contraction and eventually by nuclear burning which changes the chemical composition within the star. We will see that in more massive stars or in other phases where mass-loss is important, another time dependent quantity is the total mass of the star.

1.5 The ingredients of PARSEC stellar evolutionary code

The recent PAdova-TRieste Stellar Evolution Code (PARSEC) (Bressan et al. 2012) is a thorough revision and update of the stellar evolution code used in Padova for decades.

The original 'Padova' code has been developed since Bressan et al. (1981) and the results have been widely used in the community since then. In the following, I will briefly describe the main ingredients of the PARSEC code. Most of the following description is based on Bressan et al. (2012); Chen et al. (2014a) and Chen et al. (2015), if not specified explicitly. For completeness, I also anticipate here some of the achievements of my thesis work, that will be discussed in detail in the following chapters.

Model coverages

The computed masses range from $0.1\,M_{\odot}$ to $350\,M_{\odot}$. The main models are presented in Bressan et al. (2012), while the new very low mass models are improved in Chen et al. (2014a) and very massive star models are presented in Chen et al. (2015). The metallicities are available over $0.0005 \leq Z \leq 0.07$ as specified in Bressan et al. (2012). Models are also available for several α enhancement values. Evolutionary phases are extended from pre-main-sequence to Carbon ignition.

Solar models

Comparing Solar models with the observations is necessary to check the quality of the codes and the input physics, and to calibrate some free parameters like the mixing length parameter and the size of overshoot at the base of the convective envelope. The Michelson Doppler Imager (MDI) data set from Basu et al. (2000) is used for the Solar model calibration in PARSEC, which ensures the reliability of PARSEC.

Solar abundance

The Solar abundance is taken from Grevesse & Sauval (1998) with revision from Caffau et al. (2011). In table A.2, I give a list of the abundance used in PARSEC, as well as some popular abundance compilations. According to this compilation, the present day Solar metallicity used in PARSEC is $Z_{\odot} = 0.01524$. The initial Helium content at varying metallicity is determined by $Y = Y_{\rm p} + 1.78 \times Z$, with $Y_{\rm p} = 0.2485$ taken from Komatsu et al. (2011).

A related issue is the α-enhanced mixtures. For a given [α/Fe] ratio, there are two options to built the chemical mixture: 1) keeping the ratio [Fe/H] fixed while increasing the absolute abundances of the α elements. This leads to a net increase of the total

metallicity; 2) keeping the total metallicities fixed, while decreasing Iron-group elements and increasing the α elements to reach the desired [α/Fe] ratio. In PARSEC we opt for the second option.

Equation of State

The public available FreeEOS[2] code by Alan W. Irwin is used in PARSEC to compute the equation of state (EOS). The FreeEOS code has been fully implemented into PARSEC code, thus, the EOS can be calculated "on-the-fly". However we proceed by pre-computing some suitable tables and then interpolate among them, since the accuracy of these tables is sufficient enough for our purposes. These pre-computed tables are computed for specified chemical distribution of the elements and metallicities over suitably wide ranges of temperature and pressure. Then multi-dimension interpolations in Z, X, Y and Carbon-Oxygen combinations are applied. The accuracy of using pre-computed tables has been ensured by comparing the tracks to those computed with the "on-the-fly" EOS.

Opacity

The opacities from the OPAL group[3] (Iglesias & Rogers 1996) are used at the temperature range $4.2 \leq \log(T/\mathrm{K}) \leq 8.7$, while at $3.2 \leq \log(T/\mathrm{K}) \leq 4.1$, those from AESOPUS[4] (Marigo & Aringer 2009) are used. In the transition region of $4.0 < \log(T/\mathrm{K}) < 4.1$, a linear interpolation is adopted. Within these temperature and sufficiently large density ranges, Rosseland mean opacity tables $\kappa_R(\rho, T)$ are computed for specified abundance combinations (with the consideration of α enhancement/depletion). Then interpolation in R ($\equiv \rho/T/10^6$ in $\mathrm{g\,cm^{-3}}$), T, X, Y, and R_C ($\equiv X_C/(X_C + X_O)$) is applied. Finally, conductive opacities are included following the description from Itoh et al. (2008).

Nuclear reaction rates

The major nuclear reactions are considered for 26 elements from ^{1}H to ^{26}Si, plus D, ^{26}Al^m, ^{26}Al^g. The nuclear reaction data is from the updated JINA REACLIB Database[5] (Cyburt et al. 2010). Electron screening factors for all reactions are from Dewitt et al. (1973) and

[2] http://freeeos.sourceforge.net/
[3] http://opalopacity.llnl.gov/
[4] http://stev.oapd.inaf.it/cgi-bin/aesopus
[5] http://groups.nscl.msu.edu/jina/reaclib/db/.

Graboske et al. (1973). Finally, electron neutrino energy losses are computed following Munakata et al. (1985), Itoh & Kohyama (1983) and Haft et al. (1994).

Convection and overshooting

Convection in PARSEC is described by means of the mixing-length theory (MLT; Böhm-Vitense 1958). In the MLT, a convective element travels over a distance $l_{\rm MLT}$ from its initial position, before completely dissolving into its surroundings. $l_{\rm MLT}$ is expressed as $l_{\rm MLT} = \alpha_{\rm MLT} H_p$, with H_p being the pressure scale height and $\alpha_{\rm MLT}$ the mixing-length parameter. The mixing length parameter has been calibrated by means of a Solar model tested against the helioseismologic constraints (Basu et al. 2009) and its value is $\alpha_{\rm MLT} = 1.74$. To test the stability of radiative zones against convection we adopt the Schwarzschild criterion (Schwarzschild 1958). In the presence of a gradient of chemical composition, an alternative criterion is that of Ledoux (Ledoux 1947). This condition may appear during the evolution of massive stars, when the convective core grows in mass or when an intermediate radiative region of varying chemical composition becomes unstable to the convection. In PARSEC, we opt for the Schwarzschild criterion because, on one side it has been shown that it is the more appropriate one to account for the effects of thermal dissipation (Kato 1966) and, on the other, the presence of a sizable overshooting region from the convective core significantly reduces the differences between models computed with the two alternative criteria (Meynet & Maeder 2000).

Overshooting from the convective core is estimated within the framework of the mixing-length theory, allowing for the penetration of convective elements into the stable regions (Bressan et al. 1981). The adopted mean free path of convective elements *across* the border of the unstable region, $l_{\rm c}$=$\Lambda_{\rm c} H_{\rm P}$ with $\Lambda_{\rm c} = 0.5$, is calibrated on the colour-magnitude diagram of intermediate age clusters (Girardi et al. 2009) as well as on individual stars (Kamath et al. 2010; Deheuvels et al. 2010; Torres et al. 2014). We also account for overshooting at the base of the convective envelope, which is simply modelled by mixing the radiative region down to a distance of $l_{\rm e} = \Lambda_{\rm e} H_P$, with $\Lambda_{\rm e} = 0.7$, from the formal Schwarzschild border (Alongi et al. 1991b). We stress that the extent of the overshooting regions and the corresponding mixing efficiencies are still a matter of debate. Concerning the core overshooting, a recent analysis of the period spacing of gravity modes in low mass Helium burning stars, suggests a quite sizable overshooting region, $\Lambda_{\rm c} = 1.0$

in the above formalism (Bossini et al. 2015). Concerning envelope overshooting, work in progress (Tang et al. (2014) and Rosenfield et al. in preparation) already indicates that using larger values of l_e (close to 2 H_P) at the bottom of the convective envelope fits better the extended blue loops seen in metal-poor dwarf galaxies. Therefore, future releases of the PARSEC database are likely to have these prescriptions revised.

Mass loss rate

Regarding the massive stars, the main update with respect to previous PARSEC code is the treatment of the mass loss rate. I will discuss the mass loss rate recipes in section 3.2. Here I just give a summary. Relations from Vink et al. (2000, 2001) are used for blue supergiant phase with $T_{\rm eff} \geq 12000\,K$; and de Jager et al. (1988) formulations are used for red supergiant phase ($T_{\rm eff} < 12000\,K$). A metallicity dependence as $\dot{M} \propto (Z/Z_\odot)^{0.85} M_\odot/yr$ is adopted for them. For WR stars, Nugis & Lamers (2000) formalism is used, in which a metallicity dependence is also provided. Besides them, new results from Gräfener & Hamann (2008) and Vink et al. (2011) are utilized to include the effects of evolution at near-Eddington luminosity. Their results have shown that the mass loss rate is strongly enhanced when Γ_e, the ratio of the stellar luminosity to the Eddington luminosity, approaches unity. With this recipe, we can easily reproduce the observed Humphreys-Davidson limit (HD limit, Humphreys & Davidson 1979, a forbidden region within which only very few stars are observed in the HR diagram of the Galactic and LMC massive stars). Furthermore we use their results to describe how the dependence on the metallicity changes with Γ_e. As shown by Gräfener & Hamann (2008), when the stellar luminosity approaches the Eddington luminosity, the mass loss rate becomes almost independent of metallicity.

Boundary conditions

The original PARSEC code made use of the gray atmosphere approximation (Mihalas 1978) to determine the external boundary conditions. In this approximation, the relation between the temperature and Rosseland mean optical depth τ across the atmosphere, T–τ, is given by

$$T^4(\tau) = \frac{3}{4} {T_{\rm eff}}^4 \left[\tau + q(\tau)\right], \tag{1.50}$$

where $q(\tau) \approx 2/3$ is the Hopf function. As we will see in the chapter 2, part of my thesis work was to improve upon these simple boundary conditions. However the result occurred to be inadequate, especially in the domain of very low mass stars.

Density inversion

A particular result of requiring the models to strictly obey the hydrostatic equilibrium is that, under certain circumstances, a density inversion may occur just below the photosphere (Alongi et al. 1993; Maeder 1992). This happens at effective temperatures of about 8,000K, when the envelope temperature causes the Hydrogen ionization peak to appear in regions where convective energy transport is inefficient and radiative pressure is important. The opacity reaches a sharp peak and the radiative pressure gradient ($dP_{\rm rad}/dr$) can be very large. Hydrostatic equilibrium requires $\frac{dP_{\rm gas}}{dr} = -\frac{dP_{\rm rad}}{dr} - g\rho$. So if $-\frac{dP_{\rm rad}}{dr}$ is large enough (at the outer edge of the opacity peak, $dP_{\rm rad}/dr$ is a large negative value) to overcome the gravity force, then the gas pressure gradient $\frac{dP_{\rm gas}}{dr}$ must be positive. According to $P = \rho kT$ and since dT/dr must be negative to drive radiation outward, $d\rho/dr$ must be positive, and density decreases with decreasing radius. It is not clear how one can deal with this density inversion problem, which may also cause some difficulties in numerical convergence. Because a density inversion in a gravitational field should lead to a Rayleigh-Taylor instability, a simple way to overcome this problem is to enhance the efficiency of convection which pushes the real temperature gradient toward the much smaller adiabatic one (Maeder 1987). This in turn can be achieved either by enhancing the MLT parameter or by using the density scale height instead of the pressure scale height (the former diverges when the density approaches a maximum). However, instead of increasing the efficiency of convection, Bressan et al. (1993) adopted an upper threshold for the real temperature gradient, which is provided by the condition:

$$d\rho/dr \leq 0. \tag{1.51}$$

We will go back to this issue in section 3.2.2.

Rotation

Finally, rotation has not yet been introduced in PARSEC. Rotation has been invoked to explain abundance anomalies seen at the stellar surface, such as the surface Nitrogen enhancement seen in massive stars and, in the case of low mass metal poor stars, the so-called Lithium problem (Fu et al. 2015, for a recent discussion of the problem). Recently it has also been invoked to explain the presence of extended main-sequence turn-off that cannot be fitted with conventional tracks adopting a single age population (e.g., Brandt & Huang 2015; Niederhofer et al. 2015; D'Antona et al. 2015; Li et al. 2014, etc.). However, Girardi et al. (2011); Goudfrooij et al. (2014) argue against the rotation explanation. The main effect of rotation is to induce rotational mixing if there is enough shear between nearby layers. This essentially produces an extended mixing however with characteristics that are different from those produced by a fully mixed overshooting region. Other significant differences are luminosity and effective temperature variations on the photosphere along the meridional coordinate, in such a way that these quantities also depend on the stellar inclination. For massive stars, because of the rotational mixing, which brings the Hydrogen or Helium burning products up to the surface, as well as the effect on the effective gravity potential, the mass loss rate and the appearance of WR stars can be affected. On the other hand, because of the strong mass loss in massive stars, the rotational momentum is also brought away by the stellar wind. All these effects are beyond the goals of this thesis and the reader should refer to Tassoul (2000) and Maeder & Meynet (2011) for a thorough discussion. Finally we mention here that a challenge is the slowly rotating surface Nitrogen enriched massive stars. People found stars with slow rotation but high N-enrichment which is incompatible with the models (Hunter et al. 2008; Frischknecht et al. 2010). However this may be explained with additional parameters like age, binarity and magnetic fields (Maeder & Meynet 2015).

1.6 Other stellar evolutionary models

The Padova evolutionary models have been widely used by the astrophysical community since many years. For seeking of completeness and without pretending to be complete, I list here a number of other stellar evolution codes that are also well known and used by the different research groups.

FRANEC

The FRANEC[6] (Chieffi et al. 2003; Chieffi & Limongi 2013) data base provides Solar metallicity (Grevesse & Sauval 1998) models of mass from 13 to $120M_{\odot}$. It contains both rotating and non-rotating models. The mixing length adopted is $\alpha_{\rm MLT}$ =2.3 and an overshooting of $0.2H_P$ is included. The opacities are from OPAL and LAOL. The equation of state is from Straniero et al. (1997).

BaSTI

The BaSTI library (Pietrinferni et al. 2004, 2014) is computed with the FRANEC code. It contains models in the mass range of $0.5-10M_{\odot}$ and metallicities $Z=0.04$ to 0.0001. The Solar metallicity is from Grevesse & Noels (1993) and the α enhancement follows that from Salaris & Weiss (1998). The opacities are from OPAL for $T>10,000$K, whereas those from Alexander & Ferguson (1994) are used for lower temperatures. Opacities of Alexander & Ferguson (1994) include the contributions from molecular and dust grain. The mixing-length parameter from the Solar-calibration (to reproduce the Solar radius, luminosity, metallicity at an age of 4.57 Gyr) is 1.913 (there are also models computed with 1.25). The overshooting is switched off.

Dartmouth

The Dartmouth[7] (Dotter et al. 2008) data base provides stellar evolutionary tracks in the mass range of $0.1-4M_{\odot}$, and isochrones of age $0.25-15$ Gyr. The metallicities are from [Fe/H] $=+0.5$ to -2.5, and α enhancement from $[\alpha/{\rm Fe}]=0.8$ to -0.2. The Helium abundance are scaled with the relation $Y=0.245+1.54Z$. They also provide $Y=0.33$ and 0.4 models. They use the Solar abundance from Grevesse & Sauval (1998). Their definition of α enhancement is keeping [Fe/H] unchanged but adding the $[\alpha/{\rm Fe}]$ value to each of the α-elements (O, Ne, Mg, Si, S, Ca, and Ti). The mixing length used is $\alpha_{\rm ML}=$ 1.938 (Solar-calibrated). They parameterize the core overshoot as a function of stellar and composition and the overshoot grows with the convective core size. They also use the EOS from FreeEOS. The opacities from OPAL are used for the high temperature, while

[6] http://www.iasf-roma.inaf.it/orfeo/public_html/.
[7] http://stellar.dartmouth.edu/models/index.html.

low temperature opacity tables are calculated by themselves. They employ the Phoenix and Castelli & Kurucz (2003) atmosphere models as the surface boundary conditions.

Geneva

The Geneva stellar evolution model grids[8] are provided for $0.7 - 120 M_{\odot}$ and metallicities from $Z = 0.001$ to 0.1. The models are provided from pre-main sequence to Carbon burning. Models with rotation are also computed.

MESA

MESA[9] (Paxton et al. 2011) is the first scientific open source code for stellar structure and evolution, thus it provides the community the flexibility to modify or improve the code. Since its flexibility, it is useless to mention about the detailed parameters or setups. It has been extended for a wide application: from planets to massive stars, binaries, rotations, oscillations, pulsations, and explosions. Although very large libraries of stellar tracks have not yet been assembled, its future is prosperous.

Yale-Yonsei

The Yale-Yonsei[10] models (Spada et al. 2013) contain models of mass $0.1 - 1.25 M_{\odot}$ and metallicities [Fe/H] $= 0.3$ to -1.5 but with no α enhancement. The Solar abundance is from Grevesse & Sauval (1998). The Helium contents are calculated according to $\Delta Y / \Delta Z = 1.48$. The mixing length is not calibrated but provided at several values with $\alpha_{\rm MLT} = 0.5, 1.0, 1.875, 3.0$. Overshooting is ignored. The OPAL opacities are used at high temperature and Ferguson et al. (2005) opacities are used at low temperature. OPAL EOS is used. Phoenix BT-Settl models are used as the boundary conditions.

Eggleton code

The Eggleton code originated from Eggleton (1971) is now well organized and released to the public at `http://www.ast.cam.ac.uk/~stars/`. They present the homogeneous

[8] `http://obswww.unige.ch/Recherche/evol/Geneva-grids-of-stellar-evolution`.
[9] `http://mesa.sourceforge.net/`.
[10] `http://www.astro.yale.edu/demarque/yyiso.html`.

zero-age main-sequence models of $Z = 0.02$ and mass $0.5 - 9.0\,M_{\odot}$ as input models for the code. Opacity tables of metallicities $Z = 0 - 0.5$ are also provided.

Chapter 2

New evolutionary tracks of very low mass stars with realistic $T-\tau$ relations

2.1 Background

Very low mass stars (VLMS; $M \lesssim 0.6\ M_{\odot}$) are by far the most numerous stars in the Galaxy. For a Kroupa (2001) or Chabrier (2001) initial mass function (IMF), they constitute about 1/3 of the formed stars. Contrarily to the more massive stars, they remain burning Hydrogen during the entire Hubble time, being observable at about the same luminosities from the moment they settle on the main sequence (MS) up to very old ages. At the near–Solar metallicities that characterize the Solar Neighbourhood, they appear mostly as M dwarfs, with their spectral energy distribution (SED) peaking at near–infrared wavelengths, and marked by numerous molecular bands of TiO, VO, water vapor, etc. (e.g., see Allard & Hauschildt 1995; Allard et al. 1997a). At the lower metallicities typical of the thick disk and halo, they also appear as K dwarfs, with their SEDs peaking at red wavelengths (R and I–bands).

VLMS appear copious in *any* deep imaging survey of the Galaxy (such as Sloan Digital Sky Survey (SDSS) and Dark Energy Survey (DES)), and even more in infrared imaging campaigns such as 2MASS (Skrutskie et al. 2006), UKIRT Infrared Deep Sky Survey (UKIDSS) (Lawrence et al. 2007), European Southern Observatory (ESO)/UKIRT In-

frared Deep Sky Survey (UKIDSS) public surveys (Arnaboldi et al. 2012), and *WISE* (Wright et al. 2010). Suffice it to mention that almost half of the 2MASS point sources (Cutri et al. 2003) concentrate at $J-K_s \simeq 0.85$, in a sort of *vertical finger* in near–infrared colour–magnitude diagrams (e.g., Nikolaev & Weinberg 2000); this finger is dominated by M dwarfs at magnitudes $K_s \gtrsim 14$, except at very low galactic latitudes (Zasowski et al. 2013). In the optical, instead, VLMS appear along well–defined colour–magnitude relations, as indicated by stars in open clusters, that made them amenable for the distance derivations via photometric parallaxes, and hence valuable probes of the Milky Way structure (Siegel et al. 2002; Jurić et al. 2008; Ivezić et al. 2012).

VLMS stars are also frequent among the targets of planet searches. Indeed, almost the totality of *Kepler* planet candidates (95% cf. Borucki et al. 2011) are found around dwarfs with masses below 1.2 $M_\odot$, with the best chances of finding Earth-mass planets being around the targets of even smaller masses (e.g., Quintana et al. 2014). In the case of transit detection, the presence of a well-defined mass–radius relation (Torres et al. 2010) allows the easy derivation of planetary properties.

An interesting issue related to the low mass stars is that their evolution can be altered by the presence of asymmetric dark matter as shown by Zentner & Hearin (2011). Because of the asymmetry, some of the asymmetric dark matter is left in the galaxy without annihilation. As the stars move in the dark matter halo, they capture the asymmetric dark matter particles into themselves. Zentner & Hearin (2011) shows that the asymmetric dark matter transports energy away from the stars, thus cools the stellar cores. The consequences are that the mass limit of main sequence stars for Hydrogen burning is elevated and the luminosity is reduced.

Despite the great importance of the very low mass stars, their properties have been poorly predicted and badly matched in present grids of stellar models. E.g., in the mass–radius relation, the stellar models tend to systematically underestimate the stellar luminosity/radii for a given mass (Torres et al. 2010). Significant clarifications have been recently provided by Feiden & Chaboyer (2012) and Spada et al. (2013), who identify the surface boundary conditions in the VLMS models as a critical factor for improving the data–model agreement. Anyway, even for the best models and data, a discrepancy of about 3% remains in the observed radii (Spada et al. 2013). Another recurrent discrepancy is in the colour–magnitude relations of VLMS: indeed, models that fairly well

reproduce the near-infrared colours of VLMS in star clusters (as in Sarajedini et al. 2009), tend to have optical colours which are far too blue at the bottom of the MS, as indicated in An et al. (2008), and as we will show in the following. A similar discrepancy also appears in low-metallicity globular clusters (e.g., Campos et al. 2013). These disagreements imply that present isochrones cannot be safely used to estimate the absolute magnitudes – and hence distances – of field dwarfs, once their optical colours and apparent magnitudes are measured. Instead, empirical luminosity–colour relations have been preferred for this (e.g., Jurić et al. 2008; Green et al. 2014).

In this project, we present our effort on the revision of the PARSEC code (Bressan et al. 2012). We seek for a significant improvement on the VLMS models. The way devised to do so is centred on the revision of the T–τ relation used as the outer boundary condition in stellar models, as will be described in Section 2.2. The revised VLMS models will be transformed into isochrones and compared to some key observations in Section 2.3. The improvement in the models is clear, as summarized in Section 2.4, however, an additional *ad hoc* correction to the T–τ relation is needed to bring models and data into agreement. A subsequent paper will be devoted to a more thorough discussion of the available model atmospheres and synthetic spectra for M dwarfs.

2.2 Implementing Phoenix atmosphere models in PARSEC low mass models

2.2.1 Phoenix atmosphere models

As described above, VandenBerg et al. (2008b); Feiden & Chaboyer (2012); Spada et al. (2013) have pointed out that the discrepancies in the mass–radius relation and color-magnitude diagram between the models and observations may relate to the boundary conditions. By the time of the publication of Bressan et al. (2012), the code was still using the gray atmosphere approximation (Mihalas 1978) as the external boundary condition. That is the relation between the temperature and Rosseland mean optical depth τ across the atmosphere, T–τ, is given by

$$T^4(\tau) = \frac{3}{4} {T_{\rm eff}}^4 \left[\tau + q(\tau)\right] \tag{2.1}$$

where $q(\tau) \approx 2/3$ is the Hopf function. This relation is shown in the figure 2.1. The assumption behind this relation is the diffuse approximation (Mihalas 1978). This holds in the interior of stars, where the optical depth is so large that the photons are trapped in the medium. However, in the atmosphere, for example, at $\tau = 2/3$, the photons have 50% probability to escape from the stars without being absorbed or scattered. So the assumption can not hold. Also, we notice that this relation is independent on the metallicity or gravity of the star. This adds another uncertainty to using the gray atmosphere approximation. Thus, it would improve the situation if more realistic models are used.

One of the choices is the large library of model atmospheres from Phoenix (Allard et al. 2012, and references therein)[1], and in particular the set of BT-Settl models computed with the Asplund et al. (2009) chemical composition, which contains the most complete coverage in stellar parameters (temperature, gravity and metallicity) for both stellar spectra and atmosphere structures. We will discuss these models in chapter 5.1 in detail. These models span a large range of $T_{\rm eff}$, gravity, and metallicity. Both the emergent spectra and the atmosphere structure are provided at each parameter grid. The $T-\tau$ relations in Phoenix (BT-Settl) cover the range of $2600 < T_{\rm eff}/{\rm K} < 700000$ and $0.5 < \log g < 6$ (with g in $\mathrm{cm\,s^{-2}}$), for metallicities Z between $\sim$0.04 and 0.000003. They are well-behaved and generally cover the entire interval from $\tau = 0$ to $\tau \geq 100$. Figure 2.1 shows some selected polynomial fits performed to the atmosphere models, from $\tau = 10^{-4}$ to the boundary at $\tau = 2/3$. They provide an excellent representation of the $T-\tau$ data. The polynomial fits are obtained for each metallicity, $T_{\rm eff}$ and $\log g$ in the database, and later are interpolated among these three parameters.

As we can see that, the $T-\tau$ relation does depend on the temperature, gravity and metallicity. At larger τ and higher effective temperature, the Phoenix $T-\tau$ relations are more close to the gray atmosphere one. $T-\tau$ relations of lower gravities deviate more from the gray atmosphere than that of a higher gravities but of the same metallicity (we have taken into account the different scale of the vertical axis of the plots). The explanation could be that the higher gravity models have higher density, so the photons are more trapped locally. There are also some differences between the $T-\tau$ relations of different metallicities. For example, for $\log g = 5.0$, the low metallicities ones span a wider range in the vertical axis, however, the difference is not prominent. We also notice some other

[1] http://perso.ens-lyon.fr/france.allard/index.html.

features from these plots. E.g., for the $\log g = 5.0$ and [Fe/H]=-0.0 models, the lower is the effective temperature, the higher is the $\log(T(\tau)/T_{\rm eff})$ value, at regions around $\tau = 2/3$. However, there is no general conclusion on the monotonous behaviour. Anyway, from these deviations from the gray atmosphere approximation, we expect some effects on the stellar models computed with these models.

Bolometric corrections from Phoenix models. PHOENIX BT-Settl atmosphere models provide not only the $T-\tau$ relations to be used as the external boundary conditions, but also an extended grid of synthetic spectral energy distributions (SEDs) from which we can compute bolometric correction (BC_λ) tables. We have also implemented the new BC_λ tables to convert the basic output of stellar models into the absolute magnitudes in several passbands M_λ, with

$$M_\lambda = M_{\rm bol} - BC_\lambda, \tag{2.2}$$

where $M_{\rm bol} = -2.5\log(L/L_\odot) - 4.7554$. The formalism to compute BC_λ is thoroughly described in Girardi et al. (2002a), and is also presented in section 5.6. Suffice it to recall that it depends primarily on $T_{\rm eff}$, and to a lesser extent also on surface gravity and metallicity.

These tables of BC_λ will be used later in this thesis, for the $T_{\rm eff}$ interval between 2600 and 6000 K, as an alternative to the previous tables used in PARSEC – which were based on Castelli & Kurucz (2003) and Allard et al. (2000) model atmospheres. In the following, new BC_λ tables will be referred to as NBC, while the previous ones as OBC (see Table B.1). As we will discuss later, the new BC_λ tables have a significant role mainly on the near-infrared colours.

2.2.2 PARSEC models with Phoenix $T-\tau$ relations

Following the indications from various authors (e.g., VandenBerg et al. 2008b; Feiden & Chaboyer 2012; Spada et al. 2013), we replace the approximation in equation (2.1) by the $T-\tau$ relations provided by real model atmospheres.

PARSEC solves the stellar structure at each time step via the Henyey et al. (1964) method as described in Hofmeister et al. (1964) and Kippenhahn et al. (2013). In the atmosphere integration, the family of $T-\tau$ relations – written as a function of $T_{\rm eff}$, $\log g$, and [Fe/H] – replace the simple surface boundary condition formerly represented by equa-

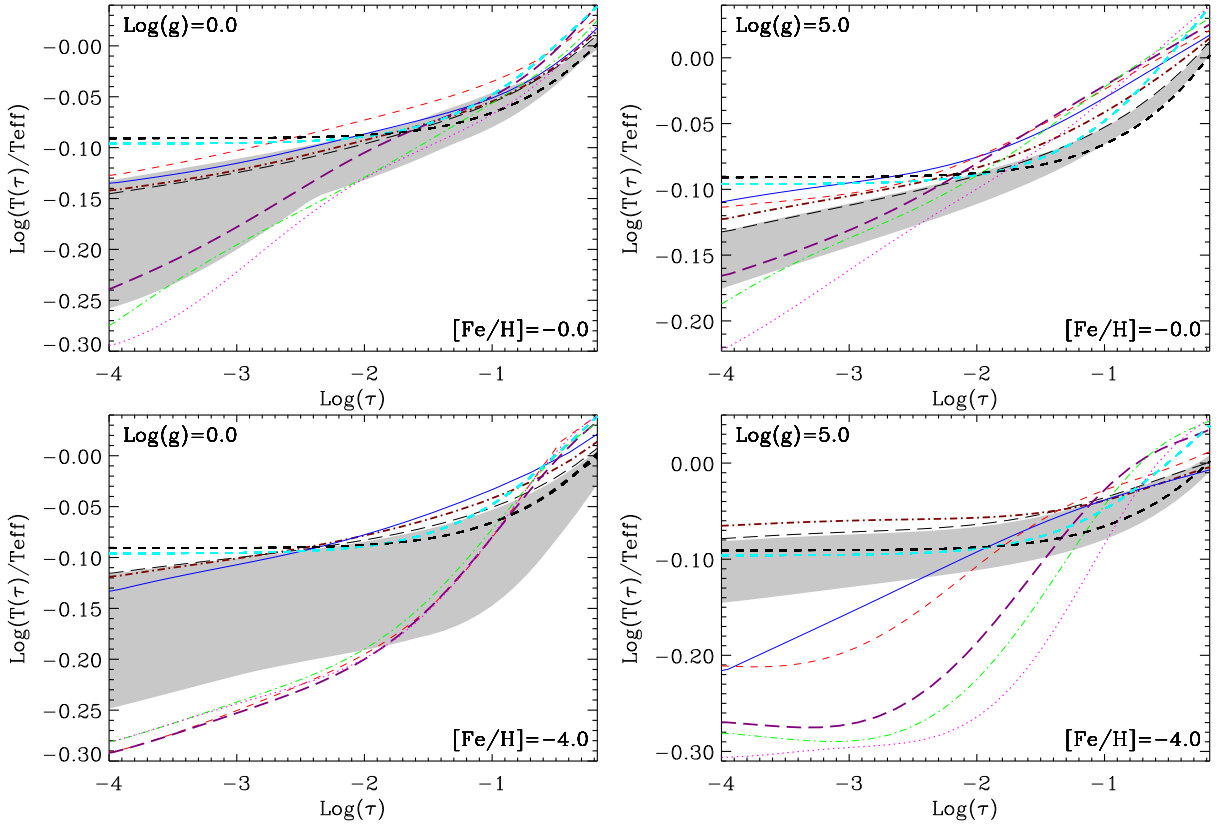

Figure 2.1: A family of polynomial fits to the $T-\tau$ relations from Phoenix (BT-Settl), for [Fe/H] $= 0$ and $\log g = 5.0$, in the region from $\tau = 10^{-4}$ to $\tau = 2/3$. All $T-\tau$ curves have been divided by $T_{\rm eff}$ so as to reduce the vertical scale in the plot. The magenta dot, green dash dot, purple thick long dash, red dash, blue solid, brown thick dash dot and black long dash curves are for $T_{\rm eff}/{\rm K} = 2600, 2800, 3000, 3500, 4000, 4300$ and 4700, respectively. For $4700 < T_{\rm eff}/{\rm K} \leq 10000$, we show only the area occupied by the models (gray shaded). Other relations useful for the discussion in this thesis are also presented: the Krishna Swamy (1966) relation (cyan thick dash line) and the gray atmosphere approximation as in equation (2.1) (black thick dash line).

tion (2.1) in the following way: The boundary is set at $\tau' = 2/3$. The pressure P is integrated starting from the radiative pressure value at $\tau = 0$ up to its value at τ' via $\mathrm{d}\tau/\mathrm{d}P = \kappa R^2/GM$, where κ is the Rosseland mean opacity, R and M are the stellar radius and total mass, and G is the gravitational constant.

We follow the same procedure as described in Bressan et al. (2012) to calibrate the Solar model using the new $T-\tau$ relations. The new Solar model has a $\alpha_{\rm MLT} = 1.77$, which is slightly higher than the previous one used for PARSEC v1.1 (namely $\alpha_{\rm MLT} = 1.74$, see Bressan et al. 2012). This value is assumed for PARSEC models from now on. We have recomputed VLMS models using the new $T-\tau$ relations and $\alpha_{\rm MLT} = 1.77$, for all compositions contained in the previous PARSEC v1.1 release, giving rise to PARSEC v1.2 tracks. They start at the birth line defined by a central temperature of 5×10^4 K, evolve through the pre-main sequence where the main stages of D and ^{3}He burning occur, and finally settle on the zero-age main sequence (ZAMS). Evolution in the main sequence is quite slow and takes longer than 15 Gyr for all masses smaller than about 1 $M_\odot$.

It is evident from the mass–radius relation of figure 2.2 and the $\log L$ versus $\log T_{\rm eff}$ panels of figures 2.3, 2.4, 2.5 and 2.6 (and discussions later in Section 2.3) that the use of the new $T-\tau$ relation has a significant impact on the stellar radii and on the shape of the lower main sequence, with the new ZAMS models becoming significantly larger, cooler (by up to $\Delta T_{\rm eff} \simeq 200$ K) and slightly less luminous, for model stars of the same mass (look at the difference between black and blue lines in figure 2.2, and between blue and green curves in figures 2.3, 2.4, 2.5 and 2.6). In the HR diagrams, however, the lower ZAMS does never become as straight as the upper main sequence. As clarified long ago by Copeland et al. (1970), the curved shape of the lower main sequence is mainly due to the changes in the equation of state (EOS), which enters into a range of significantly higher densities for VLMS. Particularly important are the roles of Coulomb interactions and the formation of the H_2 molecule, which causes a strong reduction of the adiabatic temperature gradient, $\nabla_{\rm ad} = (\partial \log T/\partial \log P)_S$, from 0.4 to about 0.1, in the outer layers of the coolest dwarfs.

2.3 Comparison with the data

In this section we compare the models with a few, selected observational datasets. We start with the mass–radius relation, because it is a fundamental relation that does not involve the stellar SEDs. Then, we discuss the observed CMDs of two open clusters (Praesepe and M67, representing Solar metallicity) and two globular clusters (47 Tuc and NGC 6397, representing metal poor environments).

2.3.1 The mass–radius relation

Figure 2.2 shows the mass-radius relation derived from our tracks, as compared with recent observational data for nearby stars, obtained either via asteroseismic techniques, or via eclipsing binaries[2]. The full data set is presented in Table C.1. Among these observations, the most direct ones are likely those from the eclipsing binaries (see Torres et al. 2010, and Kraus et al. 2011), since they do not depend on any suspicious assumption or uncertain empirical calibration between the photometry and $T_{\rm eff}$. The same happens for the few eclipsing binaries in which the primary is a white dwarf, taken from Parsons et al. (2012a,c), in which the M dwarf masses and radii are particularly well constrained.[3]

It is obvious that the PARSEC v1.1 mass–radius relation is systematically below the empirical data, with a typical deficit of 8 % in the radius for a given mass, over the entire interval between 0.1 and 0.7 $M_{\odot}$. For masses higher than $\sim$ 0.7 $M_{\odot}$, the comparison between model and observed radii is not very significant since the radii increase with the stellar age, so that both models and observations tend to occupy a wider range in this parameter.

This mismatch in the stellar radii is very significant, and has already been noticed by a number of authors (e.g., Casagrande et al. 2008; Kraus et al. 2011, and references therein). It has inspired a few alternative explanations, for instance, an additional growth in radius caused by rotation (Kraus et al. 2011; Irwin et al. 2011), magnetic fields (e.g., Spruit & Weiss 1986; Feiden & Chaboyer 2012, 2013; MacDonald & Mullan 2013; Jackson

[2] Stars measured via interferometric techniques are discarded, since their masses are derived using either empirical or theoretical mass-luminosity relations.

[3] The situation essentially does not change if we adopt the recent compilation of masses and radii from Eker et al. (2014), which, however, is less complete for masses smaller than 0.4 $M_{\odot}$, and does not contain any star below 0.18 $M_{\odot}$. While in this thesis we pay more attention to the lower masses, we decide to just use our own collected data.

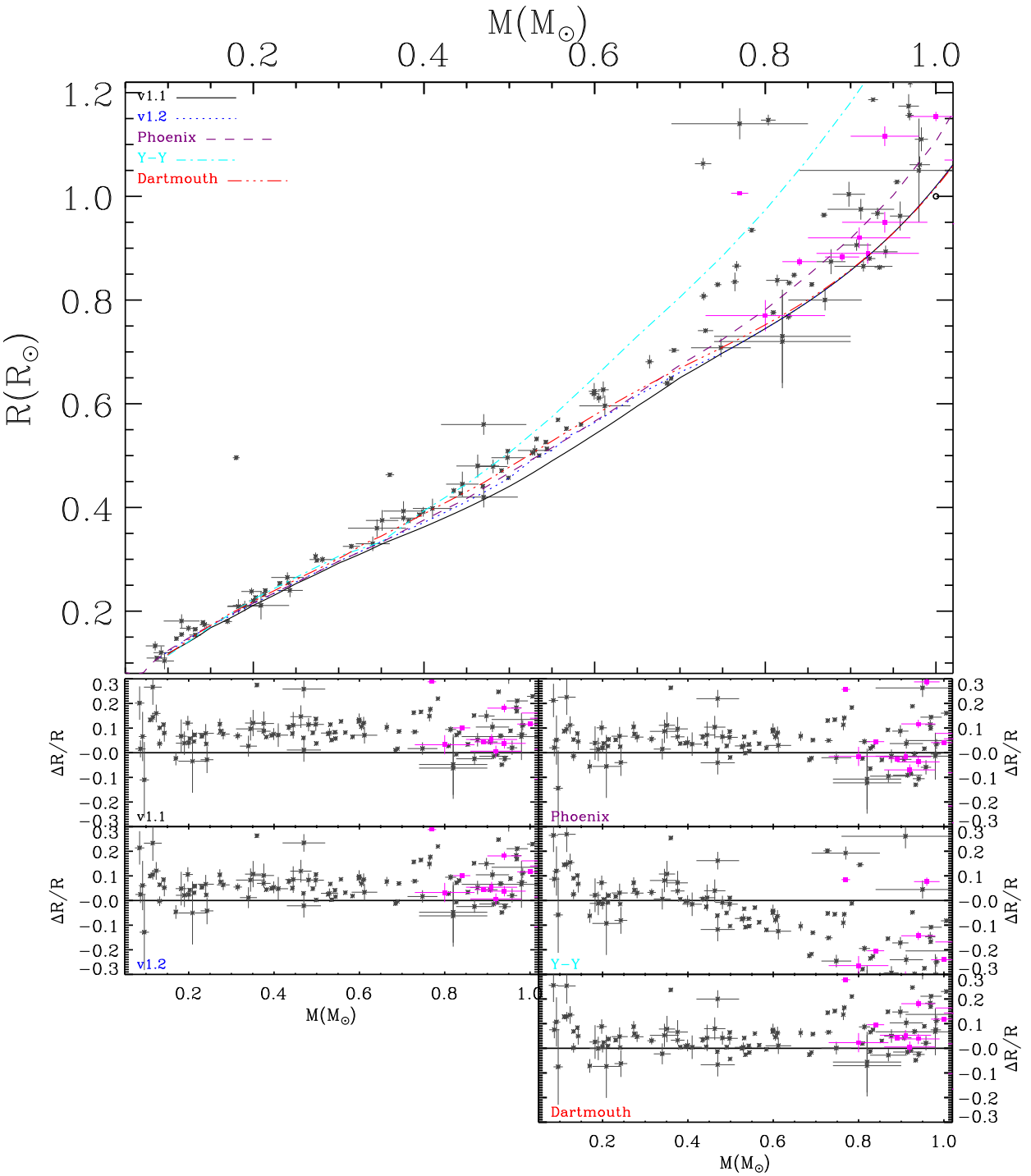

Figure 2.2: The empirical mass–radius relation for low mass stars in the Solar neighbourhood using compiled data listed in Table C.1. Black asterisks are binary stars; Magenta squares are single stars. On the upper-left panel, isochrones of 5 Gyr are overplotted for comparison for different models. PARSEC v1.1 isochrones are shown in black while our updated isochrones (v1.2, Z=0.02) are in blue. Phoenix (Z=0.02), Y-Y (Z=0.01631) and Dartmouth (Z=0.01885) models are in purple, cyan and red respectively. The other panels are the differences compared to the observation for different models as the labels shown. Y axis of $\Delta R/R$ is defined as $(R_{\rm obs} - R_{\rm mod,5Gyr})/R_{\rm obs}$.

& Jeffries 2014, and references therein). These mechanisms may indicate that eclipsing binaries follow a different mass–radius relation than single field stars, although Boyajian et al. (2012) and Spada et al. (2013) find that their radii are indistinguishable.

The lower-left panel of figure 2.2 shows that in PARSEC v1.2 models, this mismatch is reduced down to ~ 5 %.

We verified that it is really hard to eliminate this discrepancy in radii. Concerning the effect of using different EOSs, it has been investigated by many authors. The most recent study concerns very low mass stars. For example, di Criscienzo et al. (2010) has shown that different EOS equations do affect the tracks of low mass stars ($M < 0.5 M_{\odot}$) with respect to more massive stars. Thus, for a few tracks, we have explored a change in the EOS, for instance testing the use of our previous Mihalas et al. (1990) EOS for temperatures lower than 10^7 K, and the OPAL EOS (Rogers et al. 1996) for higher temperatures. The effect on the radii was close to null. Moreover, we note that our adopted FreeEOS is a modern EOS that includes all major effects of relevance here. We note in particular that our models reproduce the velocity of sound across the Sun to within 0.6 %, which is well within the error bars. Therefore, the situation is not easily remediable: Significant changes in the equation of state, apart from not being motivated, would probably ruin the agreement with the Standard Solar Model.

Changes in the mixing-length parameter $\alpha_{\rm MLT}$ are also revealed to be non-influential: models with $\alpha_{\rm MLT}$ as low as 0.1 have their radii increased by only ~ 2 %. The use of very different metallicities and Helium contents does not change the situation neither.

Figure 2.2 also compares the mass–radius data with three other recent sets of models.

1. "Phoenix", which are essentially the Baraffe et al. (1997, 1998) theoretical isochrones transformed with their synthetic colour tables. They have not implemented their T–τ relation into their isochrones, but only the colours.

2. Yale-Yonsei (Y–Y; Spada et al. 2013) which used Phoenix (BT-Settl) T–τ relation to improve their previous Y–Y models. $\alpha_{\rm MLT} = 1.743$ was used. They demonstrate the large improvement compared to their previous models for masses below $0.6 M_{\odot}$.

3. Dartmouth (Dotter et al. 2008) which used Phoenix model atmospheres (both T–τ and the synthetic colour-$T_{\rm eff}$ transformations) and $\alpha_{\rm MLT} = 1.938$.

All models are computed for metallicities close to Solar. It is easy to notice that Phoenix models present almost the same discrepancy as ours, for the entire mass range of VLMS. Dartmouth models present more or less the same pattern, but with reduced discrepancies in the interval between 0.2 and 0.6 $M_{\odot}$. Y-Y models, instead, present overestimated radii only for masses below 0.45 $M_{\odot}$; they turn out to be underestimated instead for all higher masses. It is hard to trace back the origin of these differences.

Before exploring other possible changes to our models, we decided to look at the main sequences of VLMS stars in open and globular clusters.

2.3.2 The lower main sequence in Praesepe

Praesepe is the perfect cluster to study the shape of the lower main sequence: it is reasonably well populated, it has an age high enough to have all VLMS already settled on the main sequence, and in addition it has excellent (and uncontroversial) trigonometric parallaxes from Hipparcos. van Leeuwen (2009) finds $(m-M)_0 = 6.30$ mag, log(age/yr)=8.90 ($\sim$0.8 Gyr), and $E(B-V) = 0.01$ mag. In addition, the cluster has been recently and deeply observed by the Panoramic Survey Telescope & Rapid Response System (Pan-STARRS); Wang et al. (2014) provides a comprehensive catalogue containing hundreds of VLMS, with memberships provided by the combination of Pan-STARRS and 2MASS photometry, and PPMXL proper motions.

Figure 2.3 presents the Wang et al. (2014) data in several diagrams involving Pan-STARRS and 2MASS photometry, and as compared to a few sets of models. The models are initially shown in the theoretical H-R and mass-luminosity plots (top panels), for an age of log(age/yr) = 8.90 (van Leeuwen 2009) and a metallicity of $Z = 0.02$ [Carrera & Pancino (2011) presents [Fe/H] = 0.16, which corresponds to $Z = 0.0244$ with their adopted Solar abundance]. Then, the other panels show the $g - z$ versus z, and the $g - K_{\rm s}$ and $J - K_{\rm s}$ versus $K_{\rm s}$ CMDs. It is evident that the previous PARSEC v1.1 models (black and blue lines, with OBC and NBC, respectively) fail to describe the lower main sequence in CMDs involving the optical filters g and z. In the case of the near-infrared $J - K_{\rm s}$ versus $K_{\rm s}$ CMD, the colour offset of the PARSEC v1.1 models almost completely disappear when we adopt the new bolometric corrections NBC (blue lines). In all the other CMDs, using the NBC just slightly moves the VLMS models towards the observed sequence.

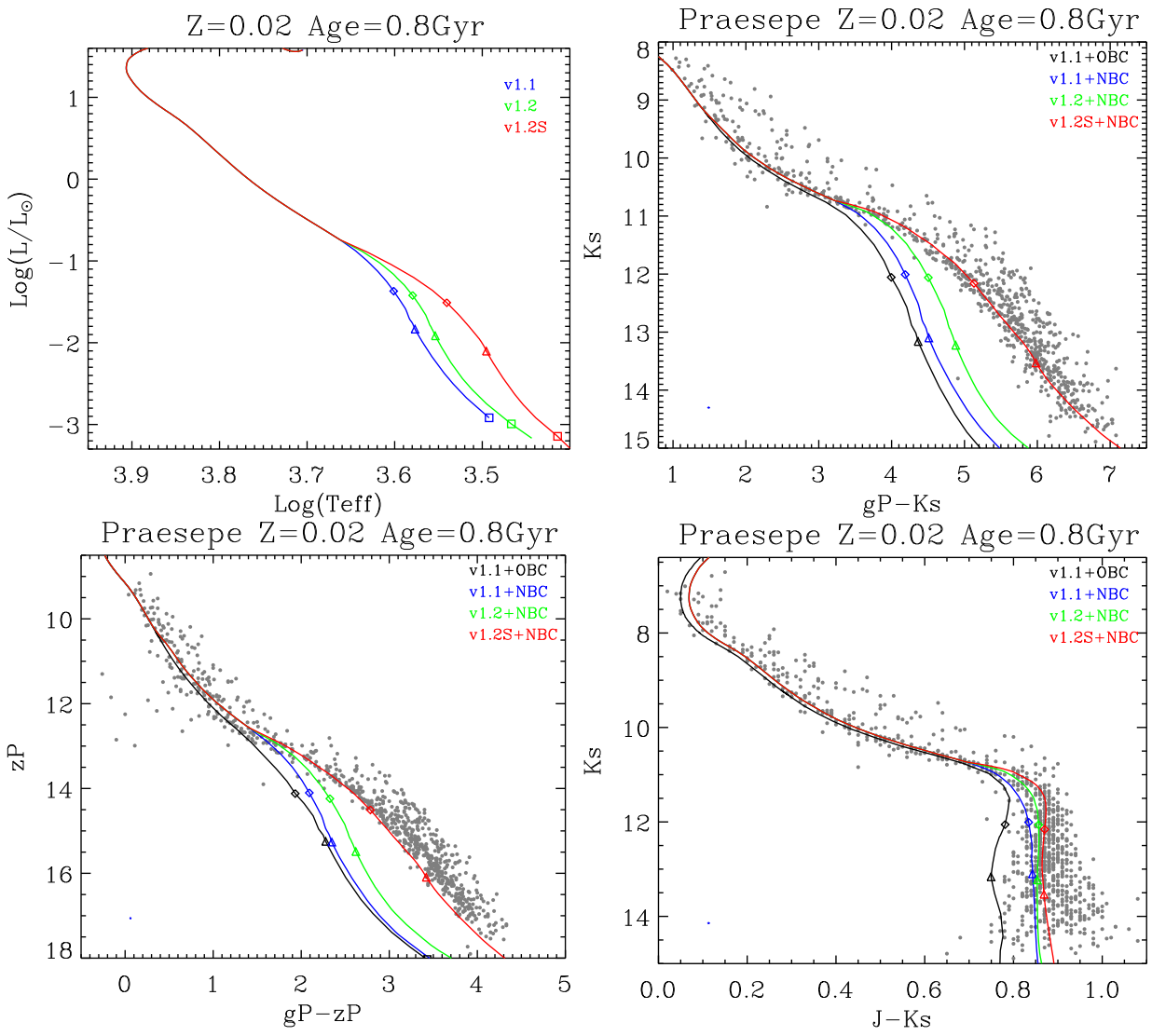

Figure 2.3: CMDs for Praesepe. The data points come from Wang et al. (2014) with Pan-STARRS and 2MASS data. Black curves: PARSEC v1.1 isochrones with our previous BC_λ tables; Blue curves: PARSEC v1.1 isochrones with new BC_λ tables; Green curves: new isochrones (v1.2) with $T-\tau$ relation derived from Phoenix (BT-Settl) models and interpolated with new BC_λ tables; Red curves: new isochrones (v1.2S) with calibrated $T-\tau$ relation upon those derived from Phoenix (BT-Settl) models and interpolated with new BC_λ tables. The galactic reddening we use for Praesepe is $E(B-V)=0.01$ and the distance modulus is $(m-M)_0=6.30$ mag (from Hipparcos parallaxes, van Leeuwen 2009). The isochrones are for $Z=0.02$ and age $=0.8$ Gyr. We also indicate initial the masses of 0.5, 0.3, 0.1 $M_\odot$ along the isochrones with open diamonds, triangles and squares respectively.

The use of the T–τ relation, as illustrated by the green lines, causes the optical colours to move towards the observed sequences in a slightly more decisive way, but anyway, it is evident that no good agreement with the data is reached. The only exception seems to be the near-infrared $J-K_s$ versus K_s diagram, in which all the model sequences in which the NBC tables are used appear with a satisfactory agreement with the data, being able to produce the vertical sequence observed at $J-K_s \simeq 0.9$. Possible discrepancies with the data are at a level of just a few hundredths of magnitude in $J-K_s$.

Anyway, the important point that comes out of this comparison is the incapacity of models using the T–τ relation, and the latest tables of bolometric corrections, to reproduce the optical colours of VLMS in Praesepe, with discrepancies being as large as $\sim$1 mag in colours as $g-z$ and $g-K_s$. The models turn out to be far too blue, which suggests that some improvement could be reached by further decreasing the $T_{\rm eff}$ – hence increasing the stellar radius – of the models, as we will see later.

2.3.3 The lower main sequence in M 67

The open cluster M 67 constitutes another excellent testing ground for our models, since it has extensive photometric and membership data, added to well-determined global ages and metallicities (e.g., VandenBerg & Stetson 2004; Randich et al. 2006), and a small foreground reddening.

We have combined the following data sources for M 67:

- the astrometry, BVI photometry, and membership probability $P_{\rm mb}$ from Yadav et al. (2008);
- the 2MASS very deep photometry from the "Combined 2MASS Calibration Scan" (Cutri et al. 2003; see also section 2 of Sarajedini et al. 2009);
- the SDSS point spread function photometry as performed by An et al. (2008).

The different catalogs were cross-matched with the Panoramic Survey Telescope & Rapid Response System (Pan-STARRS) (Taylor 2006) revealing positional offsets typically smaller than 0.5″. Figure 2.4 shows a few of the resulting CMDs for stars with $P_{\rm mb} > 20$ %. These diagrams are typically very clean for all magnitudes brighter than $g = 20$ mag, whereas a

significant number of outliers appears at fainter magnitudes – either due to the more uncertain memberships or to the worse photometric quality in this range of brightness. The important point for us is that the lower MS is very well delineated. A parallel sequence of nearly-equal-mass binaries is also evident, and located 0.7 mag above the MS.

In figure 2.4 we present the fit of M 67 for which we assume a distance modulus $(m-M)_0 = 9.75$ mag and a reddening $E(B-V) = 0.03$ mag. For the sake of simplicity we use models with $Z = 0.02$ and, since this value is slightly higher than the observed metallicity (Sarajedini et al. 2009), we obtain an age of 3.5 Gyr which is a lower limit to the ages quoted in literature (Sarajedini et al. 2009). As we will see in the following, this will not affect the results of our investigation. In the H-R diagram (top left panel of figure 2.4), these isochrones appear nearly identical to those shown for Praesepe, for all luminosities below $\sim$1 $L_\odot$. The comparison with the models reveals essentially the same situation as for Praesepe: whereas the use of the NBC and $T-\tau$ relations both contribute to redden the model VLMS sequences, and reduce the disagreement with the data, the revised PARSEC v1.2+NBC models remain too blue at optical colours. The near-infrared colour $J-K_s$ instead is little affected by the changes in the $T-\tau$ relation and reasonably well reproduced by all the NBC models.

The comparison with the blue band colours, such as the $B-V$, is more problematic and it is discussed in detail in section 2.6.

2.3.4 Ultra-deep HST/ACS data for 47 Tuc and NGC 6397

47 Tuc (NGC 104) is a relatively metal-rich globular cluster. The most recent abundance determination gives [Fe/H] = −0.79 and a median value of [O/Fe] $\sim$ 0.2 (Cordero et al. 2014). Carretta et al. (2010) give a distance modulus of $(m-M)_V = 13.32$, an age of 12.83 Gyr, and a reddening of $E(B–V) = 0.04$ mag, while Hansen et al. (2013) determines an age of 9.7 Gyr from the white dwarf cooling sequence. Kalirai et al. (2012) obtained extremely deep *Hubble Space Telescope (HST)*/Advanced Camera for Surveys (ACS) F606W and F814W data for this cluster (with 50% completeness limits at $\sim$29.75 and 28.75 mag for F606W and F814W, respectively), which makes it an excellent test bed for the lower main sequence. We compare our models with these observational data in figure 2.5. To fit the data with our models, we assume a metallicity of $Z = 0.004$, a distance modulus of $(m-M)_0 = 13.20$, an age of 10 Gyr and $E(B-V) = 0.05$ mag.

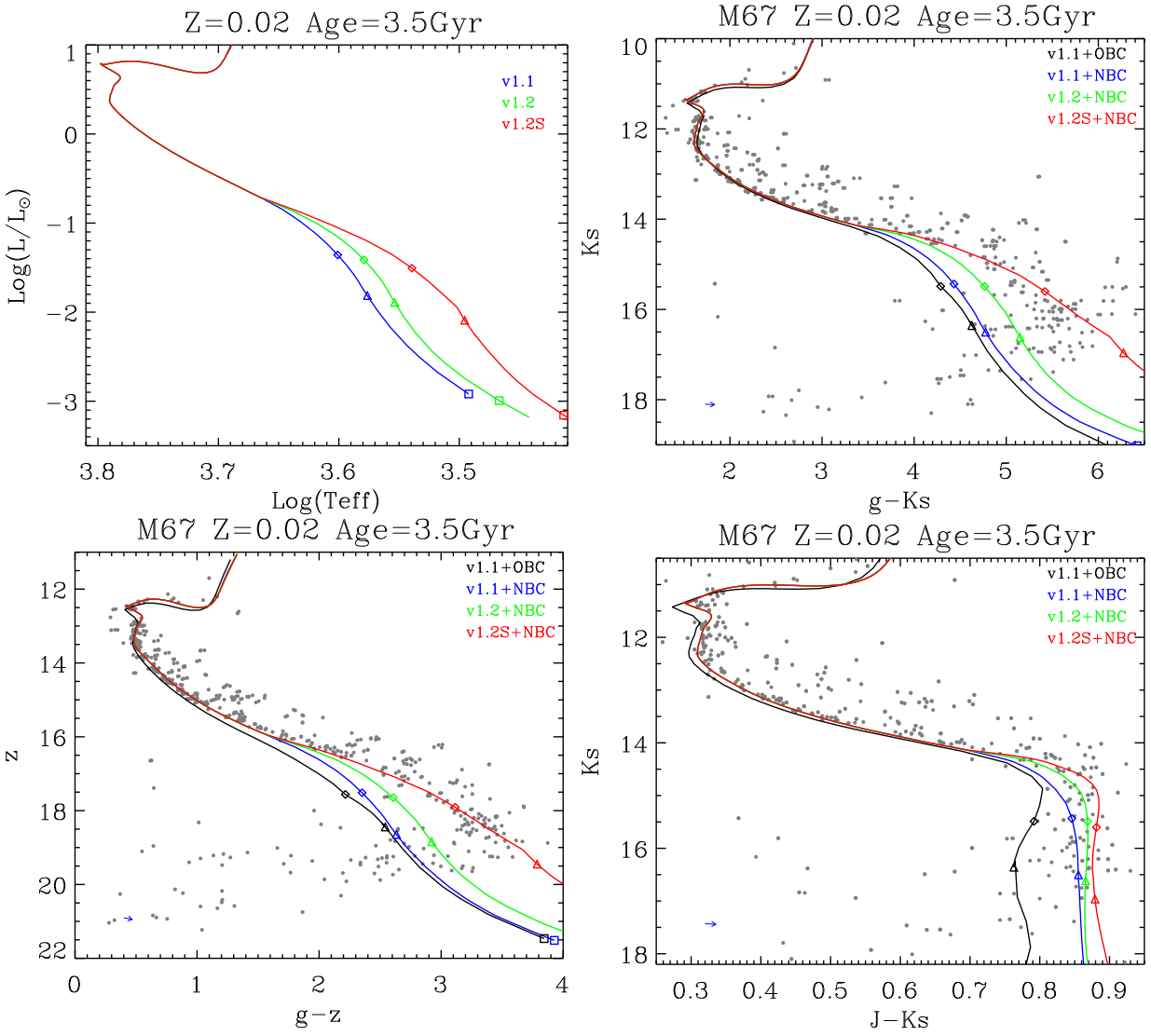

Figure 2.4: M 67 in several CMDs. The data points come from matching Yadav et al. (2008) catalog with SDSS and 2MASS catalogs (see text). The labels are the same as in figure 2.3. The blue arrow in the left-lower corner of each panel is the reddening vector. The galactic reddening we use for M 67 is $E(B-V) = 0.03$ and the distance modulus is $(m-M)_0 = 9.75$ mag. The isochrones are for $Z = 0.02$ and age = 3.5 Gyr.

Recently, Milone et al. (2012) presented detailed chemical composition study of 47 Tuc. They found that then were able to match the complex of observed colors with a pair of populations, one with primeval abundance and another with enhanced Nitrogen and a small Helium enhancement, but with depleted C and O. With these abundances, we computed two isochrones. Then we use them to fit the observational data of this cluster. In our new study, we want to address the influence of the α-enhancement on the evolutionary tracks, though they do not influence the lower main sequence. In Kalirai et al. (2012), there are not many stars in the horizontal branch because of their criteria for clean up the star members. So, we use the data from (Sarajedini et al. 2007). Our new fitting gives a distance modulus of $(m-M)_0 = 13.12$, an age of 12 Gyr and $E(B-V) = 0.07$ mag. We notice that Watkins et al. (2015) gives an (intrinsic) distance modulus of 13.09 from the proper motion measurement of this cluster. Our fitting is quite close to this value. However, we are still using the same bolometric table as in this chapter (with the global metallicities corresponding to that of the two populations).

It is evident that PARSEC v1.1 and v1.2 models fail to reproduce the lower main sequence in 47 Tuc, in a way similar to what was already noticed for Praesepe and M 67. It is also evident that the NBC and the use of $T-\tau$ relations cause models to move on the right direction, but do not suffice for them to reach the observed sequences. In 47 Tuc, the discrepancy between models and data start at about $F814W = 20$, which corresponds approximately to stellar models of mass $M = 0.6\ M_{\odot}$. Finally we note that with an isochrone of 12.6 Gyr we can also fit the turn-off very well, while with the isochrone of 10 Gyr, we need to enhance the Helium content. But since the goal of this thesis is to improve the models for the lower main-sequence, we leave the detailed modelling of the turn-off and red giant sequences to a future work.

Going to even smaller metallicities, we have the case of NGC 6397 with a measured metallicity of [Fe/H] $= -1.988$ (and $[\alpha/\mathrm{Fe}] = 0.36$, cf. Carretta et al. (2010), corresponding to $Z = 0.000376$ with their adopted Solar abundance). Carretta et al. (2010) also give a distance modulus of $(m-M)_V = 12.31$, an age of 13.36 Gyr, and a reddening of $E(B-V) = 0.18$ mag. Richer et al. (2008) observed this cluster with HST/ACS and, after proper motion cleaning, obtained a very narrow main-sequence down to F814W$\sim$26 mag, as shown in figure 2.6. To fit the data with our models we assume a metallicity of $Z = 0.0005$ (the nearest metallicity in PARSEC v1.1), a distance

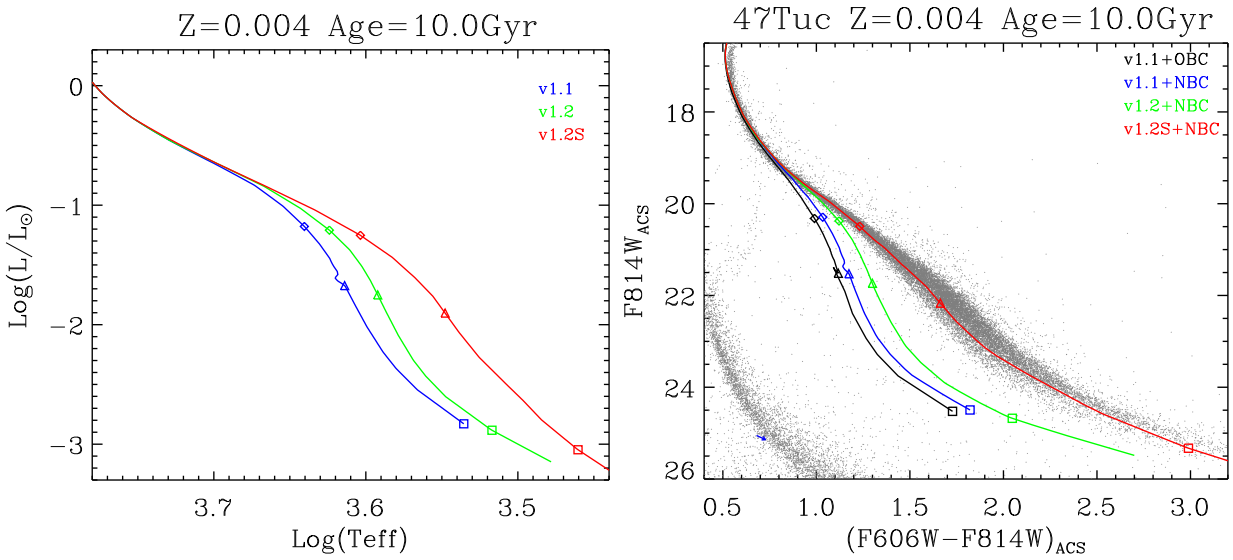

Figure 2.5: CMDs for 47 Tuc. The data points are from Kalirai et al. (2012). The sequences at the bottom-left corner of the CMD correspond to the background SMC population, and should be ignored. Model isochrones are presented with the same labels as in figure 2.3, but for a reddening of $E(B-V) = 0.05$ mag, and a distance modulus of $(m-M)_0 = 13.20$ mag. The isochrones are for $Z = 0.004$ and an age of 10 Gyr.

modulus of $(m-M)_0 = 11.95$, an age of 12 Gyr and $E(B-V) = 0.2$ mag. Comparison with PARSEC v1.1 and v1.2 models reveals about the same discrepancies as for 47 Tuc, but now starting at $F814W \simeq 19$ mag.

We remind the reader that the models used here adopt a Solar abundance partition, without enhancement of α elements. While the effect of α-enhancement is the goal of a forthcoming detailed analysis on globular clusters properties, we notice that its effects on the $T-\tau$ relation are of secondary importance, after it is accounted for in deriving the global metallicity.[4]

2.3.5 Comparing the CMDs with other models

The sequence of figures 2.7 to 2.10 compares our best-performing isochrone set so far – namely the PARSEC v1.2+NBC – with those from other groups already introduced in Section 2.3.1, and with the data of the four clusters we have just discussed. In doing so, we are by no means trying to find the best-fitting isochrone for each model set and cluster, we are just overplotting them for the same assumed distance and reddening, for a quick

[4] As first noted by Kalirai et al. (2012), a dispersion in the abundance ratios might be at the origin of the colour dispersion observed at the bottom of the main sequence in 47 Tuc.

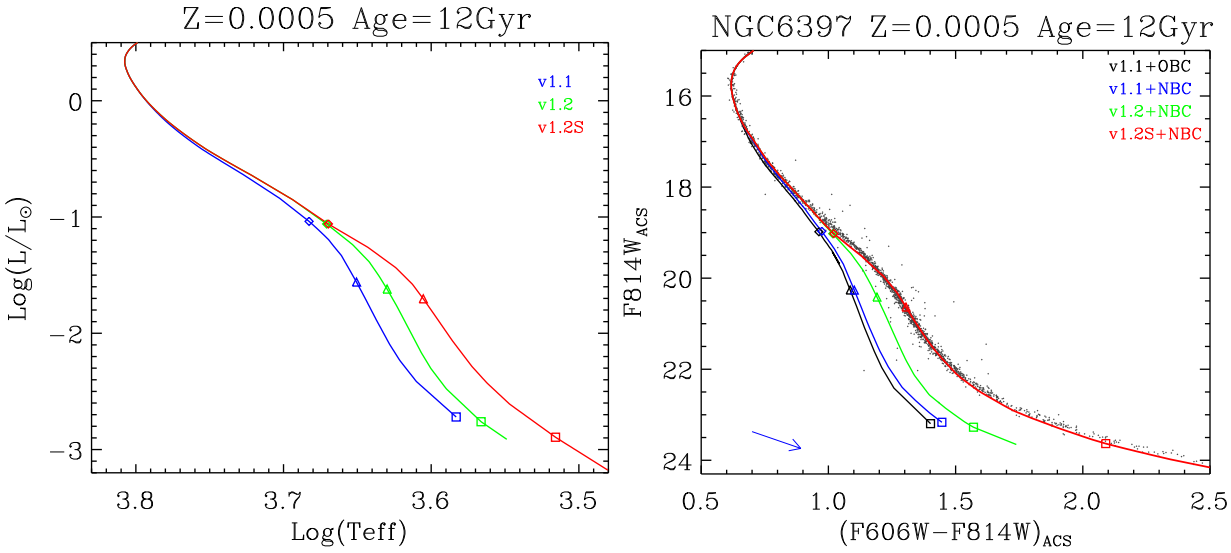

Figure 2.6: CMDs for NGC 6397. The data points come from Richer et al. (2008). Model isochrones are presented with the same labels as in figure 2.3, but for a reddening of $E(B-V) = 0.2$ mag, and a distance modulus of $(m-M)_0 = 11.95$ mag. The isochrones are for $Z = 0.0005$ and an age of 12 Gyr.

comparison of the several sets. The comparisons are first made in the H–R diagram, and later in the CMDs for which we have isochrones available in the same filter sets.

As can be seen in the figures, none of the sets being compared agrees perfectly in the H–R diagram, even if the Y-Y and Dartmouth models implement similar $T-\tau$ relations as in our PARSEC v1.2 models. Our v1.2 models are slightly hotter than both Dartmouth and Phoenix models in the lower main-sequence at near-Solar metallicity (figures 2.7 and 2.8), but still significantly hotter than those at low metallicities (figures 2.9 and 2.10). Tracing back the origin of these differences is difficult at this stage, and is beyond the scope of this thesis.

When we look at the CMDs in figures 2.7 to 2.10, in addition to the intrinsic difference in the evolutionary tracks, we also see the effect of the different tables of bolometric corrections adopted by the different groups. What is more remarkable in the Preasepe and M 67 plots is that all models seem to reproduce satisfactorily the kink that occurs at the bottom of the main sequence in the near-infrared colour $J-K_s$. However, in all cases the fit is far from satisfactory when we look at the colours which involve optical filters. The same applies to the two old globular clusters as shown in figures 2.9 and 2.10.

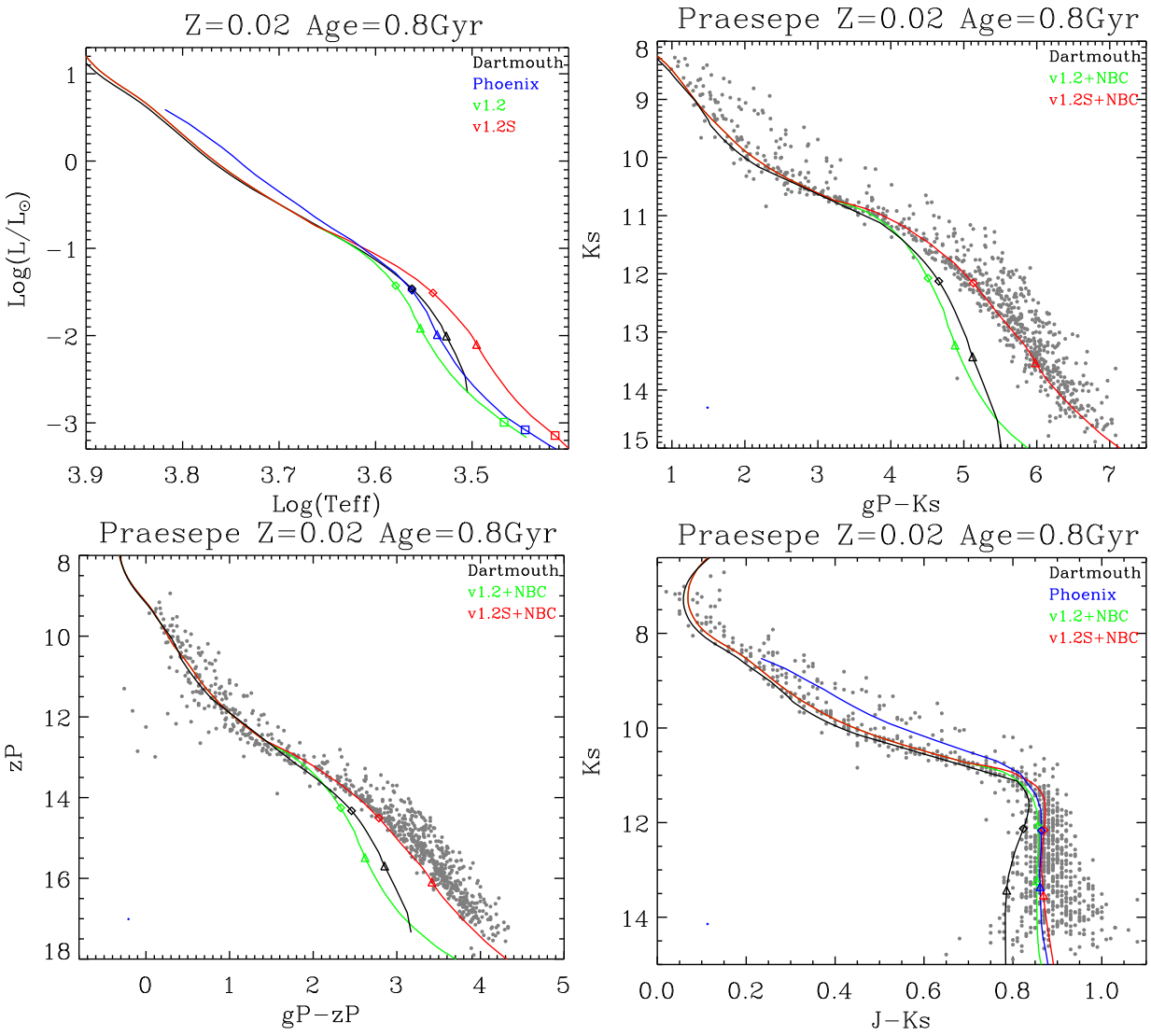

Figure 2.7: CMDs for Praesepe, same as in figure 2.3, except that the black lines are for Dartmouth with $Z = 0.01885$ and age $= 0.8$ Gyr, and the blue ones are for Phoenix with $Z = 0.02$ and age $= 0.8$ Gyr.

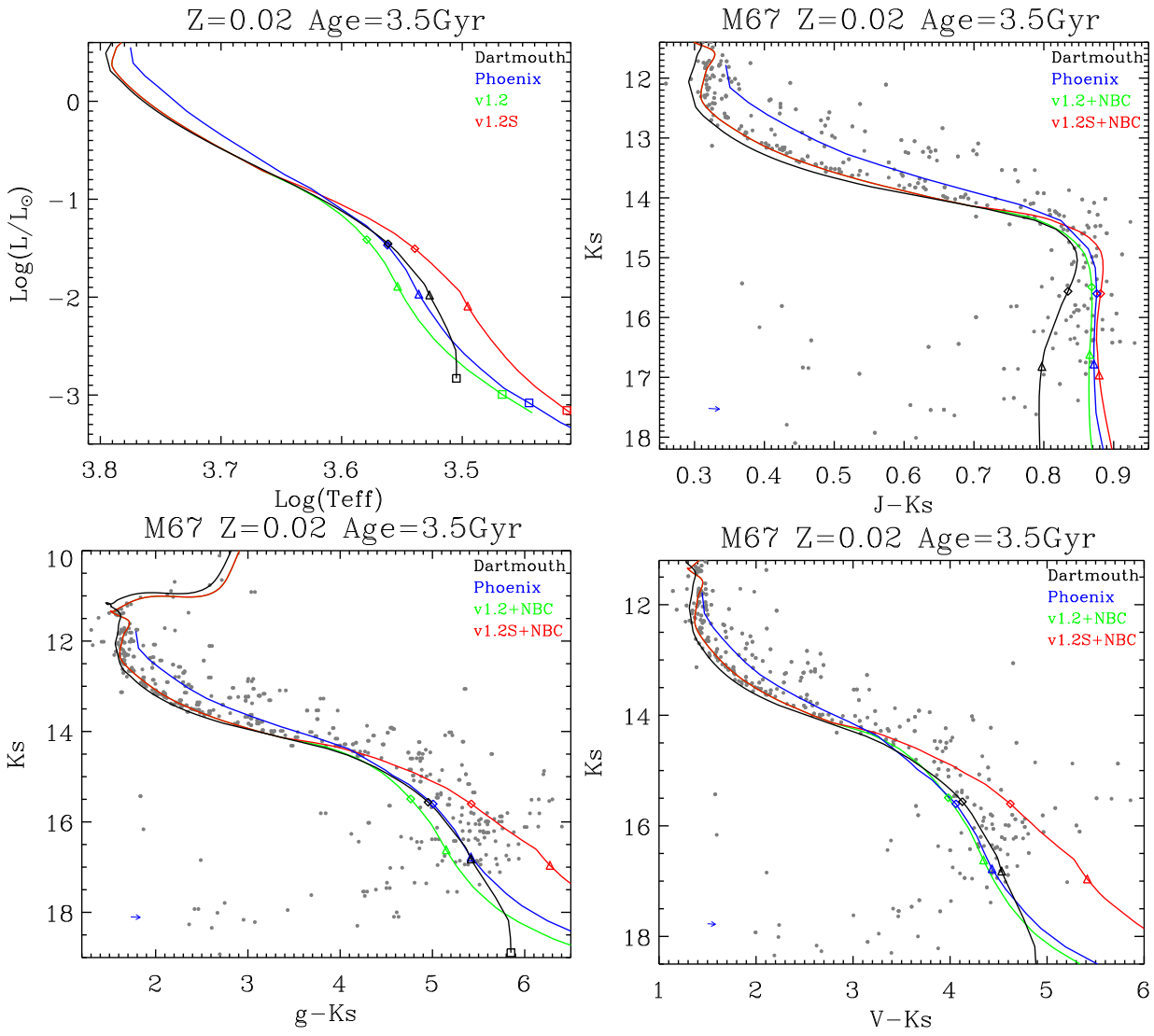

Figure 2.8: M 67 in several CMDs, same as in figure 2.4, except that the black lines are for Dartmouth with $Z = 0.01885$ and age $= 3.5$ Gyr, and the blue ones is for Phoenix with $Z = 0.02$ and age $= 3.5$ Gyr.

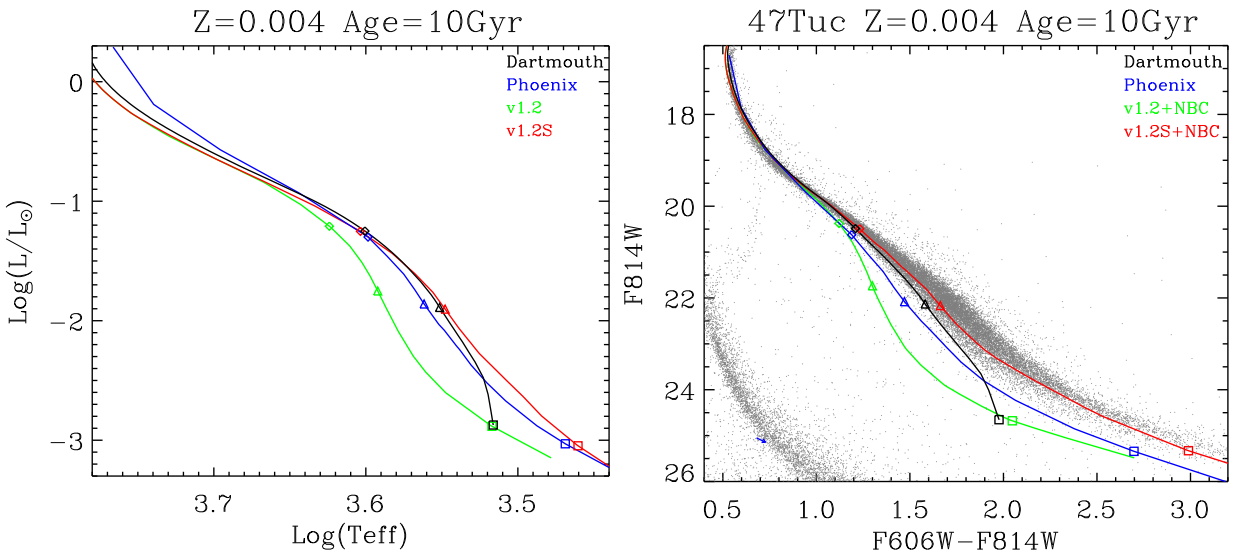

Figure 2.9: CMDs for 47 Tuc, same as in figure 2.5, except that black lines are for Dartmouth ($Z = 0.0053740$ and age $= 10$ Gyr) and blue ones are for Phoenix ($Z = 0.006340$ and age $= 10$ Gyr).

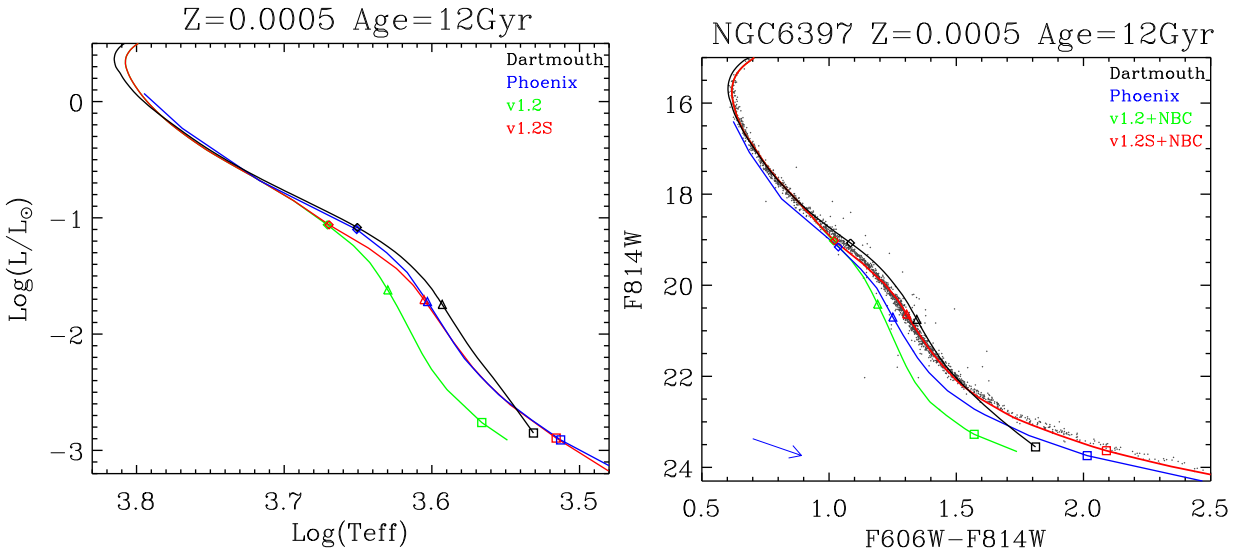

Figure 2.10: CMDs for NGC6397, same as in figure 2.6, except that black lines are for Dartmouth ($Z = 0.00054651$ and age $= 12$ Gyr), and blue ones are for Phoenix ($Z = 0.000307$ and age $= 12$ Gyr).

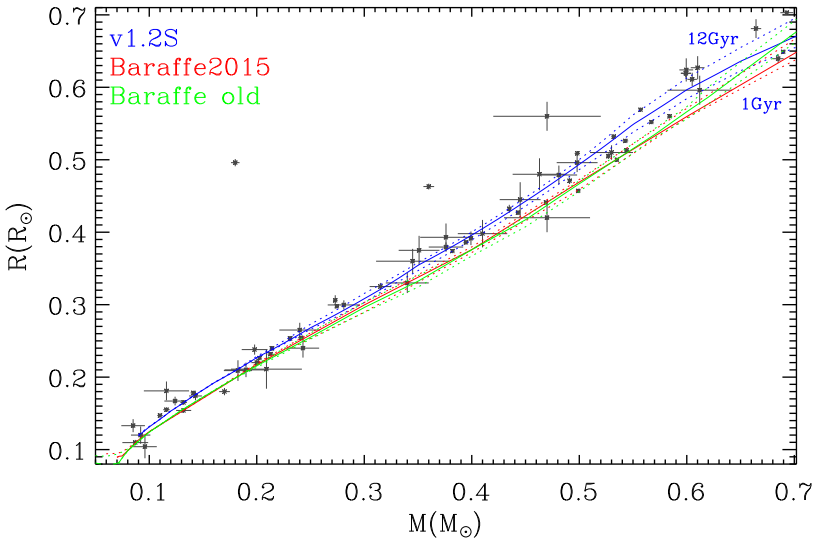

Figure 2.11: Comparison with new Phoenix models (Baraffe et al. 2015). Blue: PARSEC v1.2S models; Red: Baraffe 2015 models, Green: Baraffe98 models. Solid lines are for 5 Gyr, while dashed lines are for 1 Gyr (lower one) and 12 Gyr (upper one).

Comparison with new Phoenix models. Recently, Phoenix group published a new set of isochrones (Baraffe et al. 2015), which supersede the old Phoenix models (or BCAH98). We single them out here for two reasons. First, these are the newest published models (among other models). Second, our models rely on their atmosphere models, thus this kind of comparison can provide us more direct interpretation. As stated in their paper, there are some difference for models with mass larger than 0.65 $M_\odot$. In the figure 2.11 we compare the mass radius relations with new Baraffe models. We find a very small difference between their new and old models. This result is also shown in figure 2.12 (by ignoring the part below 0.1 $M_\odot$).

2.4 A further step at improving the low mass models in PARSEC

As is evident from the previous discussion, adopting better BC$_\lambda$ tables and $T-\tau$ relations is not enough to bring models and data into agreement, and the problem seems to extend to other sets of models in the literature as well. Interestingly, we note that the changes requested in the mass-radius relation – namely larger radii at a given mass – go in the same sense of the changes required to improve the agreement with the CMDs – namely lower $T_{\rm eff}$ (larger radii) for a given luminosity. Moreover, the discrepancies start to appear

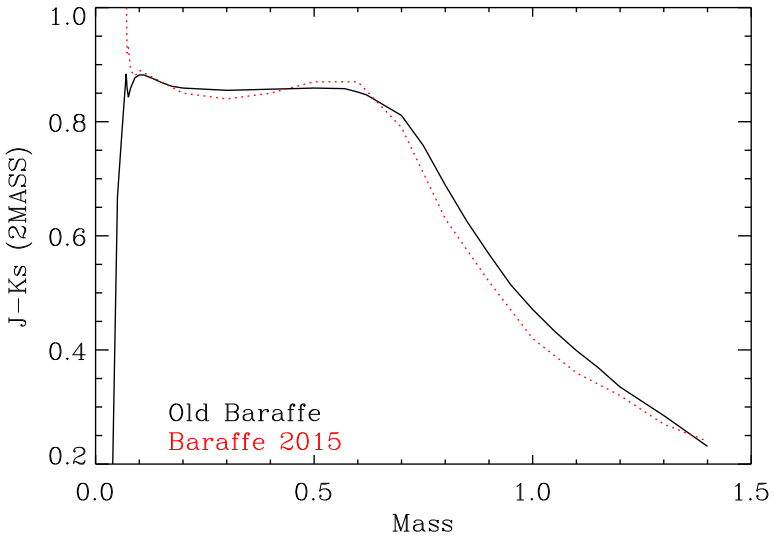

Figure 2.12: Comparison of colors between Phoenix models. Red: Baraffe 2015 models, Black: Baraffe98 models.

more or less at the same masses down the main sequence, namely at $\sim$0.5 $M_{\odot}$. Therefore, it is natural to seek for changes that increase the stellar radii of the models, and check whether this causes better agreement with the CMD data. This is essentially the approach we will pursue in the following.

2.4.1 A recalibration of the $T-\tau$ relation

As can be seen in figure 2.1, the BT-Settl $T-\tau$ relations are distributed in a relatively narrow region of the $T/T_{\rm eff}$ versus τ plane and, at large values of τ, they converge towards and even exceed the gray $T-\tau$ relation. This effect becomes more prominent at lower effective temperatures, where the $T-\tau$ relations near the photosphere become significantly hotter than the gray atmosphere one. The excess reaches $\Delta \log(T/T_{\rm eff}) \sim 0.04$ dex and is likely caused by the formation of molecules at low temperatures, which trap the radiation in the atmosphere. It is this shift of the $T-\tau$ relation that causes some improvement in the mass–radius of the main sequence models and, consequently, on the corresponding colour-magnitude relations. However the agreement with observations of lower main sequence stars is far from being satisfactory. Thus, we wonder if (1) the mismatch can be due to an underestimate of the photospheric temperature by the $T-\tau$ relations at smaller $T_{\rm eff}$, and if (2) we could use the observed mass-radius relation shown in figure 2.2 to calibrate the $T-\tau$ relations at low effective temperatures.

Concerning the first point we can only say that there are many such relations in the

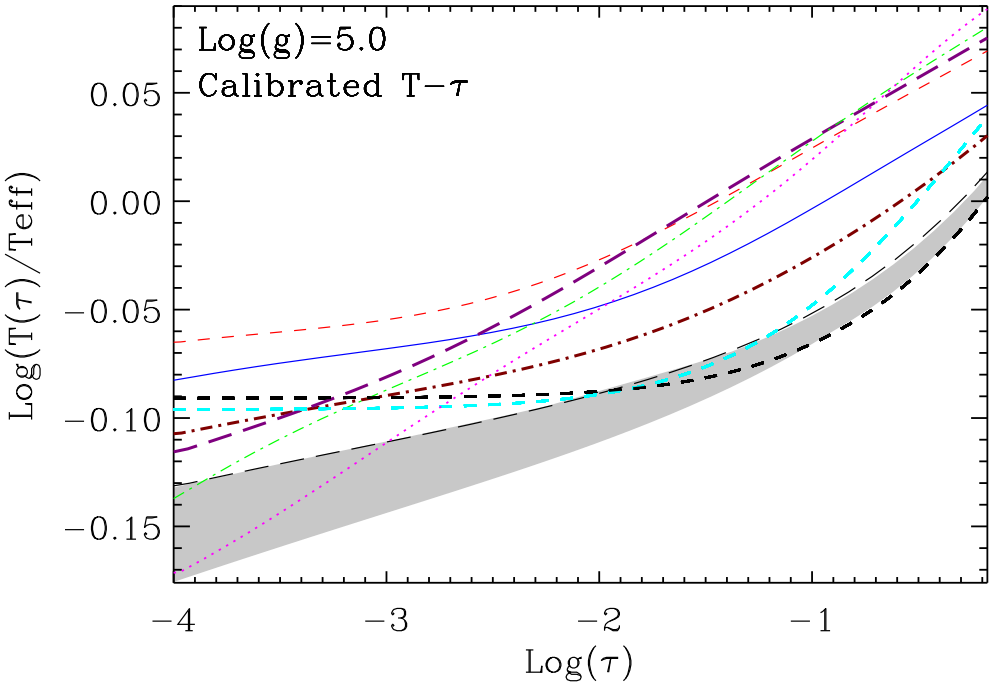

Figure 2.13: As figure 2.1, but for calibrated $T-\tau$ relations, as described in section 2.4.1.

literature and that the empirically checked Krishna Swamy (1966) relation predicts a significant shift already at ∼5000 K (dwarf stars), comparable to that obtained by the BT-Settl $T-\tau$ relation of the 2600 K model.

Concerning the second point, we have calculated a series of models for low mass stars where we have applied a shift to the low temperature $T-\tau$ relations, to reproduce the observed mass-radius relation. The correction factor depends on the effective temperature. It is $\Delta\log(T/T_{\rm eff}) = 0$ at $\log(T_{\rm eff}/{\rm K}) = 3.675$, and it increases linearly to $\Delta\log(T/T_{\rm eff}) \sim 0.06$ dex (∼14%), at $\log(T_{\rm eff}/{\rm K}) = 3.5$. The resulting $T-\tau$ relations are shown in figure 2.13. Note that the correction is applied *only* to the $T-\tau$ relation and we use our own EOS and opacity to get the pressure structure in the atmosphere. The mass–radius calibration is shown in figure 2.14, where it is indicated as PARSEC v1.2S models. We checked that no shift is necessary at $T_{\rm eff}$ higher than $\log(T_{\rm eff}/{\rm K}) = 3.675$, since there is no need to alter the radii of stars with masses larger than $M = 0.7\ M_\odot$ at Solar metallicities.

We now look at the effects of this calibration on the colour–magnitude relations of VLMS in clusters. The results are illustrated by means of the PARSEC v1.2S+NBC models (red lines) overplotted in figures 2.3, 2.4, 2.5 and 2.6, for Praesepe, M 67, NGC 6398 and 47 Tuc, respectively. Notice that the same $T_{\rm eff}$-dependent shift obtained from the cal-

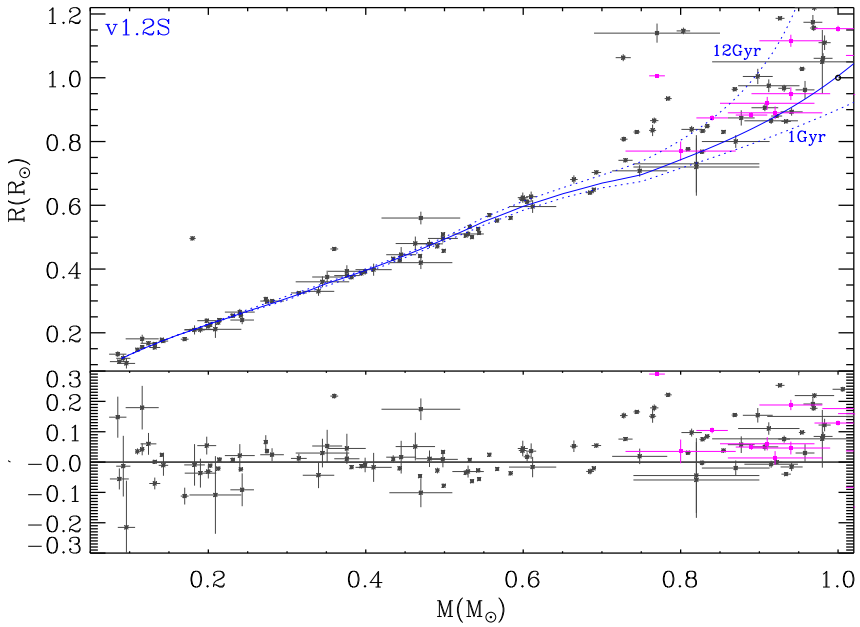

Figure 2.14: As figure 2.2, but for calibrated $T-\tau$ relation. We also plot isochrones with ages of 12 Gyr and 1 Gyr.

ibration with the mass–radius relation, is applied for all metallicities. Careful inspection of these plots reveals that the $T-\tau$-calibrated models provide an excellent fit to the lower MS in all these clusters, spanning a range of $\sim$2 dex in metallicity.

This result is remarkable. It is probably indicating that the problem at the origin of the too small radii in present VLMS models might be the same as that at the origin of their bad reproduction of the observed lower MS in cluster CMDs. Whether the present recipe of calibrating the available $T-\tau$ relations in the way we described is an acceptable solution, is another question, which we open for discussion. Of course, we are well aware that, at this stage, this is not more than "a recipe that works", rather than a recommendation we can do to stellar modellers. Work is necessary to clarify whether more realistic descriptions of stellar atmospheres – like for instance full 3D hydrodynamical models – may lead to any indication of this kind, or to alternative recipes.

Another aspect revealed by figures 2.3 and 2.4, is that the near-infrared CMDs of very low mass stars can be reproduced fairly well with the published $T-\tau$ relations, provided that one uses the correct bolometric corrections. In the very low mass regime, they are not as sensitive to $T_{\rm eff}$ as the optical CMDs. Indeed we emphasize that the optical CMDs should be considered as stronger diagnostic tools, together with the mass–radius relation which we used for the final calibration. However, we stress that, since the relation between

mass and near-infrared luminosity is also affected by the adopted $T-\tau$ relation (see the top-left panel of figure 2.3), the use of different models, although reproducing equally well the near-infrared CMDs, may lead to different estimates of the present-day mass function in star clusters.

2.5 Origin of the shifted $T-\tau$ relations: star-spots?

Finally, we would like to mention that possible origin of the modifications of the $T-\tau$ relation could be the photospheric spots in magnetic active stars (Spruit & Weiss 1986). These authors find that the general effect of the star spots in low mass stars is to reduce the luminosity L, while keeping the radius R and the temperature T_{us} of unspotted regions unchanged. Depending on the coverage of spotted regions (f_{spot}) and the temperature contrast between spotted and un-spotted regions ($x_{spot} = T_{spot}/T_{amb}$, 'amb' is for un-spotted regions), the flux would be dominated bu un-spotted regions at smaller f_{spot} and x_{spot}. Suppose, we fix f_{spot}, and the luminosity and radius (so the effective temperature is also fixed) of the models. If we reduce x_{spot}, to maintain the same luminosity, the temperature of un-spotted regions have to be increased. This would mimic the shifted $T-\tau$ relation as we have done, in which at the same effective temperature, we have to increase the temperature at every τ. Assuming the simplest model of Spruit & Weiss (1986), one obtains

$$L = 4\pi\sigma\,(1-f_{\rm e})\,R^2 T_{\rm us}^4 = 4\pi\sigma R^2 {T_{\rm eff}}^4 \tag{2.3}$$

where, $f_{\rm e}$ represents the effective blocking area of dark spots. For this model we have $\log(T_{\rm us}/T_{\rm eff}) = -\frac{1}{4}\log(1-f_{\rm e})$. Taking a value of $f_{\rm e} = 0.4$ (Jackson & Jeffries 2014), we obtain $\log(T_{us}/T_{\rm eff}) \sim 0.055$, which is not far from the effect we are considering at the lowest masses. Of course, in stellar models, the luminosity and radius also changes as $T-\tau$ relations change. Recently, the effect of star spots on the stellar models have been studied by Jackson & Jeffries (2014) and Somers & Pinsonneault (2015). Especially in Somers & Pinsonneault (2015), they have taken into account the star spots into the Yale Rotating Evolution Code in a consistent way. They have shown that the radii of very low mass stars are inflated by a quantity which is required to compare with the observations. They also show that the star spots make the stellar luminosity lower and effective temperature.

However, in the case of star spots, the colors are changed, while in our modification we

only shift the T–τ relation but keep the colors unchanged at fixed effective temperature. What's more, in Somers & Pinsonneault (2015), the authors claim that the spotted stars appear bluer in short bandpasses and redder in long bandpasses compared to un-spotted stars. For example, the $B-V$ color would be bluer in spotted stars. This would worsen the problem in the $B-V$ band (as discussed in section 2.6). Although it appears appealing to some of the problems in very low mass stars, it may not be the explanation we are looking for.

2.6 Blue band colours

As already discussed, we were able to obtain new stellar evolution models of low mass stars that can reproduce fairly well the observed MS of star clusters in a broad range of ages and metallicities. We show here that there remains some tension when we try to reproduce the optical colours, such as $B-V$, of selected nearby clusters, and discuss the possible origin of the remaining discrepancies.

In figure 2.15, we compare our models with one of the deepest CMD of M 67 in the V versus $B-V$ diagram (Yadav et al. 2008). The models plotted are the same as used in figure 2.4 and show the following characteristics. First of all, they are able to reproduce the main sequence down to about three magnitudes below the turn-off, but then they run bluer than the observed data at fainter magnitudes. It is also evident that the major difference between the models is due to the use of revised bolometric corrections rather than to the T–τ relation. The discrepancy with the data reaches $\delta(B-V) = 0.4$ at $V = 19$, even if our new models perform very well in other colours for the same cluster (as seen in figure 2.4).

To find the origin of this large discrepancy we first remind the reader that Yadav et al. (2008)'s data were obtained using a far-from-standard B filter, namely the ESO#842 filter available at the ESO/WFI camera in 2000. This B filter has a transmission curve strongly skewed towards the red and with a sharp cut-off at $\lambda > 5100$ Å, instead of the more extended (and slightly skewed to the blue) curve expected from a Johnson filter[5]. Indeed, the ESO#842 mean wavelength is close to 4637 Å, as compared to the 4460 Å

[5]This difference can be appreciated in figure 3 of Girardi et al. (2002a), where ESO#842 appears as the B filter in the ESO Imaging Survey (ESO/EIS) photometric system, and is compared to the (Bessell 1990) representation of the Johnson B filter.

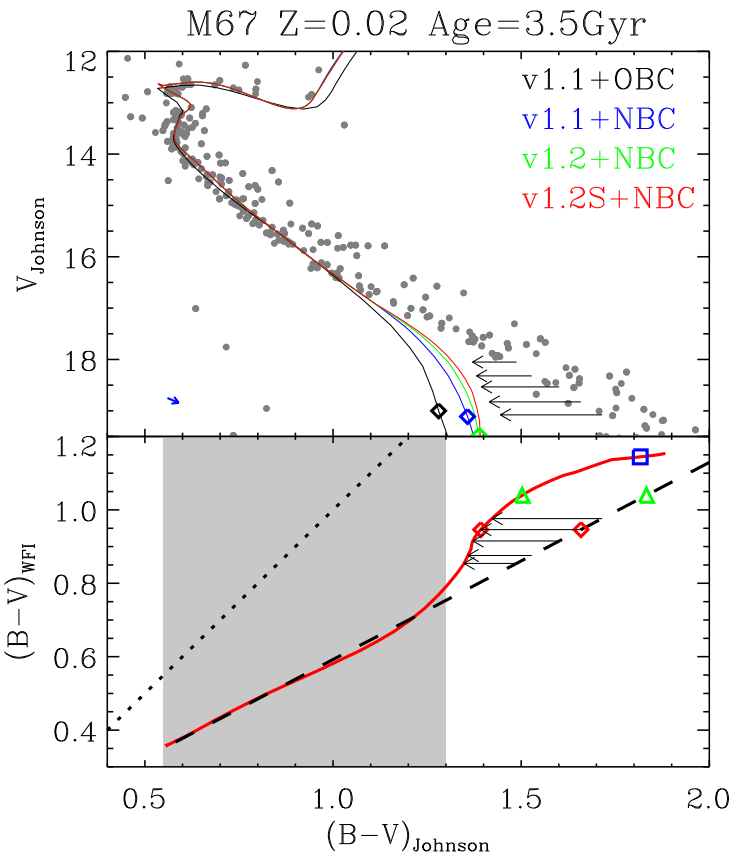

Figure 2.15: Top panel: The M 67 data from Yadav et al. (2008), in the V vs. $B-V$ diagram (gray dots). These data were originally collected in the ESO/Wide Field Imager (WFI) filters and then transformed to a Johnson system (see text). Our isochrones in the Johnson system are overlaid, using the same labels and parameters as in figure 2.4. Bottom panel: the difference between ESO/WFI $B-V$ and Johnson $B-V$, with our v1.2S isochrone shown as the red solid line. The black dashed line represents the linear transformation between these two systems as defined in the colour range of $0.55 < (B-V)_{\rm Johnson} < 1.3$ (grey shaded region) and extrapolated to redder colour (or lower masses). The horizontal black arrows indicate the corrections that should have been applied to the linear transformation, in order to more correctly represent the colours of the redder stars observed with ESO/WFI filters. The dotted line is the identity line.

of the Bessell (1990) B filter. When coupled to a V filter (with a mean wavelength of 5500 Å), ESO#842 provides a wavelength baseline of just 863 Å, as compared to the ∼1040 Å baseline expected from Johnson filters.[6]

Although collected in this very particular set of filters, Yadav et al. (2008) observations were then "calibrated" using linear transformations between their instrumental magnitudes and the magnitudes of stars in common with the Sandquist (2004) M 67 catalogue, being the latter in a well-calibrated Johnson system. As Yadav et al. 2008 show in their paper, the stars used to derive the transformations are bluer than $(B-V)_{\rm Johnson} = 1.4$ so that for redder (and fainter) stars this linear transformation becomes an extrapolation. This step is critical for obtaining reliable magnitudes of the fainter stars and its validity must be carefully assessed – especially in this case, where the B filter is very different from a Johnson one.

To clarify this point we show the transformation between the ESO/WFI $B-V$ and Johnson's $B-V$ [hereafter $(B-V)_{\rm WFI}$ and $(B-V)_{\rm Johnson}$, respectively] by the red thick line in the lower panel of figure 2.15. The colours in both systems were obtained using the ZAMS of our theoretical isochrones as a baseline, together with the Phoenix BT-Settl spectral library and the corresponding filter transmission curves. Even if it is not exactly the same method used by Yadav et al. (2008), this procedure shows that the transformation between the two photometric systems is far from being linear just redward of $(B-V)_{\rm Johnson} = 1.3$. The analogue of the linear transformation used by Yadav et al. (2008) is shown as a dashed line in the lower panel of the same figure. The dashed line is a linear fit of the actual transformation for $(B-V)_{\rm Johnson} \geq 1.3$. We evince from this exercise that, by extrapolating the linear transformation to stars redder than $(B-V)_{\rm Johnson} = 1.3$, one gets $(B-V)_{\rm Johnson}$ colours that are significantly redder than those expected from the actual transformation. A measure of the possible error in the $(B-V)_{\rm Johnson}$ colours of VLMS is shown by the horizontal arrows in the lower panel, which are also reported in the upper panel.

These comparisons with Yadav et al. (2008) data just emphasize the need of collecting data for VLMS in nearby open clusters using *standard* filters, together with a robust calibration of the photometry based on standard stars covering the widest-possible color range. Otherwise, any comparison with theoretical models (as those presented in figure 10

[6] These and other mean wavelengths are provided at the web interface `http://stev.oapd.inaf.it/cmd`, together with the theoretical isochrones.

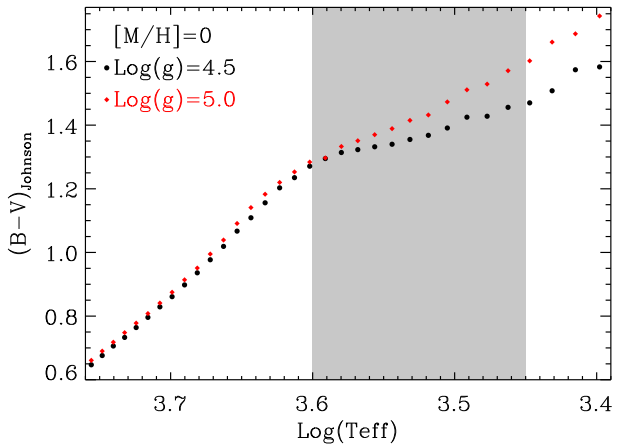

Figure 2.16: Temperature scale ($\log(T/\mathrm{K})$vs. $(B-V)_{\mathrm{Johnson}}$) for Phoenix BT-Settl models of [M/H]=0. Red and black dots are for $\log g = 5.0$ and 4.5 respectively. The grey area indicates the region where $B-V$ increases slowly as $\log(T/\mathrm{K})$ decreases.

of Yadav et al. 2008) may turn out to be misleading.

To reinforce this finding we plot in figure 2.16 the $(B-V)_{\mathrm{Johnson}}$ colours against $\log(T/\mathrm{K})$ of Phoenix models (from their website). Since below $T_{\mathrm{eff}} \simeq 4000\,\mathrm{K}$ the $B-V$ colours become quite flat, we expect a knee-like shape in the V vs. $B-V$ diagram, as seen in our plotted isochrones, but not in the "putative-Johnson" CMD from Yadav et al. (2008).

Another interesting – and more conclusive – comparison between models and data can be done using the Solar Neighbourhood data compiled by I. Neill Reid from Bessel (1990), Leggett (1992) and Dahn et al. (2002) catalogues[7]. The V vs. $B-V$ data in the Bessell system, are plotted in the left panel of figure 2.17, together with our models. We first notice that these data show the expected knee-like shape in the very low mass range. But we also notice that our best model mismatch the data by ~ 0.1 mag at $0.3\,M_{\odot}$. We suspect that this discrepancy originates from some molecular absorption bands around 4400 Å (AlH and NaH) being still unaccounted for in the models, as recently pointed out in Rajpurohit et al. (2013). Indeed, from their figure 3 we notice that the observed spectra run slightly below the Phoenix models at $\sim$ 4400 Å in the temperature range $3000 < T_{\mathrm{eff}}/\mathrm{K} < 3700$. This shows that the real $B-V$ should be slightly redder than those obtained by the Phoenix models, but more work is needed to check if the difference really amounts to ~ 0.04 dex in flux, as expected from the observed mismatch.

Finally, the Solar Neighbourhood V vs. $U-V$ data in the Bessell system, are plotted

[7] http://www.stsci.edu/~inr/cmd.html

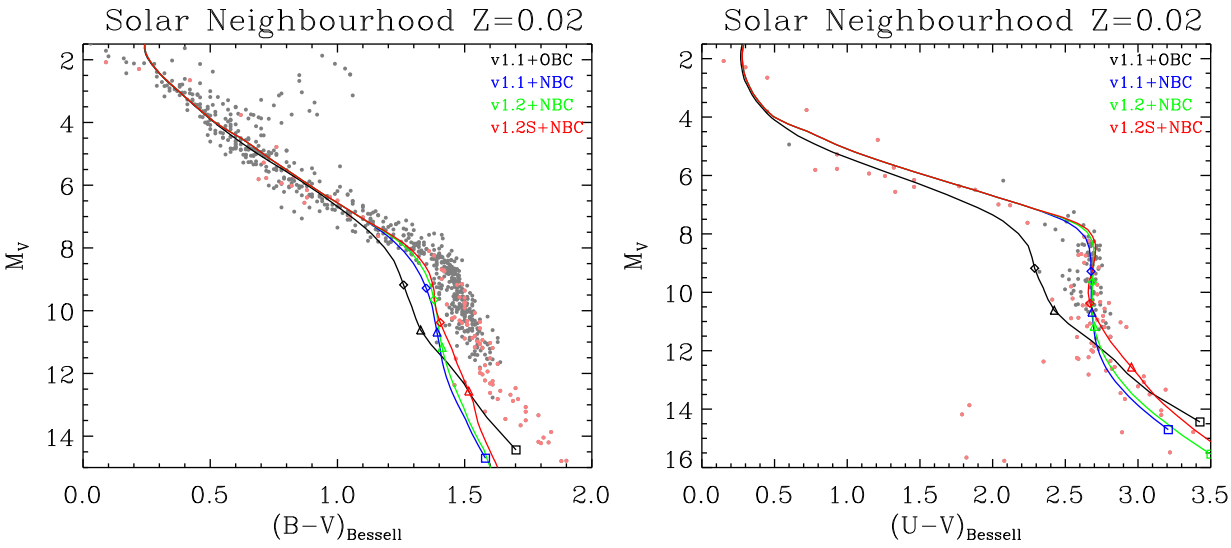

Figure 2.17: Solar neighbourhood stars in the M_V vs. $B-V$ and M_V vs. $U-V$ diagrams. The data points are from the CNS3 star sample; stars within 8 pc of the Sun are marked with pink dots. The labels are the same as in figure 2.3. The absolute magnitudes are in the Bessell photometric system (Bessell 1990). The galactic reddening is not considered in this plot. The isochrones are for $Z = 0.02$. Although the stars have different ages, their evolution is quite slow, thereby we only show the isochrones of 1 Gyr.

in the right panel of figure 2.17, together with our models. In contrast to the $B-V$ colour, our new models can fit quite well the $U-V$ knee-like shape at $U-V \simeq 2.7$, starting at $M_V \gtrsim 8$ and extending down to $M_V \simeq 11$. There remain some possible mismatch at still fainter magnitudes, but the data are too scarce for drawing definitive conclusions.

Pleiades After the publication of our paper on very low mass stars, Kamai et al. (2014) presented new BVI $_C$ photometry of low-mass Pleiades stars. The filters they use are well-matched to the standard Johnson and Kron-Cousins systems. Melis et al. (2014) presented the VLBI parallax distance for Pleiades of 136.2±1.2 pc (corresponding to an intrinsic modulus of 5.671 mag). We compare our models with the new observation for Pleiades in figure 2.18. We see the expected knee-like feature at V∼15 mag. Below this magnitude the discrepancy between our calibrated model and observation is less than 0.2 mag.

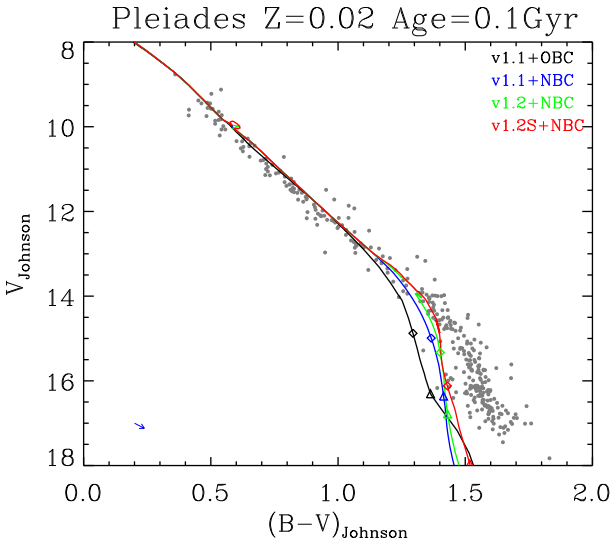

Figure 2.18: Comparsion with the observation data for Pleiades from Kamai et al. (2014). A reddening of $E_{B-V} = 0.02$ mag (Kamai et al. 2014) and an intrinsic distance modulus of 5.671 mag (Melis et al. 2014) are applied.

2.7 Data release

The VLMS models $M < 0.75\ M_{\odot}$ presented in this theis turn out to represent a significant improvement over the previous versions. The v1.2, by using a more realistic $T-\tau$ relation, clearly go in the direction of presenting larger radii and cooler $T_{\rm eff}$, which is indicated by the data. Moreover, the "calibrated" v1.2S models fit very well the mass-radius and CMD data of VLMS in the Solar Neighbourhood and in star clusters over a wide range of metallicities, hence representing a good alternative to being applied in a series of astrophysical problems, going from the derivation of parameters of star clusters and transiting planets, to the interpretation of star counts in the Galaxy in terms of both their mass function and density variations across the galactic disk and halo.

Therefore, we are releasing these two new sets of evolutionary tracks through our web servers at `http://stev.oapd.inaf.it`. These VLMS models replace those in the previous database of PARSEC isochrones (namely v1.1, Bressan et al. 2012), producing the isochrones' version v1.2 and v1.2S. They become available using both the previous BC_{λ} tables (OBC), and the revision based on BT-Settl models (NBC), for a wide variety of photometric systems, through our web interface `http://stev.oapd.inaf.it/cmd`. For guidance, Table B.1 presents a summary of the main characteristics of these models, and of the other models that will be introduced later in this thesis.

Chapter 3

Massive stars: evolutionary tracks

3.1 Background

Massive stars play an important role in the evolution of galaxies (Oey & Clarke 2007). They are the most important stellar sources of ionizing and dissociation photons (Schaerer et al. 2011; Kimm & Cen 2014; Dale et al. 2012; Cai et al. 2014; Hollenbach & Tielens 1999; Yu et al. 2015). They inject a significant amount of kinetic energy through powerful stellar winds (Mackey et al. 2014). They are among the main drivers of metal and dust enrichment in galaxies when they explode as core collapsed supernovae (SNe) (Sarangi & Cherchneff 2015; Schneider et al. 2004). They are thus very important sources of feedback to the ambient ISM (Dale et al. 2013). Last but not least, most of our information on the ongoing star formation rates across the Universe heavily relies on our detailed knowledge of their properties (Bruzual & Charlot 2003; Kennicutt 1998). Amongst different types of massive stars (O, LBV, RSG, WN, WC), there is the "Conti scenario" in the Milky way as summarized in Crowther (2007). I also repeat here:

- For stars with initial mass larger than $\sim 75 M_{\odot}$:
  O $\rightarrow$ WN(H-rich) $\rightarrow$ LBV $\rightarrow$ WN(H-poor) $\rightarrow$ WC $\rightarrow$ SN Ic.

- For stars with initial mass of $\sim 40 - 75 M_{\odot}$:
  O $\rightarrow$ LBV $\rightarrow$ WN(H-poor) $\rightarrow$ WC $\rightarrow$ SN Ic.

- For stars with initial mass of $\sim 25 - 40 M_{\odot}$:
  O $\rightarrow$ LBV/RSG $\rightarrow$ WN(H-poor) $\rightarrow$ SN Ib.

Because of their relevance for so many fields of astrophysics, massive stars have been the subject of many observational and theoretical investigations that are impossible to list here. Understanding their evolution is challenged by the complexity of several physical phenomena, as recently reviewed, for example, by Martins & Palacios (2013) who compare STERN (Brott et al. 2011), Geneva (Ekström et al. 2012), FRANEC (Chieffi & Limongi 2013), Padova (Bertelli et al. 2009), MESA (Paxton et al. 2011) and STAREVOL (Decressin et al. 2009) evolutionary tracks of massive stars. Martins & Palacios (2013) find that, apart from the inclusion of rotation, the main differences among the models computed by different authors can be attributed to the different treatments of convection and mass-loss, with the former process being more important in the domain of the less massive stars. It is worth noting that the Padova tracks (Bertelli et al. 2009) analyzed by Martins & Palacios (2013) are still those presented in Fagotto et al. (1994) and Bressan et al. (1993). Since then, there have been many advances both in the basic input physics (opacities, equation of state, nuclear reactions) and in the mass-loss theory (and observations), and these called for a substantial revision of the Padova code. But, while low and intermediate mass stars were systematically updated, with the last version being PARSEC models (Bressan et al. 2012, and refs. therein), massive stars have not been updated since then.

In this chapter, we present the new evolutionary tracks of massive stars computed with PARSEC. Besides the basic input physics, which is described elsewhere (Bressan et al. 2012, and refs. therein), the main novelties concern the recipes adopted for the mass-loss rates and the spectral energy distributions used to convert the tracks from the theoretical to the observational plane. Concerning mass-loss, there have been many efforts over the past years to determine/predict the mass-loss rates of massive stars across different spectral types and metallicities. It is now widely accepted that hot massive blue supergiants (BSG) and Wolf-Rayet (WR) stars lose a prominent amount of their mass through line-driven stellar winds and that the mass-loss rates show a simple scaling law with the metallicity (Castor et al. 1975; Kudritzki & Puls 2000; Nugis & Lamers 2000; Vink et al. 2000, 2001; Muijres et al. 2012a; Crowther 2007; Smith 2014). In Luminous Blue Variable (LBV) stars, there is evidence that an important mode of mass-loss is through eruptive mass-loss, that may contribute as much as or even more than the steady stellar wind (Smith 2009). In this phase the mass-loss rate may easily reach

a few of $10^{-4} M_{\odot}\, yr^{-1}$ (Lamers 1989). This eruptive mechanism is still unknown but the observed rates could be explained by a super-Eddington wind (Smith & Owocki 2006), or by non-disruptive hydrodynamic explosions (Barsukova et al. 2014). Interestingly, LBV stars are found near the so-called Humphreys-Davidson limit (Humphreys & Davidson 1979) which delimits the forbidden region above which only very few stars are observed in the Hertzsprung-Russell (HR) diagram of the Galactic massive stars. In this respect, a remarkable result of recent investigations is that the mass-loss rates could be enhanced by a significant factor when the stars approach the Eddington luminosity (Gräfener & Hamann 2008; Vink et al. 2011), which is known to happen near the Humphreys & Davidson (1979) limit. For the later spectral types there are larger uncertainties both on the mechanisms and on the strength of the mass-loss rates. In red supergiants (RSG) one customarily adopts the observational parametrization by de Jager et al. (1988), but the mass-loss rates in this phase are known to be uncertain by a large factor (Salasnich et al. 1999; Meynet et al. 2015). As in less massive Asymptotic Giant Branch (AGB) stars, dust formation on the circumstellar envelopes could be one of the possible mechanisms responsible for this enhancement (van Loon et al. 2005).

Concerning the observations of the very massive stars, I did not compare our new models with the observation in my Ph.D. projects, thus here I only give some literature that summarize the progress on the observation. A very good review on massive stars in the local group galaxies is Massey (2013). A very recent review is Crowther (2015) which overviewed the known WR population of the Milky Way. Some other papers on searching for massive stellar populations are the following. Kiminki et al. (2015) presented 79 new spectral classified O- and B-type stars in the star-forming complex Westerhout 3 in our Galaxy. The largest campaign searching for massive stars is the VLT-FLAMES survey (Evans et al. 2005, and refs. thereafter). So far, they have obtained high-quality spectra for over thousand stars (over 800 stars in the VLT-FLAMES survey and over 900 stars in the VLT-FLAMES Tarantula survey) in the Galaxy and in the Magellanic Clouds. Recent observations from Crowther et al. (2010) and Bestenlehner et al. (2011) suggest the existence of very massive stars (VMSs), with initial masses up to 350 $M_{\odot}$, e.g., R136A in the LMC cluster (Crowther et al. 2010, $\sim 300 M_{\odot}$). These observations would not just help us understand the massive evolution better, but also help us reveal the initial mass function in star-forming regions.

In this chapter, we describe our stellar evolution models for massive stars, with particular care to the description of the recipes adopted for the mass-loss rates. We then compare the new models with our previous models and with one set among the most recent models found in literature, FRANEC (Chieffi & Limongi 2013). In the next chapter we will describe in detail the adopted atmosphere models and the procedure used to obtain as much as possible homogeneous sets of bolometric correction tables, and we will discuss the resulting colour-magnitude diagrams predicted from the new evolutionary tracks and isochrones.

Our evolutionary tracks can be downloaded from http://people.sissa.it/~sbressan/parsec.html, and the isochrones can be downloaded from http://stev.oapd.inaf.it/cgi-bin/cmd.

3.2 Stellar evolutionary tracks for massive stars

We compute new track of massive stars with the PARSEC code for a wide range of initial metallicities and for initial masses from $M_{\rm ini}$=14 $M_\odot$ to $M_{\rm ini}$=350 $M_\odot$. The evolution begins from the pre-main sequence phase and ends at central Carbon ignition. The new evolutionary tracks complement the already existing models of intermediate and low mass stars.

The basic ingredients of PARSEC code have been extensively described in chapter 1.5. The most important update in the PARSEC code for calculating the massive stellar evolutionary tracks is the mass loss rate. Thus in the following we discuss them in detail.

3.2.1 Mass loss rates

At Solar metallicity, the mass-loss phenomenon is known to dominate the evolution of stars for initial masses $M_{\rm ini} \geq 30 M_\odot$. We account for this process following recent prescriptions found in the literature for the different spectral types. In the blue supergiant phase, for $T_{\rm eff} \geq 12000$ K, we adopt the relations provided by Vink et al. (2000, 2001). This formulation (R_{V01}) shows an almost linear overall dependence of the mass-loss rates on the metallicity, $\dot{M} \propto (Z/Z_\odot)^{0.85} M_\odot/yr$. In the supergiant phases with $T_{\rm eff} < 12000$ K we use the mass-loss rates provided by de Jager et al. (1988), R_{dJ}, assuming the same dependence on the surface metallicity of R_{V01}. For WR stars we use the Nugis & Lamers

(2000) formalism, R_{NL}. They also provide a dependence on the stellar metallicity. The definition of the WR phases is provided below (see section 4.4).

An aspect which is relevant for the more massive stars concerns the transition between the O-phase, the LBV/RSG phase and finally the WR phase and, most importantly, the dependence of this transition upon the metallicity of the stars. For example, in the old Padova models, e.g., Bressan et al. (1993), the transition to the super-wind phase corresponding to the LBV stars is artificially set at the stages when the models cross the Humphreys-Davidson instability limit (Humphreys & Davidson 1979) in the HR diagram. This is justified by the evidence that Galactic and Magellanic Clouds massive stars near this limit show mass-loss rates that may reach $\dot{M} \simeq 10^{-3} M_{\odot}/yr$. However, while the Humphreys-Davidson limit is an observed property of the HR diagram of massive stars in near Solar environments, it is used independently from the metallicity of the galaxy, in spite of the fact that the mass-loss rates themselves do depend on the abundance of heavy elements (Kudritzki & Puls 2000; Puls et al. 2000; Mokiem et al. 2007; Smith 2014). This approximation becomes critical at very low metallicities.

From the theoretical side, recent detailed studies of radiative wind models (Gräfener & Hamann (2008) and Vink et al. (2011)) show that the mass-loss rates are strongly enhanced when the stars approach the electron scattering Eddington limit

$$\Gamma_e = \frac{L\kappa_{es}}{4\pi cGM} = 1 \tag{3.1}$$

Since for the most massive stars at Solar metallicity this may happen near the Humphreys-Davidson limit, the above formalisms could provide a modern description of the transition from O-type through LBV/RSG-type to WR-types (Vink & Gräfener 2012). We thus include in PARSEC the recent formulation of mass-loss rates by Vink et al. (2011). The resulting HR diagram of a few selected evolutionary tracks for about Solar metallicity is shown in the upper panel of figure 3.1. For purposes of clearness, we do not plot the pre-main sequence phase. The colours along the tracks represent the strength of the mass-loss rates as indicated in the inset scale. In the figure, the thick black lines mark the so-called Humphreys-Davidson limit (Humphreys & Davidson 1979) which delimit the forbidden region above which only very few stars are observed in the HR diagram of the Galactic massive stars. As shown in the figure, the main sequence of the most massive stars extends

up to the Humphreys-Davidson limit. Eventually, the stars may encompass this limit but the time spent in this region is very short because the mass-loss rate becomes so high that the stars rapidly lose their envelopes and turn into the hotter region of the HR diagram. We stress that this is not a result of an *ad hoc* assumption for the mass-loss rate, but a direct result of the application of the newly adopted relations of the mass-loss rates. Near the Humphreys-Davidson limit, Γ_e rises close to 1 and, as described in Vink et al. (2011), when Γ_e is larger than 0.7, the mass-loss dependence on Γ_e becomes high and, correspondingly, the mass-loss rates are significantly enhanced. With this formulation, the boosting of the mass-loss rate at the highest masses ($M_{\rm ini} \geq 150 M_{\odot}$) is effective already from the beginning of the main sequence and, because of the large mass-loss rates, they evolve almost downward vertically in the HR diagram. Interestingly, the luminosity of the tracks with the higher masses ($M_{\rm ini} \geq 150 M_{\odot}$) falls with time much more than those of the less massive ones. This is caused by the *over-luminosity* with respect to the main sequence mass – luminosity relation which, being larger at larger masses, results in larger values of Γ_e. Thus, the evolved brightest massive stars are not necessarily those with the largest initial masses.

The Γ_e dependence of the mass-loss rates of O-type supergiant stars has not yet been studied for different galactic environmental conditions, apart from the analysis of the effects of CNO abundances (Muijres et al. 2012b). A more thorough analysis in a broad metallicity range, $10^{-3}\ Z_{\odot} \leq\ Z \leq\ 2\ Z_{\odot}$, has been performed by Gräfener & Hamann (2008), but only for the case of WR stars. In particular, Gräfener & Hamann (2008) show that the dependence of mass-loss rates on the metallicity is also a strong function of Γ_e. While at low values of Γ_e the mass-loss rates obey the relation of $\dot{M} \propto (Z/Z_{\odot})^{0.85} M_{\odot}/yr$, at increasing Γ_e the metallicity dependence decreases, and it disappears as Γ_e approaches 1. In the absence of a more comprehensive analysis of the dependence of the mass-loss rates on the metallicity and Γ_e, and since there is a continuity between the models provided by Vink et al. (2011) and those of WNL stars provided by Gräfener & Hamann (2008) (see discussion in Vink et al. (2011)), we assume in PARSEC that the scaling with the metallicity obeys the following relation

$$\dot{M} \propto\ (Z/0.02)^{\alpha} \tag{3.2}$$

with the coefficient α determined from a rough fit to the published relationships by Gräfener & Hamann (2008):

$$\alpha = 2.45 - 2.4 * \Gamma_e \qquad (2/3 \leq \Gamma_e < 1) \tag{3.3}$$

and with the supplementary condition $0 < \alpha \leq 0.85$. In summary, our algorithm for the mass-loss is the following. Besides the already specified mass-loss rate formulations (R_{V01}, R_{dJ} and R_{NL}) we compute also R_{Γ_e} from the tables provided by Vink et al. (2011), but we scale the latter value with the metallicity, using equations (3.2) and (3.3). During the BSGs and LBVs phases the basic mass loss rate adopted is R_{V01}. However, since, because of the effects of Γ_e, this can be encompassed by R_{Γ_e} and in order to secure a smooth transition, we adopt the maximum between R_{V01} and R_{Γ_e}. Toward the red supergiant phase we use R_{dJ}, but again, since this is an empirical rate parameterized in such a way that it should hold on a broad region of the HR diagram and it likely underestimates the mass loss rates of luminous yellow super-giants (Salasnich et al. 1999), we compare it with R_{Γ_e} and take the maximum value. In the WR phases we consider the Nugis & Lamers (2000) formulation.

The HR diagram of a few selected evolutionary tracks for Z=0.008 is shown in the middle panel of figure 3.1. We note here a significant decrease of the mass-loss rates, at a given mass. In particular while at Z=0.02 the models of $M_{\rm ini}$∼120$M_\odot$ and $M_{\rm ini}$∼150$M_\odot$, rapidly turn their main sequence evolution to higher effective temperatures, at Z=0.008 the mass-loss rates are not high enough to prevent the tracks from entering into the forbidden region. Nevertheless, the tracks burn Hydrogen around the Humphreys-Davidson limit until, near central Helium ignition Γ_e becomes large and after performing a rapid excursion within the forbidden region, they turn into the blue part as WR stars. At even lower metallicities, the mass-loss rates decrease, unless the star is near the Eddington limit with Γ_e ∼1, and the location of the predicted Humphreys-Davidson limit shifts to higher luminosities. For example, at Z=0.001 in the lower panel of figure 3.1, the upper main-sequence widens significantly and the more massive stars evolve into the "forbidden" region even during the H-burning phase, because of their very large convective cores. They may also ignite and burn central Helium as "red" supergiant stars.

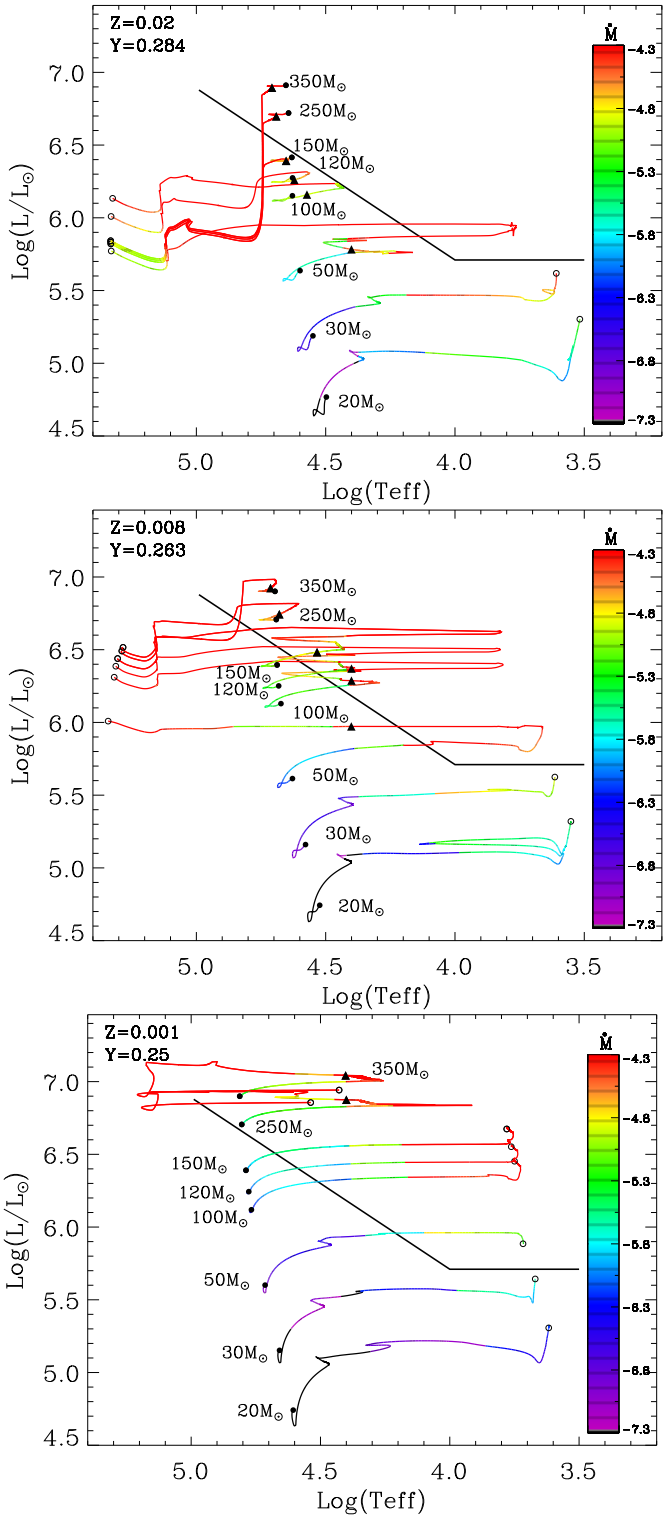

Figure 3.1: Selected evolutionary tracks for massive stars with Z=0.02 (upper panel), Z=0.008 (middle panel) and Z=0.001 (lower panel). The mass-loss rates are indicated with the colour bar. The thick black straight lines represent the Humphreys-Davidson limit (Humphreys & Davidson 1979) which delimits the forbidden region above which only very few stars are observed in the Hertzsprung-Russell (HR) diagram of the Galactic massive stars. The big solid and empty circles indicate the ZAMS and the end points of the tracks respectively. The triangles mark the beginning of WR phase.

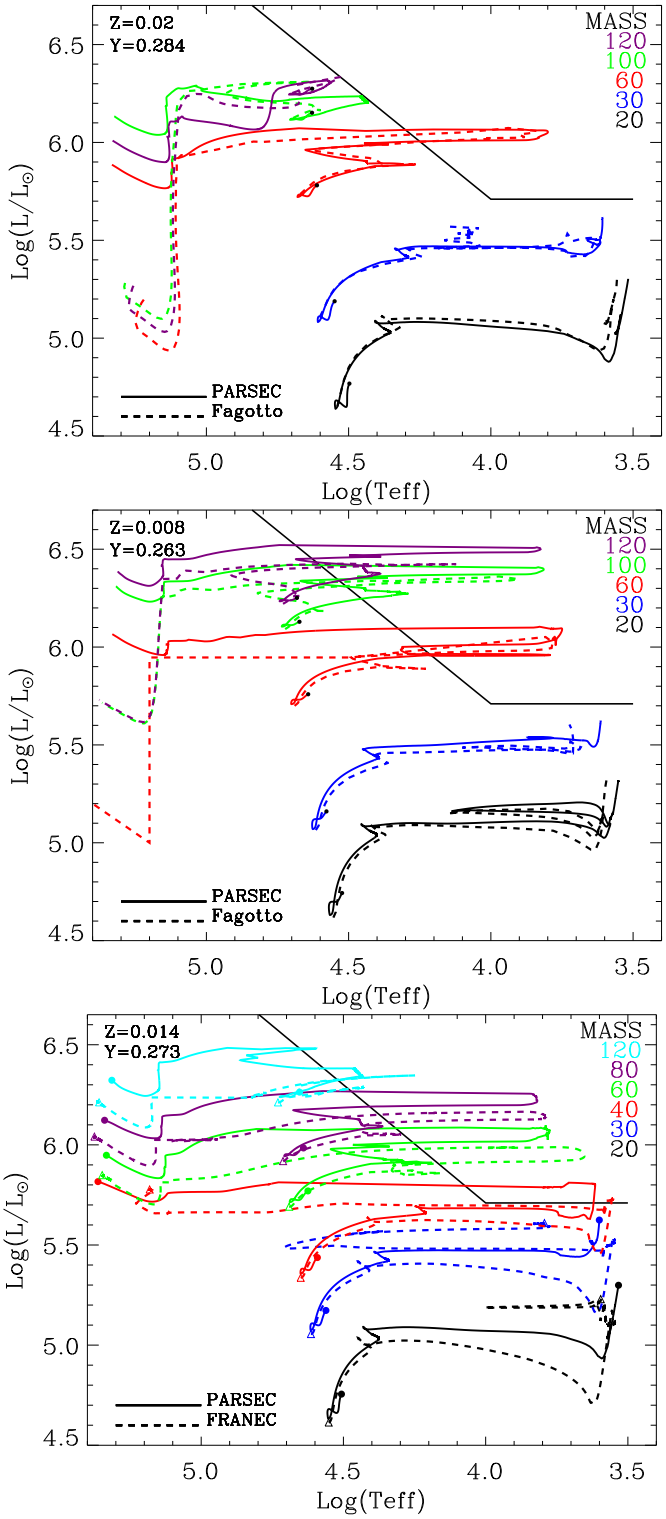

Figure 3.2: Upper and middle panels: comparison with previous releases of Padova evolutionary tracks (dashed lines, Fagotto et al. 1994; Bressan et al. 1993) with $Z = 0.02$ (upper panel) and $Z = 0.008$ (middle panel). Models with different masses are indicated with different colors. Notice that Helium abundances are slightly different between the two different sets illustrated: $Y = 0.263$ for PARSEC; $Y = 0.25$ for Fagotto et al. (1994); Bressan et al. (1993). Lower panel: comparison with the FRANEC Solar abundance ($Z = 0.01345$) models without rotation (dashed-lines, Chieffi & Limongi 2013). The Humphreys-Davidson limit is also drawn as in figure 3.1.

3.2.2 Comparison with previous releases

The current set of massive stars supersedes the old one adopted in several popular studies since 20 years (Bressan et al. 1993; Fagotto et al. 1994, hereafter BF+). With respect to BF+, the new models have a significantly finer mass spacing and extend up to a higher upper mass limit. The computed masses range from 14 to 20 $M_{\odot}$in steps of 2 $M_{\odot}$, then up to 100 $M_{\odot}$in steps of 5 $M_{\odot}$and finally 120, 150, 200, 250, 300, 350 $M_{\odot}$. This allows for a quite better interpolation in ages and masses and a sampling of different initial mass function up to larger initial masses. Simple stellar populations can now be sampled with a higher accuracy than before and with more suitable mass and time-steps. The new tracks include also the pre-main sequence phase that begins when the central temperature of the protostar becomes larger than $\log(T_c/K) = 5.3$. No mass accretion is accounted for during the pre-main sequence phase.

To summarize the differences brought by the adoption of the updated physics input we compare the new tracks with those of the previous Padova release, in the upper and middle panels of figure 3.2, for $Z = 0.02$ and $Z = 0.008$ respectively. Besides the presence of the pre-main sequence in the new tracks, which for purposes of clarity is not shown, a few general trends can be seen in the figure. At Z=0.02, the Zero Age Main Sequence (ZAMS) is similar. Note that the old tracks do not include the pre-main sequence phase. The main sequence termination is only slightly hotter in the new tracks, likely because of differences in the underlying opacities. The red supergiant phase is slightly cooler in the new tracks, but the differences are barely significant. We remind that in BF+ the density inversion (arising in the inefficient region of the convective envelope) was inhibited in the computation of massive star tracks. In a later revision of the tracks (Girardi et al. 2000) it was inhibited at all masses. As discussed in Alongi et al. (1993), a density inversion may develop in the external inefficient convection zones because of the requirement of the hydrostatic equilibrium in a region with a large super-adiabatic real temperature gradient (assuming typical values of the mixing length parameter). This situation which should lead to a Rayleigh-Taylor instability or even a significant increase in the mass-loss rate, may give rise to numerical instabilities which preclude the computation of the track. To inhibit the density inversion one may use a mixing length parameter proportional to the density scale height (H_{ρ}) which, by rendering convection more efficient in the region where the density has a relative maximum, prevents a large super-adiabatic real temperature

gradient. Alternatively one may impose that the real temperature gradient is limited by $\nabla_T \leq \nabla_{T_{\max}} = \dfrac{1-\chi_\mu \nabla_\mu}{\chi_T}$, which is the choice made since BF+. This also simulates a more efficient convection and prevents the development of numerical instabilities. However since a larger convective efficiency results in a hotter red giant track, and since BF+ red giant tracks of intermediate and low mass stars compared well with the corresponding observed colours, we follow their method and inhibit density inversion only for the most massive stars. Thus the most massive red super-giants have effective temperatures that are slightly hotter than those obtained by allowing density inversion to occur. A detailed analysis of this effect is clearly needed, but likely it must also take into account effects of dusty circumstellar envelopes which are known to affect the colours of RSG stars.

The mass-loss rates adopted here are less efficient already at $M_{\rm ini}$=30$M_\odot$. At this mass, the star ignites Carbon as a red giant while in BF+ the star is already moving toward the hot region of the HR diagram. This effect is more striking in the more massive stars, for those reaching the WR stages. Comparing the two models of 60 $M_\odot$we see that while the H-burning and the central Helium ignition phases are pretty similar, the final WR phase is very different. The mass-loss adopted for the WR stages in BF+ is significantly larger than that adopted here and the star ends with a luminosity which is about one order of magnitude lower.

At higher masses, $M_{\rm ini}$=100 and 120 $M_\odot$, there are significant differences already in the core H-burning. The mass-loss rates are initially higher in the BF+ models, but when the effects of Γ_e become important, the mass-loss rates become comparable and the tracks evolve along the similar path. There remain a large difference in the mass-loss rate adopted in the advanced WR stages.

We stress again that in BF+ models the mass-loss is arbitrarily enhanced when the stars approach or encompass the Humphreys-Davidson limit, while in the current models the mass-loss enhancement is a result of the photospheric conditions. In this respect, it is very interesting to note the similarity between the tracks of $M_{\rm ini}$=60 $M_\odot$that can be taken as representative of the fact that the mass-loss enhancement is no more imposed as before, but it is instead a natural consequence of the *photospheric* conditions.

The comparisons with the models of Z=0.008, typical of the Large Magellanic Cloud, confirm the previous picture. The ZAMS is pretty similar, but now the effects of a lower metallicity become visible, since the normalization metallicity for the mass-loss rate has

been assumed to be Z=0.02. In the old models, the metallicity dependence was slightly lower, $\dot{M} \propto (Z/0.02)^{0.5}$, and the mass-loss rates at Z=0.008 were about 40% larger than in the current models, keeping other parameters fixed. Thus, the new models evolve at slightly higher luminosity until the effects of Γ_e become important. Again there is a striking similarity in the turnover of the effective temperature in the models that overcome the Humphreys-Davidson limit. As before, in the final WR stages the stars evolve at a significantly higher luminosity than that of the old models. We note that, while in the advanced WR stages the luminosities of the new models are significantly higher, the corresponding lifetime is more or less unchanged ($\sim 0.1\,\mathrm{Myr}$ for $100\,M_\odot$ models). This means that the new models should contribute far more to the hard ionizing photons than the old ones. This will be the subject of a forthcoming paper dedicated to the integrated properties of young star clusters.

For the comparison with models by other groups, we select the evolutionary tracks without rotation computed with the FRANEC code (Chieffi & Limongi 2013). The HR diagram is shown in the lower panel of figure 3.2. The FRANEC models (dashed lines) are for a composition of $Z = 0.01345$ and $Y = 0.265$ while PARSEC models (solid lines) are for a slightly different chemical composition, $Z = 0.014$ and $Y = 0.273$. They adopt a mixing-length parameter $\alpha \equiv \Lambda/H_p = 2.3$ and a core overshooting region of $0.2H_p$ (Chieffi & Limongi 2013; Martins & Palacios 2013). One of the major difference is the presence of big blue loops in the FRANEC $20\,, 30$ and $40\,M_\odot$ models, while the big blue loops are absent in our models. In this respect, we note that the main sequence termination of our models is significantly cooler and more luminous than that of FRANEC models. This is particularly evident in the model of $M_{\rm ini}$=$40\,M_\odot$ and it is indicative of a larger central mixing during the main sequence phase of our models, which is known to disfavour the occurrence of blue loops. The larger extension of the loops in the FRANEC models could also be due to their use of the Ledoux criterion for the definition of the borders of the intermediate unstable regions. It is well known that the Ledoux criterion inhibits the development of the intermediate convective regions within the Hydrogen profile, at the end of the H-burning phase, favouring a deeper penetration of the convective envelope when the stars move into the RSG region. This is an important issue deserving further investigation. Preliminary models computed adopting either the Schwarzschild or the Ledoux criterion in the Hydrogen chemical composition profile, confirm that the main

cause of the inhibition of blue loops is the extent of core overshooting (or another kind of extended mixing) during main Hydrogen burning phase. With a slightly reduced core overshooting, also PARSEC models with the Schwarzschild criterion show extended blue loops (Tang et al. 2015 in preparation).

We also see that the behavior of the tracks within the Humphreys-Davidson region is very similar. In both cases, the models abandon this forbidden region after losing a significant fraction of their mass. In both cases, the mass-loss must be enhanced, but the invoked mechanisms are different: Chieffi & Limongi (2013) invoke the dust mass-loss enhancement (van Loon et al. 2005), while we invoke the Γ_e mass-loss enhancement.

3.3 Discussions and Conclusions

We present new evolutionary tracks of massive stars for a broad range of metallicities, $0.0001 \leq Z \leq 0.04$ and for initial masses up to $M_{\rm ini}$=350$M_{\odot}$. At super-Solar metallicity, the models extend up to $M_{\rm ini}$=200$M_{\odot}$ (Z=0.03) and $M_{\rm ini}$=150$M_{\odot}$ (Z=0.04), respectively. The new models complement the already published PARSEC data base (Bressan et al. 2012) and supersede the old Padova evolutionary tracks of massive stars which are more than 20 years old. The stellar models are evolved from the pre-main sequence phase to the central Carbon ignition. The mass grid is very well sampled and it is fully adequate to perform detailed investigations of very young stellar systems both from the point of view of the resolved populations and from their integrated properties.

We revise the scheme adopted for including the mass-loss rate in the evolution of massive stars, by combining recent recipes found in the literature. Among the new recipes, particularly important is the enhancement of the mass-loss rate when the luminosity approaches the Eddington limit. We show that with the recent formulation by Vink et al. (2011), the models naturally reproduce the observed Humphreys-Davidson limit observed in the Galactic and LMC HR diagrams. In previous Padova models this limit was used as a threshold to enhance the mass-loss rates, independently from the metallicity. In this thesis, the role of the metallicity is described by means of a simple recipe derived from the models presented in Gräfener & Hamann (2008). The metallicity dependence of the mass-loss rate is now described by a power law with an exponent α which depends on Γ_e (equation (3.1)), the ratio between the stellar luminosity and the Eddington luminosity.

When Γ_e approaches unity the metallicity dependence drops significantly, allowing for relatively high mass-loss rates also in stars of low metallicity. At lower values of Γ_e the usual exponent is recovered, α=0.85. While the models of Gräfener & Hamann (2008) refer particularly to the WR phase, it has already been shown that there is a continuity between the new Vink et al. (2011) formalism and the Gräfener & Hamann (2008) results for WNL stars. The result of the new mass-loss formulation is that the Humphreys-Davidson limit shows a clear dependence with metallicity and it even disappears at very low metallicities.

Compared to our previous models with the same metallicity (Fagotto et al. 1994; Bressan et al. 1993), the major difference concerns the WR phases. The new models evolve in the late WR stage, at $\log T_{\rm eff} > 5.0$, with luminosities which are significantly higher than those of the old Padova tracks (~ 0.9 dex in $\log L/L_{\odot}$). These differences result from the different mass-loss recipes used in the advanced WR phases. Since the lifetimes of the models in this phase remain more or less the same, the new models should contribute much more to the hard ionizing photons. At lower metallicity, Z$\leq$0.008, the new mass-loss formulation introduces significant differences even in the earlier phases. Our models compare well with the recent evolutionary tracks of non-rotating stars of similar metallicity, computed with FRANEC (Chieffi & Limongi 2013).

A preliminary comparison of the new models with the colour-magnitude diagrams of star-forming regions in nearby low metallicity dwarf irregular galaxies, has already been performed in Tang et al. (2014). The new models of massive stars will be used to compute the integrated properties of young star forming regions (Obi et al. in preparation). The full sets of evolutionary tracks can be downloaded from `http://people.sissa.it/~sbressan/parsec.html`. The isochrones can be downloaded from `http://stev.oapd.inaf.it/cgi-bin/cmd`.

Chapter 4

Massive stars: atmosphere models

4.1 Background

In chapter 3, we have discussed the evolutionary tracks of massive stars, where only stellar interior is concerned. Compared to stars of lower masses, the main difference is just that the stellar mass is no more conserved. The other main part of studying massive stars is the atmosphere. To compare with the observation, we need the atmosphere models to predict the stellar magnitudes and colours. They are equally important for the interpretation of observed properties of massive stars. For stars with negligible mass-loss, a comprehensive stellar atmosphere library usually adopted is ATLAS9 (Castelli & Kurucz 2004), consisting of plane parallel models in local thermodynamic equilibrium. This library is particularly suitable for $\sim$ A-, F- and G-type stars. For cool giants, where the plane parallel and non-LTE (non-local thermodynamic equilibrium) approximations must be relaxed, comprehensive stellar atmosphere libraries are provided by Phoenix (Allard & Homeier 2012, and references therein) and MARCS (Gustafsson et al. 2008) projects. For hot stars with high mass-loss rates a number of atmosphere models have been released in the recent years like the *WM-basic* models (Pauldrach et al. (1986)), the CMFGEN models (Hillier & Miller 1998) and the Potsdam Wolf-Rayet (PoWR) models (Gräfener et al. 2002; Hamann & Gräfener 2003, 2004; Sander et al. 2012; Hamann et al. 2006; Hainich et al. 2014). The POWR data base now provides very high quality models for the WR stars. But for the O, B stars with normal surface chemical composition, there is no well organized library. So, we decided to generate this kind of models. This chapter

thus is dedicated mainly to how we generate the library with WM-basic. Before describing the procedure of computing the models in section 4.3, we first give a short introduction to the stellar wind in section 4.2.

4.2 Stellar wind

Stars can lose some amount of the mass through the stellar wind, which can affect their evolution if the mass loss is substantial. For stars like the Sun or with lower masses, the stellar wind is driven by the hot corona induced gas pressure. For red giants, they possess slow but dense stellar wind, which is thought to be impelled by the magnetohydrodynamic waves. For the AGB stars, the wind is operated by the deep-seated stellar pulsation and the radiation on the dust generated during the pulsation. In analogy to the waves on the sea, the stellar material is pushed away from the star gradually by the successive pulsations. For hot stars (both massive stars and the central stars of planetary nebulae), the wind is driven by the radiative line-scattering. Finally, some massive stars, such as LBVs and RSGs, are found in giant eruptions with mass loss rates as large as $\sim 10^{-3} - 10^{-5} M_{\odot}/yr$, which are thought to be the continuum radiation-driven. For a review, the reader can refer to Owocki (2013).

The main contributors to the wind acceleration are the abundant scattering lines from ionic ground states of C, N, O, etc., and low-lying meta-stable levels of Iron group elements, with respect to the H and He, which have far less lines. Then the acceleration is shared with main mass content, i.e., H and He, through the Coulomb coupling in dense winds (Puls et al. 2008). However, in less dense winds, the Coulomb coupling is not so efficient that smaller mass-loss rates but larger terminal velocities are expected.

Baisc equations for stellar wind

To model the stellar wind, some assumptions are made. Firstly, the wind is stationary and spherically symmetric. Secondly, the wind is homogeneous. Recently, people have found evidence of clumping (and porosity) in the stellar wind, so that these assumptions are not strictly general.

The first equation comes from mass conservation:

$$\dot{M} = 4\pi r^2 \rho(r) = \text{constant}. \tag{4.1}$$

The second equation is from the momentum equation:

$$\frac{dv}{dt} = v\frac{dv}{dr} = -\frac{GM}{r^2} - \frac{dp}{dr}\frac{1}{\rho} + g_{\text{rad}}. \tag{4.2}$$

g_{rad} describes the radiative acceleration, including both the continuum and line driven contributions. In the deep layer of stellar interior, (gas) pressure is the dominant term counteracts the gravitational force that the fluid is still in hydrostatic equilibrium ($\frac{dv}{dt} = 0$), and electron scattering is the main contributor to the radiative acceleration term in the fully ionized plasma. Outwards, the contribution from the radiative acceleration increases, and the ionization stages of the ions are becoming lower. Thus the line driven contribution becomes more and more dominant. Then at a certain point, where $\frac{dv}{dt} > 0$, the wind is initiated. To solve this equation, we need to know the relation between p and ρ. In the stellar atmosphere, the thermal-dynamical processes are always close to adiabatic (because the timescales are small for thermal exchange with the surrounding environment of the bubbles). However, isothermal equation of state is assumed, $p = v_s^2\rho$, where $v_s = \sqrt{kT/\mu}$ is the isothermal speed of sound. Combined with the equation (4.1), equation (4.2) can be written as:

$$(1 - \frac{v_s^2}{v^2})v\frac{dv}{dr} = \frac{2v_s^2}{r} - \frac{dv_s^2}{dr} - \frac{GM}{r^2} + g_{\text{rad}}. \tag{4.3}$$

The main difficulty for solving this equation is the g_{rad} term. Let's consider the Thomson scattering. In one second, the photons can travel a length of c and the total energy emission is L. The scattered energy is $\kappa\rho Lc$ (κ is the opacity per unit mass of material $\kappa = \frac{n\sigma}{\rho}$, where σ is the cross-section. Since $n\sigma 4\pi r^2 c$ is the total area for the scattering, $\frac{n\sigma 4\pi r^2 c}{4\pi r^2} = n\sigma c = \kappa\rho c$ is the probability or portion of the total flux/luminosity scattered), and the corresponding momentum is $\kappa\rho Lc/c = \kappa\rho L$ (the angle average of line scattering for an scattered photon is $h\nu/c$, the same as an pure absorbed photon). The swept mass is $4\pi r^2 c\rho$. Suppose that the momentum is absorbed in the material, thus $g_{\text{Th}} = \frac{\kappa\rho L}{4\pi r^2 c\rho} =$

$\frac{\kappa L}{4\pi r^2 c}$. As the gravity acceleration is $g = \frac{GM}{r^2}$, we can define the Eddington ratio as

$$\Gamma = \frac{g_{\rm Th}}{g} = \frac{\kappa L}{4\pi c G M}. \tag{4.4}$$

In the case of Thomson scattering of electrons, the Thomson opacity is $\kappa_{\rm Th} = \sigma_{\rm Th} n_e/\rho$, where σ_e is the electron Thomson scattering cross-section and n_e is the electron density. $n_e = N_e \frac{\rho}{m_{\rm H}}$, where N_e is the free electron number per $m_{\rm H}$ mass and depends on the metallicity as well as the ionization state of the gas. Assuming a fully ionized gas mainly composed of Hydrogen and Helium, $N_e \simeq \frac{X * m_H * 1}{m_H} + \frac{Y * m_H * 2}{4 M_H} \simeq \frac{1+X}{2}$. Consequently, $\kappa_{\rm Th} = -\frac{(1+X)\sigma_e}{2 m_H} \simeq 0.02(1+X)\mathrm{m^2 kg^{-1}}$, and the Eddington ratio is:

$$\Gamma_e = 0.02(1+X)\mathrm{m^2 kg^{-1}} \frac{L}{4\pi c G M} = 10^{-4.813}(1+X)\left(\frac{L}{L_\odot}\right)\left(\frac{M}{M_\odot}\right)^{-1}. \tag{4.5}$$

However, for massive stars, the line scattering is much stronger than the electron scattering due to the resonant nature of bound-bound transitions. What's more, because of the Doppler effect, for a specific transition, the photons can interact with the medium across the stellar radii over a broad frequency range. For the line acceleration, a popular practise is the Sobolev approximation.

Sobolev approximation

In this section we consider a single line scattering. In principle, all the photons with frequency (in the observation frame) from ν to $(1 + \frac{v_\infty}{c})\nu$ have the probability to be scattered due to the line scattering of ν (in the co-moving frame of the wind). That is to say, the line formation in the stellar wind is subject to the whole atmosphere. The complication arises when we have to consider the finite width due to the thermal collision broadening. Thus at every atmospheric depth, we have to take into account the line profile to calculate the line acceleration. However, if the line profile can be approximated with a δ function, the calculation can be simplified. Therefore, at every depth the line acceleration can be computed locally. This localization method is called the Sobolev theory (Sobolev 1960). In this approximation, the frequency interval subject to scattering is $\delta\nu = \nu \frac{v_{\rm th}}{c}$, where $v_{\rm th}$ is the thermal velocity. This velocity interval corresponds to a velocity interval

of $\delta v = v_{\rm th}$ and a radial length of $l_s = v_{\rm th}/\dfrac{dv}{dr}$. In stellar wind, the line scattering is restricted in a region of width l_s at a certain laboratory frequency. Outside of this width, the line frequency shifts to another laboratory frequency. The scattered momentum is $p = \dfrac{L_\nu \delta\nu(1-e^{-\tau})}{c}$, and the line acceleration is $p/m = p/(4\pi r^2 \rho l_s)$, or

$$g_{\rm rad,line} = \frac{L_\nu \nu}{4\pi r^2 c^2 \rho}(\frac{dv}{dr})(1-e^{-\tau}), \tag{4.6}$$

where, $\tau = \kappa_\nu \rho l_s = \kappa_\nu \rho v_{\rm th}/(\dfrac{dv}{dr})$. For $\tau < 1$, $g_{\rm rad,line}$ is independent of the velocity field, while for $\tau > 1$, it does depend on the velocity gradient.

Suppose a wind with only one resonant line. Photons of frequency blueward of this line can travel freely until they reach a radial position, where the photons red-shifts into the interaction range of the line in the rest-frame of the wind material. After a length of l_s, the photons can travel freely again. Because photons of different frequencies are scattered at different radial positions in the wind locally, the optical depth, in the case of static material, is usually evaluated by the integration over a non-local distance. While under the Sobolev approximation, it is only evaluated with the length of l_s, as $\tau = \kappa_\nu \rho l_s = \kappa_\nu \rho v_{\rm th}/(\dfrac{dv}{dr})$.

The Sobolev approximation is only valid in the supersonic part of the wind.

CAK theory

In the above, we have worked out the acceleration for a single line. Now we have to sum over all the lines, which is the CAK theory (Castor et al. 1975). We can define the line strength as $t = \dfrac{\kappa_{\rm line}}{\kappa_{\rm Th}}$. In this theory, the strength distribution is modelled by a power law of t with an index of α, so that the number of lines at ν and t is

$$dN(\nu, t) = -K f_\nu(\nu) t^{\alpha-2} d\nu dt. \tag{4.7}$$

Thus, by integrating all the lines with this line distribution, the total line acceleration can be calculated. The total line acceleration can be expressed with $g_{\rm Th}$ as $g_{\rm rad,line} = M(t) g_{\rm Th}$, where $M(t)$ is the so-called force-multiplier. The force-multiplier $M(t)$ is characterized with three parameters: κ, α and δ. κ is connected to the number of stronger lines, α is related to the slope of the line-strength distributions, and δ is a factor accounts for the

ionization effects. For typical O-stars, δ is of the order of 0.1. δ is not a free parameter. α is near 2/3.

By using the continuity and momentum equations, the CAK mass loss rate (maximal) can be derived:

$$\dot{m}_{CAK} = \frac{L}{c^2}\frac{\alpha}{1-\alpha}\left[\frac{\bar{Q}\Gamma_e}{1-\Gamma}\right]^{(1-\alpha)/\alpha}. \tag{4.8}$$

The velocity law is

$$v(r) = v_\infty(1 - R/r)^\beta, \tag{4.9}$$

with $\beta = 0.5$, and the terminal velocity is

$$v_\infty = v_{esc}\sqrt{\alpha(1-\Gamma_e)/(1-\alpha)}. \tag{4.10}$$

The factor $\bar{Q}$ is the normalization related to the line strength distribution. The equation (4.9) is called 'β'-velocity law, with different βs for different type of stars. For example, $\beta = 0.8$ for O-stars, and 2 for BA-supergiants.

From the expressions for $\dot{m}_{CAK}$ and v_∞, a scaling relation "wind momentum-luminosity" is derived:

$$\dot{m}_{CAK}v_\infty\sqrt{R_*} \sim L^{1/\alpha}\bar{Q}^{1-\alpha/\alpha}. \tag{4.11}$$

The success of the CAK theory is ratified by the comparison with the observation. $\bar{Q}$ provides the dependence of this relation with the metallicity.

However, in the CAK theory, the lines are approximated independently so that the contributions can be added directly. For O, B stars, the thin wind enables this assumption. But for WR stars, the wind is thick, so the line overlapping and multiple scattering have to be taken into account.

Monte Carlo simulations

The CAK theory provides a very simple and analytical approach to the stellar wind. However, it only applies on a predefined velocity law and the wind parameters. Furthermore it can not be used when clumping is present. To model the wind in a dynamical way or the inhomogeneity in the wind, the Monte Carlo method is adopted (e.g., Noebauer & Sim 2015).

Stellar wind diagnostics

Here I summarize some techniques for the observational constraints on the stellar wind. A lot of the descriptions come from Owocki (2013).

The driving force of the hot (and cool) massive stars comes from the interaction of the radiation with the stellar atmosphere materials. The processes include (1) electron scattering; (2) free-free absorption and emission; (3) bound-free absorption and free-bound emission by atoms or molecules; (4) bound-bound scattering, absorption and emission of atoms and molecules; (5) scattering, absorption, and emission of dust grains. The strengths of (1), (3) and (4) are density dependent, while those of (2) and (5) are density-squared dependent. If there is inhomogeneous in the stellar wind, then the different observational signatures due to the density-squared mechanism will respond differently by a clumping factor $C_f \equiv \sqrt{\langle\rho^2\rangle}/\langle\rho\rangle$.

In the stellar wind, the optical depth of line absorption can be given with the Sobolev approximation. Compared to the wind terminal velocity v_∞, the thermal velocity $v_{\rm th}$ is very small. The Sobolev approximation thus assumes $v_{\rm th} \to 0$. Then the opacity over this line can be modelled as a delta function. The optical depth can then be integrated analytically with assumed wind velocity law.

Firstly, the most important feature for constraining the wind properties is the P-Cygni profiles. It is arisen from the line scattering in the stellar wind. The UV lines from P^{+4} (PV) is of particular use. It is because P^{+4} is always the dominant ionization stage so that the correction for the ionization state is at minimum. Also, the abundance of phosphorus is quite low, thus the lines are generally not saturated. A very nice illustration for the formation of the P-Cygni can be found in the figure 15-4 of Owocki (2013). By fitting the predicted P-Cygni profile, the terminal velocity (the width of the absorption trough) and the mass loss rate can be derived. This scattering nature of the P-Cygni profiles lead them to be immune to the wind clumping. The second diagnostic feature is the broad emissions from very dense winds. Examples are the H_α and CIII lines. However, these lines suffer from the uncertainties in the clumping, due to the density-squared dependence. The third method uses the continuum emission in radio and infrared bands. The continuum arises from the free-free emission, so it is also affected by the clumping. The above three methods can be combined to give more robust results.

4.3 O, B star atmosphere models computed with WM-basic

For temperatures typical of O and B stars (60000 K> T_{eff} >19000 K) we have generated a new library of models using the public code *WM-basic* (Pauldrach et al. 1986). This allows us to take into account both the effects of extended winds and those of non-LTE, since both effects may significantly affect the emergent spectra of hot stars. We have generated new sets of stellar spectral libraries covering as much as possible the space of parameters of our new evolutionary tracks of massive stars, i.e., effective temperature, gravity, metallicity and mass-loss rate. The temperature grid ranges from $\log T_{eff} = 4.3$ to 5.0 in steps of $\Delta \log T_{eff} = 0.025$ dex. At each temperature, we adopt a step in gravity of $\Delta \log g = 0.5$ dex, with upper and the lower boundaries that depend on the T_{eff}. Indeed, the highest gravity is determined by the fact that the line-driven radiation force cannot initiate the stellar wind, while the lowest value corresponds to stability problems when the models approach the Eddington limit. At each grid point we consider three different values of the mass-loss rates, i.e., $\dot{M} = 10^{-7}$, 10^{-6}, and $10^{-5}\, M_{\odot}/yr$, encompassing typical values for O, B stars.

We note that, besides T_{eff}, $\log g$ and stellar radius (radius defined at a Rosseland optical depth of 2/3, $R_{*,2/3}$), there are additional input parameters in *WM-basic*: κ, α and δ, referring most specifically to the structure of the wind as shown by Castor et al. (1975). Thus, for any point in the (effective temperature, gravity) grid we suitably change the other stellar parameters (radius, luminosity and mass) as well as the wind parameters α and κ in order to obtain three consistent atmosphere models with the required values of mass-loss rates, i.e., $\dot{M} = 10^{-7}, 10^{-6}$, and $10^{-5} M_{\odot}/yr$. These models are used to derive the broad band colors and magnitudes for any given effective temperature, gravity and metallicity, easily interpolating for the different values of the mass-loss rates actually used in the tracks. Our new library consists of about 300 models for each metallicity. For example, for $z = 0.02$, we computed 105 models for $\dot{M} = 10^{-7}$, 98 for $\dot{M} = 10^{-6}$ and 86 for $\dot{M} = 10^{-5}$. The metal partition adopted in the new models is the same as used in Bressan et al. (2012), to say Caffau et al. (2011). As an example, we show in figure 4.1, the effects of changing the mass-loss rate at constant metallicity (upper panel) and those of changing the metallicity at constant mass-loss rate (lower panel), for models

with $\log T_{\rm eff} = 4.6$ and $\log g = 3.5$. In the upper panel, the black line refers to the model with $\dot{M} = 10^{-5} M_{\odot}\ yr^{-1}$, while the red one is for $\dot{M} = 10^{-7} M_{\odot}\ yr^{-1}$. We can see that the He II continuum is more absorbed in the model with higher mass-loss rate. We notice also that, as expected, some spectral features which appear in emission in the higher mass-loss rate model, turn into absorption in the model with a lower mass-loss rate.

In the lower panel, the black line refers to the same model as in the upper panel, while, the red one is now for a model at the same grid point but with $Z = 0.008$. This comparison shows that the effects of changing the metallicity on these hot spectra are less pronounced than those arising from the variation of the mass-loss rates.

4.4 Wolf-Rayet star models from PoWR

WR stars typically have wind densities one order of magnitude larger than those of massive O-type stars. Spectroscopically they are dominated by the presence of strong broad emission lines of Helium, Nitrogen, Carbon and Oxygen. They are subdivided into different sub-types, one with strong lines of Helium and Nitrogen (WN stars), another one with strong lines of Helium and Carbon (WC stars) and a third one with strong Oxygen lines (WO stars).

To reproduce their spectra we make use of the most recent library of WR models computed by the Potsdam group (PoWR) (Gräfener et al. 2002; Hamann & Gräfener 2003, 2004). They provide models with metallicities corresponding to those of WR stars in the Galaxy, the LMC and the SMC. The model grids are parameterized with $T_{\rm eff,\tau=20}$ (the effective temperature at radius where the Rosseland optical depth is 20), and the transformed radius R_t (because models with the same set of such parameters show the same emergent spectrum as discussed in Schmutz et al. (1992)). The transformed radius R_t is given by (Schmutz et al. 1992):

$$R_t = R^*_{\tau=20} \left(\frac{v_\infty}{2500\, km\, s^{-1}} \frac{10^{-4} M_{\odot} yr^{-1}}{\dot{M}} \right). \tag{4.12}$$

Since $R^*_{\tau=20}$ is nearly equivalent to the hydrostatic radius of the evolutionary tracks, this quantity combines stellar radius and mass-loss rate of the tracks with the terminal velocity. For the same reason $T_{\rm eff,\tau=20}$ corresponds to the effective temperature of our

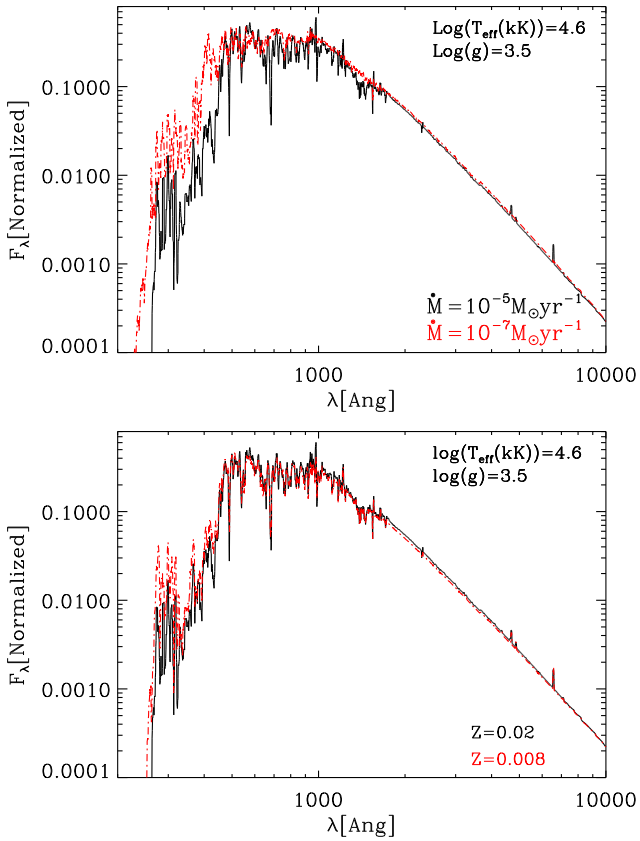

Figure 4.1: Upper panel: comparison of *WM-basic* spectra (smoothed) of different mass-loss rates. The effective temperature, gravity, radius and metallicity ($Z = 0.02$) are the same, but the black one is for $\dot{M} = 10^{-5} M_\odot\ yr^{-1}$ and red one is for $\dot{M} = 10^{-7} M_\odot\ yr^{-1}$. The ionizing photon (with wavelength smaller than 912 nm) number ratio ($N_{\rm Ionizing}(\dot{M} = 10^{-5} M_\odot\ yr^{-1})/N_{\rm Ionizing}(\dot{M} = 10^{-7} M_\odot\ yr^{-1})$ supposing the same luminosity) is 0.197. Lower panel: comparison of *WM-basic* spectra (smoothed) of different metallicities. The effective temperature, gravity, radius and mass-loss rate ($\dot{M} = 10^{-5} M_\odot\ yr^{-1}$) are the same, but the black one is for $Z = 0.02$ and red one is for $Z = 0.008$. The ionizing photon number ratio ($N_{\rm Ionizing}(Z = 0.02)/N_{\rm Ionizing}(Z = 0.008)$ supposing the same luminosity) is 0.994 (almost identical). All the spectra are normalized over the wavelength range from 0.84 to 1.44 μm.

hydrostatic models $T^*_{\rm eff}$. As shown in Hamann & Gräfener (2004), at large R_t (or thin winds), $T_{{\rm eff},\tau=20} \backsimeq T_{{\rm eff},\tau=2/3}$. (In the case of our *WM-basic* models, R_t are always $\gtrsim 1.5$, so there is no need to use R_t to match atmosphere models and theoretical tracks). As done in Schmutz et al. (1992), we match the WR atmospheres to the evolutionary tracks by interpolating $T^*_{\rm eff}$ and R_t.

An issue concerns the match between stellar models and stellar atmosphere models. While the observational classification is quite well defined (Crowther 2007; Crowther et al. 1998), it is more difficult to assign the WR subgroups along the evolutionary tracks. We use the following convention to identify them. WR stars are classified as WNL (late) when the surface Hydrogen mass fraction $X_{\rm H}$ is below a given threshold, $X_{\rm WNL}$. When $X_{\rm H} = 0$, they are classified as WNE (early) if $N(^{12}{\rm C}) < N(^{14}{\rm N})$ and as WC if $N(^{12}{\rm C}) \geq N(^{14}{\rm N})$. We finally assign the WO subtype when the condition $N(^{12}{\rm C}) + N(^{16}{\rm O}) > N(^{4}{\rm He})$ is fulfilled (Smith & Maeder 1991). The classification is based on the belief that difference classes are in different evolutionary stages. The WN stars show Nitrogen enrichment as a result of the Hydrogen burning, as we recall that the Nitrogen cycle is the slowest one in the CNO cycle. However, in WC/WO stars, the by-products of Helium burning has reached the surfaces, thus WC/WO stars are thought to be more evolved with respect to WN stars. We then match our type assignments with the models provided by PoWR, which adopts a fixed composition for any given subtype. For example, for the Galactic metallicity, in the PoWR library $X_{\rm WNL}$=0.5 and the different subtypes have the following surface compositions:

- WNL-H50 for $X_{\rm H}=X_{\rm WNL}$, $X_{\rm He}=0.48$, $X_{\rm C}=1{\rm E}{-}4$, $X_{\rm N}=0.015$, $X_{\rm O}=0$ and $X_{\rm Fe}=0.0014$;
- WNL for $X_{\rm H}=0.2$, $X_{\rm He}=0.78$, $X_{\rm C}=1{\rm E}{-}4$, $X_{\rm N}=0.015$, $X_{\rm O}=0$ and $X_{\rm Fe}=0.0014$;
- WNE for $X_{\rm H}=0$, $X_{\rm He}=0.98$, $X_{\rm C}=1{\rm E}{-}4$, $X_{\rm N}=0.015$, $X_{\rm O}=0$ and $X_{\rm Fe}=0.0014$;
- WC for $X_{\rm H}=0$, $X_{\rm He}=0.55$, $X_{\rm C}=0.4$, $X_{\rm N}=0$, $X_{\rm O}=0.05$ and $X_{\rm Fe}=0.0016$.

In the above, $X_{\rm Fe}$ represents the mass fraction Iron-group elements from Sc to Ni. Their relative number ratios are given in the table 2 of Gräfener et al. (2002). For the LMC, the surface Hydrogen threshold is $X_{\rm WNL}$=0.4, while for the SMC they provide models with both $X_{\rm WNL}$=0.6 (WNL-H60 models) and $X_{\rm WNL}$=0.4 (WNL-H40 models). Note that PoWR does not yet provide spectral models for WO stars, which, however, are quite rare objects especially at lower metallicities.

Recently, the PoWR group updated their database with very high quality SEDs for the WR models. The SEDs are available at http://www.astro.physik.uni-potsdam.de/~htodt/powr-sed/. We will discuss the differences between the previous and new PoWR model sets later.

Finally, we should keep in mind that, in reality, there should be a continuous evolution in the physical and chemical properties among O, B stars and different types of WRs. We will address this issue again when we transform the evolutionary tracks to observational magnitudes with the atmosphere models.

4.5 Color-magnitude diagrams of stellar tracks

Besides evolutionary tracks, we provide new tables of bolometric corrections that allow for the conversion from the theoretical HR to the observed colour-magnitude diagrams. For this purpose, we assemble existing atmosphere libraries, i.e., ATLAS9, PoWR, Phoenix and new atmosphere models calculated on purpose with the *WM-basic* code. We merge these different libraries with interpolation on a global metallicity scale, providing quite homogeneous tables of bolometric corrections, at several metallicities. We convert from effective temperature, gravity and luminosity to magnitudes and colours using theoretical atmosphere models.

The ranges of effective temperatures encompassed by different spectral libraries are marked by vertical lines in the HR diagrams shown in figure 4.2, for $Z = 0.02$ (left panel) and $Z = 0.008$ (right panel), respectively. Overplotted are selected stellar evolutionary tracks from $M_{\rm ini}$=20 $M_\odot$ to $M_{\rm ini}$=350 $M_\odot$. The combined atmosphere models, that share the same global metallicity of the corresponding evolutionary tracks as shown in the HR diagram, provide a very good coverage in terms of effective temperatures and gravities. They allow for an optimal calculation of bolometric correction (BC_λ) tables that are used to convert from theoretical to observational diagrams. The details of this process are thoroughly described in Girardi et al. (2002b) and Chen et al. (2014a), and are not repeated here. While for the evolutionary tracks we only consider the photospheric magnitudes, the corresponding isochrones also account for the effect of possible circumstellar dusty envelopes following the dust calculation recipes described in Marigo et al. (2008) and Nanni et al. (2013, 2014).

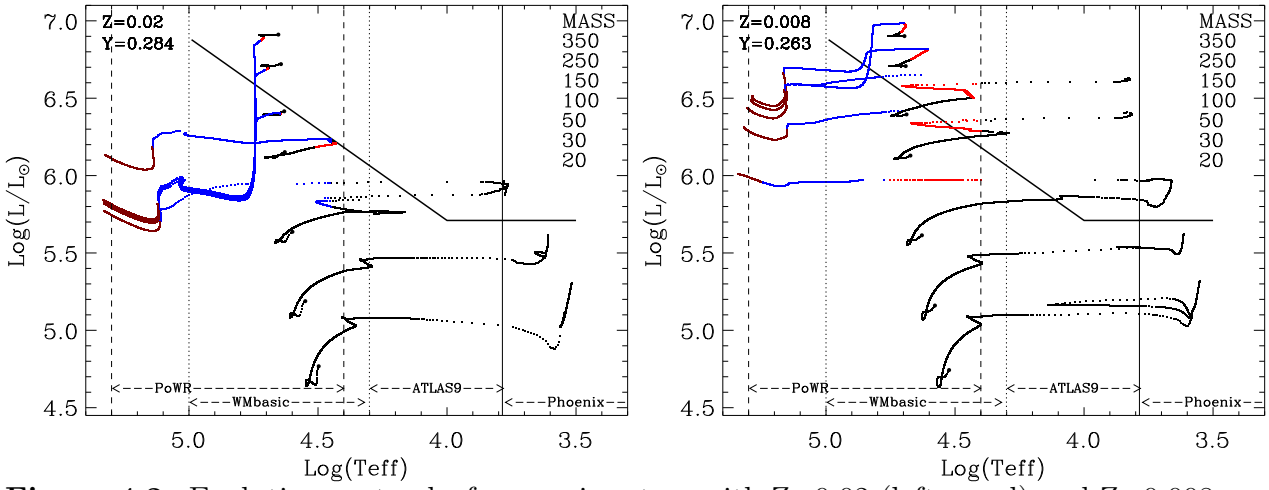

Figure 4.2: Evolutionary tracks for massive stars with Z=0.02 (left panel) and Z=0.008 (right panel). Different colours represent different evolutionary stages: black for stages precedent of WR phases, red for models using PoWR WNL-H50 ($Z = 0.02$) or WNL-H40 ($Z = 0.008$), blue for WN models, and brown for WC models. The overplotted vertical lines delimit the coverage of different atmosphere models as indicated in the plots. The Humphreys-Davidson limit is also drawn as in figure 3.1.

An example of the colour-magnitude diagrams of the tracks of $M_{\rm ini}$=100$M_\odot$ and $M_{\rm ini}$=50$M_\odot$ is shown in figure 4.3, for Z=0.02 (left panels) and Z=0.008 (right panels), respectively. In the figure, we highlight the different evolutionary phases with different colours and line styles. Black dotted lines indicate the evolution precedent of the WR stages, while the red solid lines are used to indicate the transition phase from the LBV phase to the late WR stars (WNL-H50 for $Z = 0.02$ or WNL-H40 for $Z = 0.008$ in the PoWR notation). The blue dash-dotted lines are used for the other WN stages and the brown dashed lines are for the final WC/WO stages.

As can be seen in the figure, the optical colours show some evident jumps when the star type changes from WN to WC. This is likely to be caused by the appearance of different strong emission lines in different sub-types. This can be seen from figure 4.4, where we compare the spectra of one WC star (black solid line) and one WN (red dashed line) star with the same effective temperature. We show the optical region sampled by the broadband filters F438W, F555W, and F814W of the HST/WFC3 system. Both spectra show a strong emission HeII(4700Å) line, falling within the F555W passband and touching the border of the F438W passband. The differences between the WN and the WC spectral types are mainly on the contribution of the strong CIV(5800Å) line within the F555W passband, in the latter type. Thus, the flux in the F555W passband

is heavily enhanced in the case of the WC star with respect to that of the WN star, and correspondingly the sudden transition from the WN to the WC types is accompanied by a jump in the F438W-F555W and F555W-F814W colours. It is important to stress that the CIV(5800Å) doublet is very sensitive to the adopted atmosphere parameters which somehow challenges its predictability (private communication with Helge Todt, Wolf-Rainer Hamann and Götz Gräfener). Furthermore, we have to note that the transition between WN and WC spectral types is smoother in the tracks than in the spectra, because the latter is computed only at discrete values of the elemental abundances, and this could enhance the effect, at least in terms of evolutionary speed.

Using the evolutionary tracks we compute new isochrones of young stellar populations, with the same procedure already described in Bressan et al. (2012). A few examples are shown in the theoretical HR diagram of figure 4.5, from very young to very old ages and for Z=0.02 (left panel) and Z=0.008 (right panel), respectively. By means of the new bolometric correction tables, we convert theoretical isochrones into observational magnitudes/colours, in the same way used for the evolutionary tracks. In figure 4.6 we show the colour-magnitude diagrams of isochrones at very young ages, 1 Myr and 2.5 Myr, and for Z=0.02 and Z=0.008. The colour codings are the same as in figure 4.3, but for the pre-main sequence which is drawn in light gray.

As we have mentioned just above that PoWR provides both the previous low resolution models, which were used in our paper Chen et al. (2015), and recent high resolution models. We compare the resulting evolutionary tracks and isochrones on the CMD with the two different resolution SEDs. The tracks and isochrones with the previous low resolution SEDs are shown in figures 4.3 and 4.6, respectively, with gray lines. Though the general trends are the same, there are some differences between the old low resolution and the new high resolution SED results. The difference in the colors is basically less than 0.1 mag, while in the magnitude it is less than 0.2 mag.

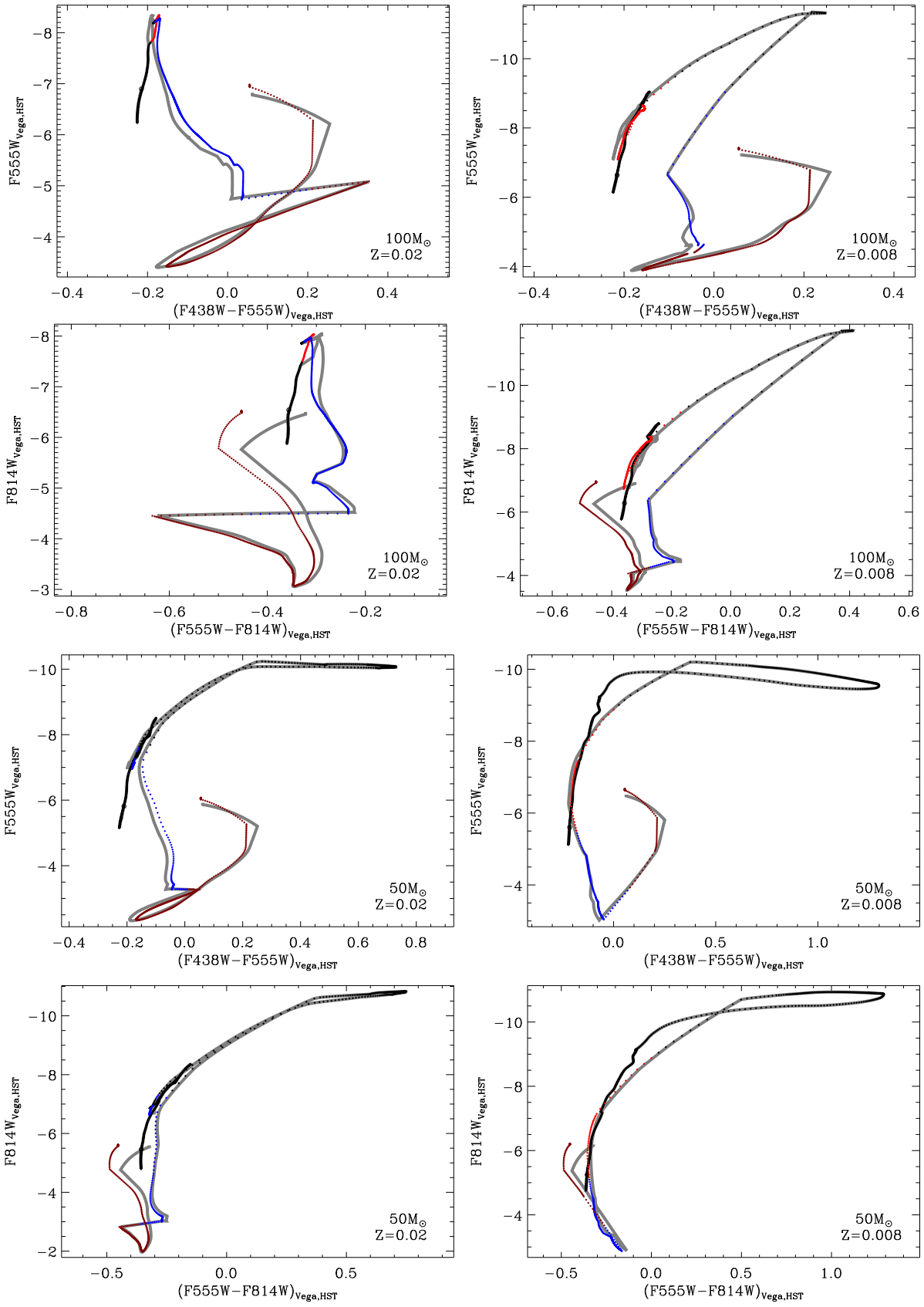

Figure 4.3: We use new stellar spectral libraries to transform the evolutionary tracks into observable colors. Different colours are used for PoWR WC (brown), WN (blue) and WNL-H50(40) (red) models. For the gray track we use previous low resolution PoWR models.

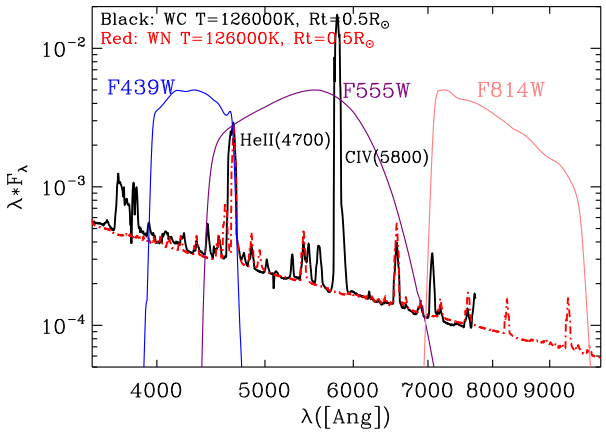

Figure 4.4: Comparison of PoWR WC (black) and WN (red) models with the same effective temperature T_{eff} = 120000 K and metallicity Z=0.02. Also shown are the transmission curves of three HST/WFC3 filters (F438W, F555W and F814W). Notice the two strong emission lines HeII(4700) and CIV(5800) can greatly influence the magnitude/colors in related passbands.

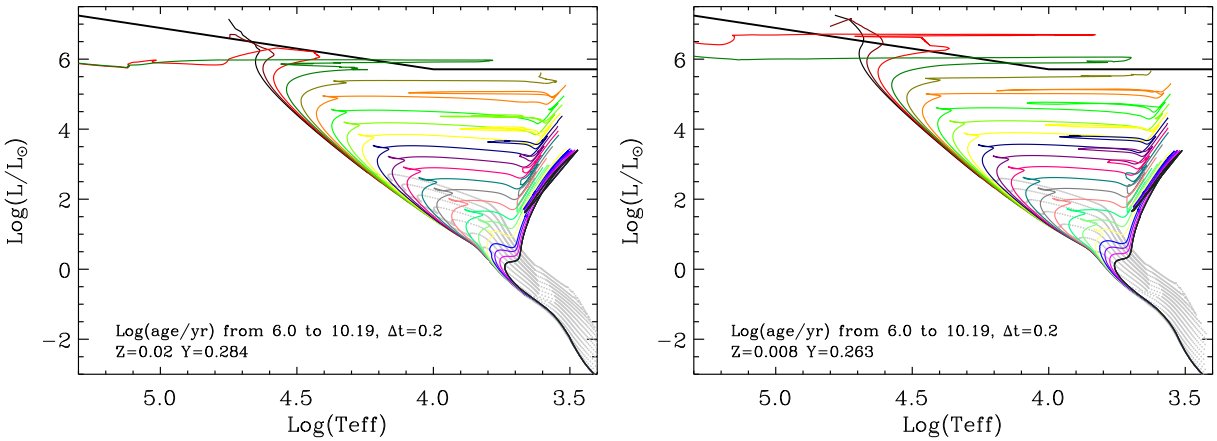

Figure 4.5: Isochrones of different ages, as indicated by the labels, are shown for Z=0.02 (left panel) and Z=0.008 (right panel). Note that at young ages intermediate and low mass stars are still on the pre-main sequence (grey dots). The Humphreys-Davidson limit is also drawn as in figure 3.1.

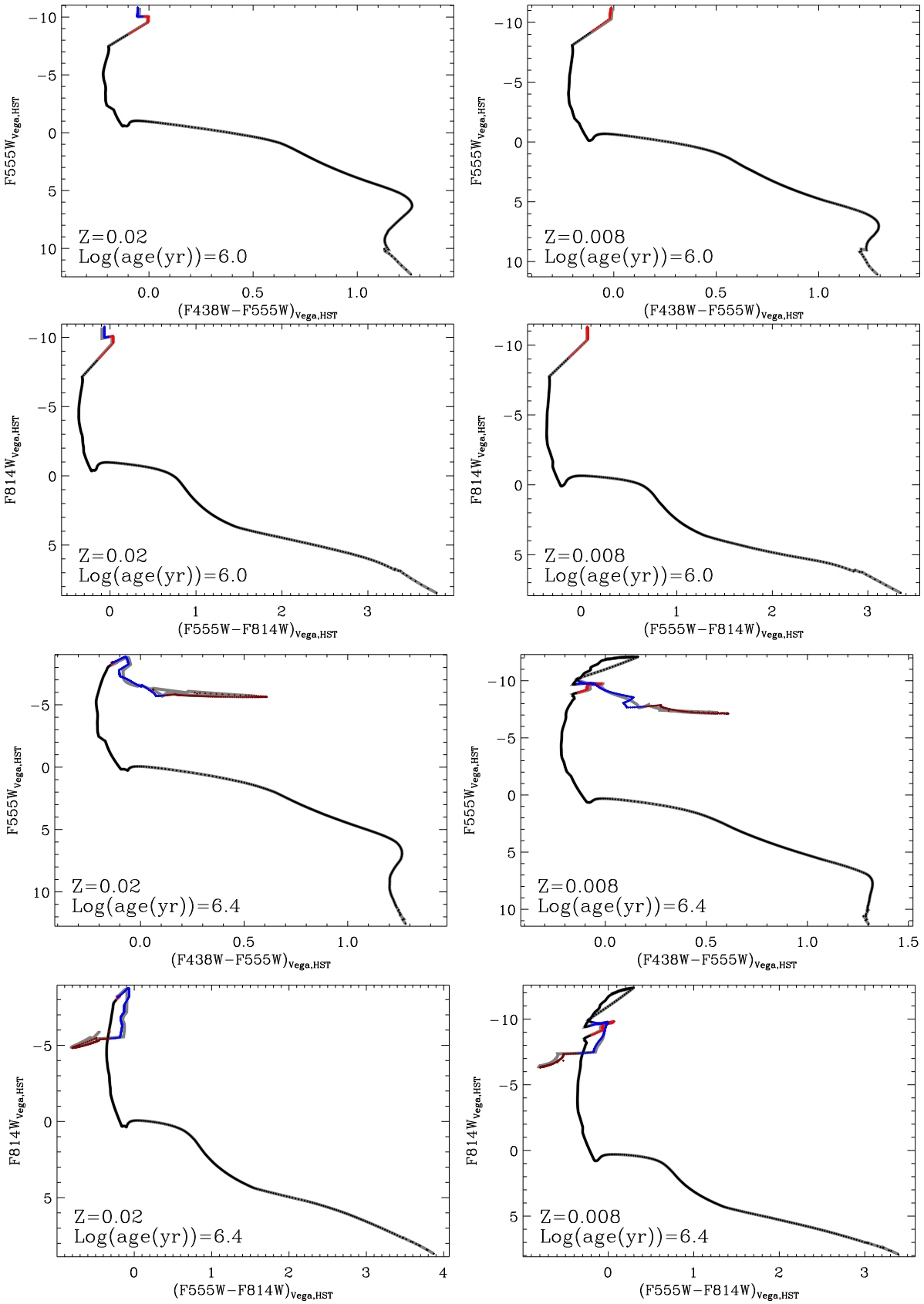

Figure 4.6: We use new stellar spectral libraries to transform the isochrones into observable colors. The indications are the same as in figure 4.3

Chapter 5

Summary of stellar atmosphere models and Isochrones

In this chapter, I summarize the atmosphere models used in my Ph.D. projects.

5.1 Atmosphere models, bolometric tables & empirical stellar spectral libraries

The atmosphere models provide emergent spectra so that the theoretical parameters (luminosity, gravity and effective temperature) of stellar evolutionary tracks can be converted into colors/magnitudes. Then the colors can be compared with observations on the colour-magnitude diagram. The atmosphere models can also provide the boundary conditions for the stellar interior models as discussed in section 1.3. In the following, I will present some popular stellar atmosphere models. A special attention is drawn for the models I generated for the hot massive stars. In the last part, I will introduce some empirical stellar spectral libraries, like IRTF, MILES, etc.

5.2 ATLAS

The core of our library consists of the plane parallel ATLAS9 models (Kurucz 1995). These LTE models are well suited to describe the atmospheres of intermediate and low mass stars of spectral types between A and K. The most recent ATLAS9 models are

those computed by Castelli & Kurucz (2004). ATLAS9 models are based on the Solar abundances by Grevesse & Sauval (1998) and make use of an improved set of molecular lines including TiO, H_2O, HI-Hi and $HI - H^+$. The model grids are computed for T_{eff} from 3500 K to 50000 K, $\log g$ from 0.0 dex to 5.0 dex and [M/H]=+0.5, +0.2, 0.0, -0.5, -1.0, -1.5, -2.0, -2.5, -3.5, -4 and -5.5. We limit the use of ATLAS9 models to the temperature range of 19000 K> T_{eff} >6000 K. At higher temperatures, in general, we need to consider models with mass-loss while at lower temperatures the Phoenix models are more appropriate.

Recently, there is also a spherical version of the ATLAS12 models at `http://www.astro.utoronto.ca/~lester/programs.html`, as described in Lester & Neilson (2008).

5.3 Phoenix

As reviewed by Allard et al. (1997b), the atmospheres of cool stars are dominated by the formation of molecules and eventually at very low temperatures by dust condensation that can affect the spectral shape significantly. A suitable set of 1D, static spherical atmosphere spectral models accounting for the above effects has been developed in the recent years and is continuously maintained by the Phoenix group (Allard & Homeier 2012). We adopt such models for temperatures $T_{eff} \leq 6000$ K. Among the different suites of libraries, we use the BT-Settl models which contain the most updated and complete stellar parameter grid and are well tested against observations (Allard & Homeier 2012). The models are provided for 50000 K > T_{eff} > 2600 K, $0.5 < \log g < 6$, and metallicities $0.000003 \lesssim Z \lesssim 0.04$. These tables for cool stars have already been used in Chen et al. (2014a), in the context of low and very low mass stars.

A comparison between ATLAS, Phoenix and MARCS are made in Plez (2011) and reference therein. They find that there is no large difference in the atmosphere structure, but there are some discrepancies in the spectra, especially in the blue-UV part.

According to Dotter et al. (2008), Phoenix uses an ideal EOS but contains a large number of elements and molecules, while FreeEOS accounts for several non-ideal effects but includes fewer elements and only molecules that involve H and He.

Phoenix models employ the standard mixing length theory for the convection with mixing length of $\alpha_{ML} = 2.0$ (Dotter et al. 2008).

5.4 WM-basic

In section 4.3, we described how we computed a grid of atmosphere models for O,B stars with *WM-basic* (Pauldrach et al. 1986). These models cover the temperature range of 60000 K> T_{eff} >19000 K at a step of $\Delta \log T_{eff} = 0.025$ dex. At each temperature, the upper limit of gravity is determined by the fact that the line driven radiation force cannot initiate the stellar wind, while the lower limit value corresponds to stability problems when the models approach the Eddington limit. The gravity grids are in a step of $\Delta \log g = 0.5$ dex. At every effective temperature and gravity models are computed with three mass loss rates: $\dot{M} = 10^{-7}$, 10^{-6}, and $10^{-5}\, M_{\odot}/yr$. The models are using the same metallicities as in Bressan et al. (2012). At each metallicity, we generate about 300 models.

5.5 PoWR

In section 4.4, we have discussed the PoWR models in detail. Here we just give a short summary. The Potsdam group (PoWR) provides very high quality atmosphere models for WR stars in three metallicty environments: Galaxy, LMC, and SMC. At every metallicity, models are available for different WR subtypes: WNL-H50/H40/H60, WNL, WNE, and WC. In figure 5.1, I show the some examples of PoWR SEDs of effective temperautre 10^5 K and $\log(R_t) = 0.5$. The different SEDs represent different types of WR stars at the Galactic environment.

5.6 Synthetic bolometric correction tables

A concern on the libraries described above is that the different sets (*WM-basic*, PoWR, ATLAS9 and BT-Settl) are calculated with different metallicities and different partitions of heavy elements. In order to obtain homogeneous spectral libraries, at least as far as the metallicity is concerned, we first calculate the global metallicity from the detailed abundance values provided by each group. We note, for example, that the BT-Settl models adopt a Solar partition (Asplund et al. 2009) different from the one adopted in PARSEC (Caffau et al. 2011) and that, at low metallicities, their partitions are α enhanced. On the contrary, for our *WM-basic* models, we use the same metallicities as in PARSEC. We then interpolate each set of spectra on the global metallicity grid defined by the PARSEC

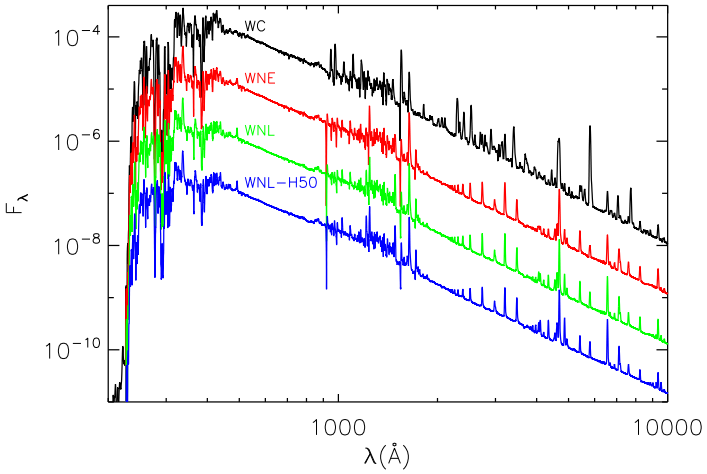

Figure 5.1: PoWR SEDs with $log\,\mathrm{T_{eff}} = 5$ and $\log(R_t) = 0.5$, at the Galactic environment. The orginal SEDs are all normalized to the Solar luminosity (flux at 10 pc). Here for clear illustration, I doward shift the SEDs of WNE, WNL, and WNL-H50 by 10, 100, and 1000 times respectively.

models. Since PoWR models are provided only for three typical metallicities, i.e., our Galaxy, the LMC and the SMC, we use Galaxy models for $Z \geqslant 0.01$, LMC models for $0.01 > Z > 0.006$ and SMC models for $Z \leqslant 0.006$. In figure 5.2, I show the coverage of the models with $Z = 0.02$ (or Galactic metallicity for PoWR models).

Filter convolution

From the assembled SED, we can construct the bolometric table, which then can be used for photometric studies. Depending on the photometric system used, for energy counting system (early days devices), the magnitude in a certain band i is:

$$\begin{aligned} m_i &= -2.5\log\frac{\int_{\lambda_1}^{\lambda_2} f_\lambda R_\lambda(i)d\lambda}{\int_{\lambda_1}^{\lambda_2} f_\lambda^0 R_\lambda(i)d\lambda} + m_i^0 \\ &= -2.5\log\frac{\int_{\nu_1}^{\nu_2} f_\nu R_\nu(i)d\nu}{\int_{\nu_1}^{\nu_2} f_\nu^0 R_\nu(i)d\nu} + m_i^0 \end{aligned} \tag{5.1}$$

where $R_\lambda(i)$ is the response function of the photometric system, and f_λ is the SED of the model while f_λ^0 is the reference spectrum. m_i^0 is the photometric zeropoint. In Vega system, Vega will have magnitude equal to 0 at all wavelengths, to say the m_i^0 is always zero. However, because of uncertainties in the calibration of the absolute flux of Vega, a small shift in the zeropoint can be applied over time. For example, a magnitude of 0.03 can be corrected for the old Buser, Johnson, and Bessell photometric filter systems. For Vega sys-

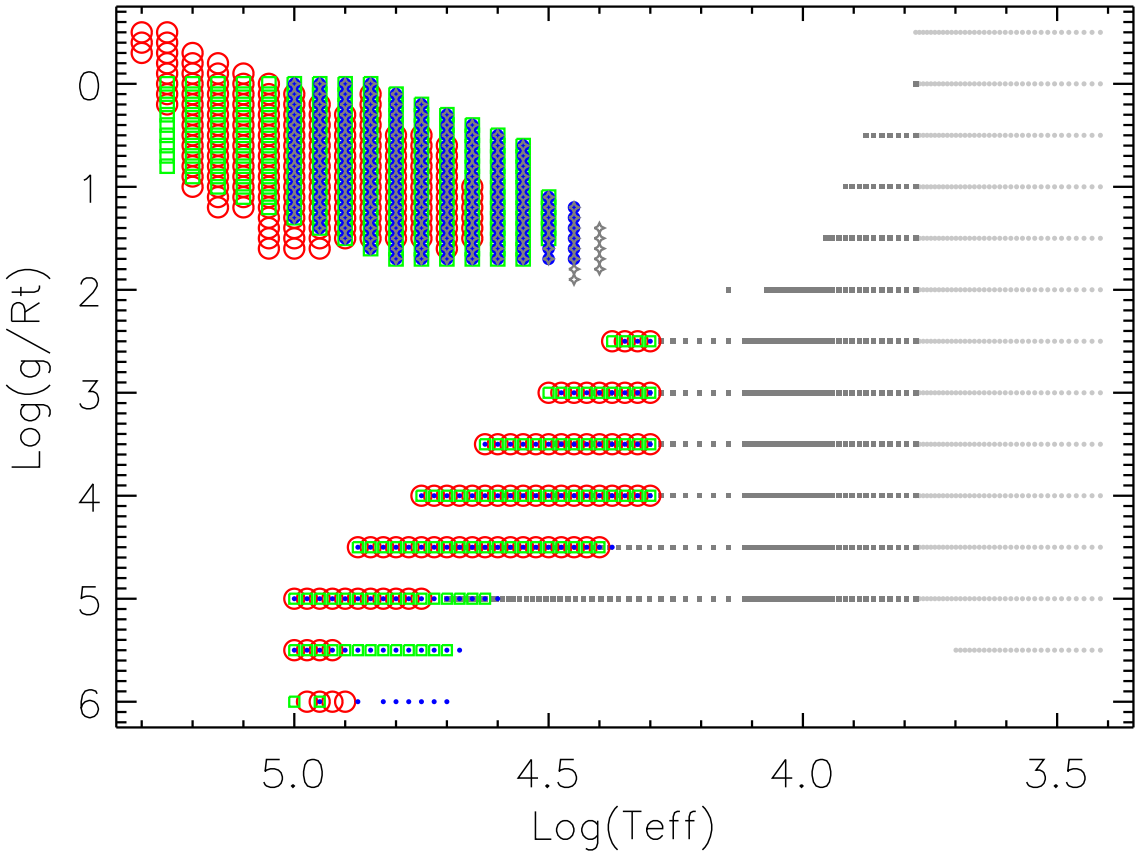

Figure 5.2: The coverage of Z= 0.02 atmosphere models. Below 6000 K, the light gray points are the Phoenix/BT-Settl models. Above 6000 K, the gray squares are the ATLAS9 models. The WM-basic models with $\dot{M} = 10^{-5}, 10^{-6}$ and $10^{-7} M_{\odot}\ yr^{-1}$ are shown with red open circles, green open squares and blue solid dots, respectively. The PoWR models are for Galactic environment, and the vertical axis is the transformed radius R_t. The WC, WNE, WNL, and WNL-H50 models are shown with red open circles, green open squares, blue solid dots and gray stars, respectively.

tem, we take the spectrum from ftp://ftp.stsci.edu/cdbs/current_calspec/alpha_lyr_stis_006.fits, as described in Bohlin (2007). For AB, it is defined that an object with a constant flux distribution $F_\nu = 3.63 \times 10^{-20}$erg cm^{-2}s^{-1}Hz^{-1} at all wavelengths will have $mag_{AB} = 0$ at all bands. In the case of ST magnitude system, an object with $F_\lambda = 3.63 \times 10^{-9}$erg cm^{-2}s^{-1}Ang^{-1} at all wavelengths will have $mag_{ST} = 0$. Since in both Vega and AB systems, $m_i^0 = 0$, so (5.1) can be written as:

$$\begin{aligned} m_i &= -2.5 \log \frac{\int_{\lambda_1}^{\lambda_2} f_\lambda R_\lambda(i) d\lambda}{\int_{\lambda_1}^{\lambda_2} R_\lambda(i) d\lambda} + 2.5 \log \frac{\int_{\lambda_1}^{\lambda_2} f_\lambda^0 R_\lambda(i) d\lambda}{\int_{\lambda_1}^{\lambda_2} R_\lambda(i) d\lambda} \\ &= -2.5 \log \frac{\int_{\nu_1}^{\nu_2} f_\nu R_\nu(i) d\nu}{\int_{\nu_1}^{\nu_2} R_\nu(i) d\nu} + 2.5 \log \frac{\int_{\nu_1}^{\nu_2} f_\nu^0 R_\nu(i) d\nu}{\int_{\nu_1}^{\nu_2} R_\nu(i) d\nu} \end{aligned} \tag{5.2}$$

In the case of AB system (e.g., the SDSS system), it can be even simplified if the model SED is in the unit of erg $\mathrm{cm}^{-2}\mathrm{s}^{-1}\mathrm{Hz}^{-1}$,

$$\begin{aligned} m_i &= -2.5\log\frac{\int_{\lambda_1}^{\lambda_2} f_\lambda R_\lambda(i)d\lambda}{\int_{\nu_1}^{\nu_2} R_\nu(i)d\nu} - 48.6 \\ &= -2.5\log\frac{\int_{\nu_1}^{\nu_2} f_\nu R_\nu(i)d\nu}{\int_{\nu_1}^{\nu_2} R_\nu(i)d\nu} - 48.6 \end{aligned} \tag{5.3}$$

In the case of photon counting system (most of the modern CCD device), equation (5.1) becomes:

$$\begin{aligned} m_i &= -2.5\log\frac{\int_{\lambda_1}^{\lambda_2} \lambda f_\lambda R_\lambda(i)d\lambda}{\int_{\lambda_1}^{\lambda_2} \lambda f_\lambda^0 R_\lambda(i)d\lambda} + m_i^0 \\ &= -2.5\log\frac{\int_{\nu_1}^{\nu_2} f_\nu R_\nu(i)d\nu/\nu}{\int_{\nu_1}^{\nu_2} f_\nu^0 R_\nu(i)d\nu/\nu} + m_i^0 \end{aligned} \tag{5.4}$$

equation (5.2) becomes:

$$\begin{aligned} m_i &= -2.5\log\frac{\int_{\lambda_1}^{\lambda_2} \lambda f_\lambda R_\lambda(i)d\lambda}{\int_{\lambda_1}^{\lambda_2} \lambda R_\lambda(i)d\lambda} + 2.5\log\frac{\int_{\lambda_1}^{\lambda_2} \lambda f_\lambda^0 R_\lambda(i)d\lambda}{\int_{\lambda_1}^{\lambda_2} \lambda R_\lambda(i)d\lambda} \\ &= -2.5\log\frac{\int_{\nu_1}^{\nu_2} f_\nu R_\nu(i)d\nu/\nu}{\int_{\nu_1}^{\nu_2} R_\nu(i)d\nu/\nu} + 2.5\log\frac{\int_{\nu_1}^{\nu_2} f_\nu^0 R_\nu(i)d\nu/\nu}{\int_{\nu_1}^{\nu_2} R_\nu(i)d\nu/\nu} \end{aligned} \tag{5.5}$$

and equation (5.3) becomes:

$$\begin{aligned} m_i &= -2.5\log\frac{\int_{\lambda_1}^{\lambda_2} \lambda f_\lambda R_\lambda(i)d\lambda}{\int_{\lambda_1}^{\lambda_2} \nu R_\lambda(i)d\lambda} - 48.6 \\ &= -2.5\log\frac{\int_{\nu_1}^{\nu_2} f_\nu R_\nu(i)d\nu/\nu}{\int_{\nu_1}^{\nu_2} R_\nu(i)d\nu/\nu} - 48.6 \end{aligned} \tag{5.6}$$

The bolometric correction (BC_i) in a given band i is defined as

$$m_{\mathrm{bol}} = m_i + \mathrm{BC}_i \tag{5.7}$$

so,

$$\mathrm{BC}_i = m_{\mathrm{bol}} - m_i \tag{5.8}$$

The SEDs in our stellar spectral libraries are from different sources, thus we first normalize the SED to $1L_{\odot}$, and then put them to 10 pc. Therefore, the models SEDs have the flux in unit of erg $cm^{-2}s^{-1}Hz^{-1}$. and the equations (5.2), (5.3), (5.5) and (5.6) can be used. We take the luminosity of the Sun to be $L_{\odot} = 3.846 \times 10^{33}$erg s^{-1} and its absolute bolometric magnitude to be $M_{\rm bol}(\rm Sun) = 4.7554$. When transforming the tracks or isochrones into observable magnitudes, the bolometric magnitudes are determined through

$$M_{\rm bol} = -2.5 \log(L/L_{\odot}) - 4.7554. \tag{5.9}$$

Then the bolometric correction of a specific band is calculated from equation (5.8).

5.7 Empirical stellar spectral libraries

The MILES library (Sánchez-Blázquez et al. 2006) is one of the most popular empirical libraries for stellar population synthesis. It contains 985 stars spanning a large range in atmospheric parameters ([Fe/H] ranges from -2.31 to 0.3, effective temperature $T_{\rm eff}$ from 3330 K to 21581 K, and gravity $\log g$ from 0.84 to 5.08) with wavelength covering $3525 - 7500$Å.

The IRTF library consists of 226 Solar metallicity stars with spectral type from T to F types, with wavelength covering $0.8 - 5\mu$m (some of them only covers $0.8 - 2.4\mu$m). The spectra for hot stars are not yet released.

For the purpose of stellar population synthesis for old stellar populations. We have done some work by matching the two libraries. We match MILES with IRTF library using spectral classification (luminosity class and spectral type), and then extend them to broader wavelength range with theoretical stellar library (Lejeune et al. 1997). The resulted spectra covers blue-optical (with MILES) to NIR band (with IRTF). In total, there are 244 matched stars. Since the IRTF library does not contain early types stars, our final stellar library is lack of hot stars, which constraints our SSP with empirical stellar library for older stellar systems, like early type galaxies. At blue and red wavelengths where the stellar library wavelength ends, we use the BaSeL3.1 library to extend them and also for some gaps where MILES and IRTF do not cover or because of the telluric influence. In figure 5.3 we show the distribution of these stars on the $log\, T_{\rm eff}$ .vs. $\log g$ diagram. As we see, the empirical library coverage is not very well compared to theoretical

ones. In figure 5.4, we show some examples or the matched spectra. In figure 5.5, we show the temperature scale of the matched library. The red solid line is the Casagrande et al. (2008) temperature scale. As we can see that our matched spectra follow a very well relation, with some difference with respect to th Casagrande et al. (2008) one.

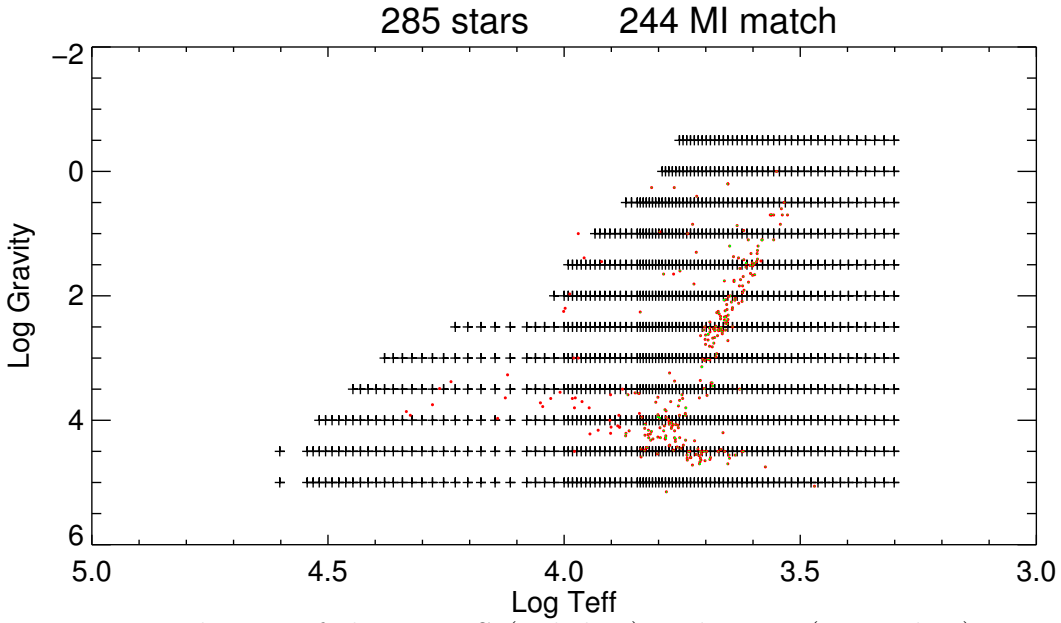

Figure 5.3: Distribution of the MILES (red dots) and IRTF (green dots) stars. The background is the BaSeL3.1 library (Lejeune et al. 1997).

This matched library was used in our work Loli Martínez-Aldama et al. (2015) and Martínez-Aldama et al. (2014).

The other two influential empirical stellar spectral libraries are X-shooter Spectral Library (XSL)[1] (Chen et al. 2014b), and the HST STIS Advanced Spectral Library Project (ASTRAL)[2] (Ayres 2010; Carpenter & Ayres 2015).

[1] http://xsl.u-strasbg.fr/.
[2] http://casa.colorado.edu/~ayres/ASTRAL/.

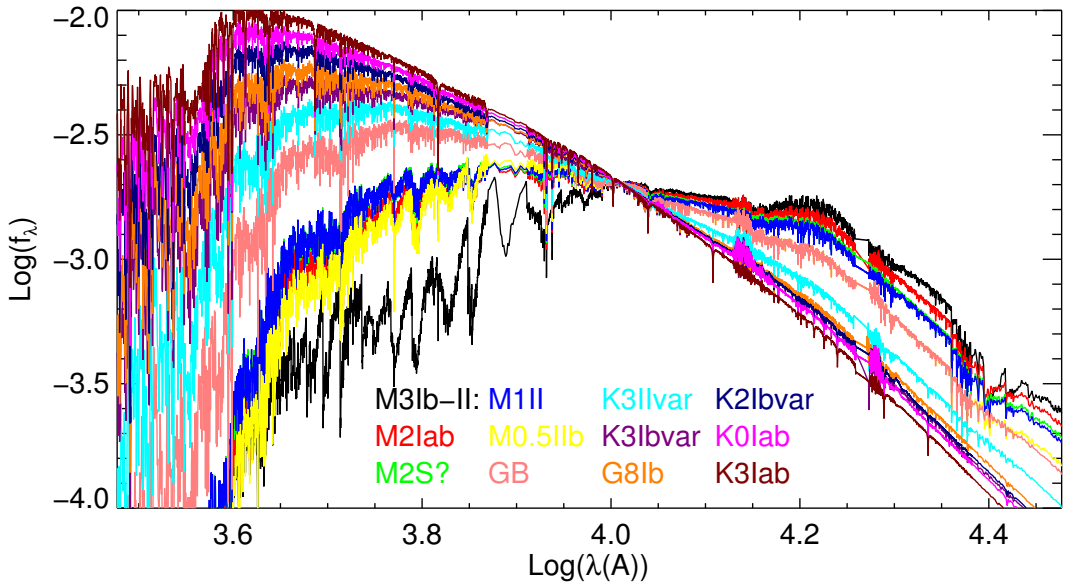

Figure 5.4: Examples of the MILES and IRTF matched spectra.

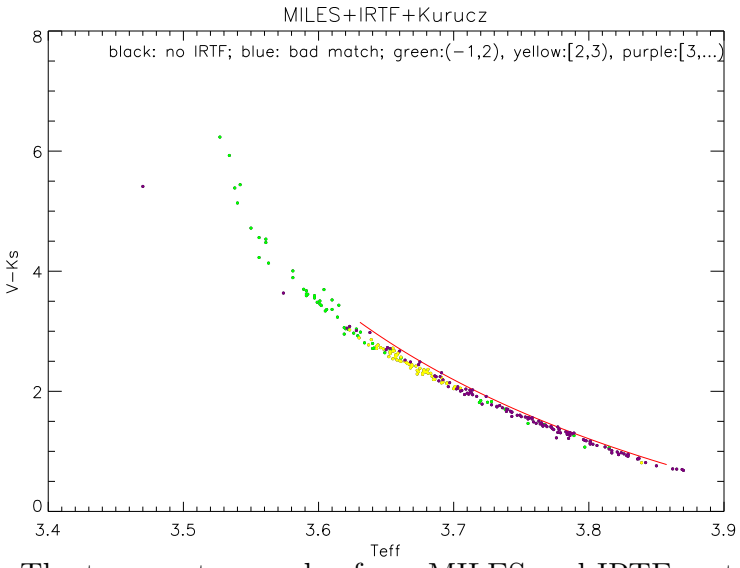

Figure 5.5: The temperature scale of our MILES and IRTF matched library.

Chapter 6

Galaxy size evolution and stellar properties of high-redshift galaxies at $z \sim 1 - 3$

As a student of the joint Ph.D. programme between SISSA-USTC, I also work partly with the group in USTC. The main topics are the stellar and morphological properties of high-redshift galaxies. Here I give a very short summary of some selected work. My main contributions to all these work are on the galaxy structure fittings and stellar population synthesis. The galaxy fitting is done with the *Galfit* package (Peng et al. 2002). Galfit is a tool for extracting information on galaxies, stars, globular cluster, stellar disks, etc., by using parametric functions to model objects as they appear in two-dimensional digital images. For the model profile, we take the Sérsic function (Sérsic 1963). The Point Source Functions are also needed to be convolved with the Sérsic profile to fit the galaxies. We use the empirical PSFs models extracted from star-like objects in the field with PSFEx code (Bertin 2011). For deriving the stellar properties from the multi-band photometric data, the Bruzual & Charlot (2003) models are used.

6.1 Galaxy size evolution

Large Size Scatter of Passively Evolving Lensed Galaxies at $z \sim 2$ in CLASH (Fan et al. 2013a)

In this work, we systematically search over 11 cluster fields from the Cluster Lensing And Supernova survey with Hubble (Postman et al. 2012, CLASH[1]). We identify ten passively evolving massive galaxies at redshift $z \sim 2$. We derive the stellar properties of these galaxies using Hubble Space Telescope (HST) Wide Field Camera 3 (WFC3) and Advanced Camera for Surveys (ACS) multiband data, together with Spitzer IRAC observations. We also deduce the optical rest-frame effective radius of these high redshift objects. The derived stellar masses and measured effective radii have been corrected by the lensing magnification factors, which are estimated by simply adopting the spherical Navarro-Frenk-White (NFW Navarro et al. 1996) model for the foreground cluster lens. The observed near-IR images, obtained by HST WFC3 camera with high spatial resolution and lensed by the foreground clusters, enable us to study the structures of such systems. Nine out of ten galaxies have on average three times smaller effective radius than local ETGs of similar stellar masses, in agreement with previous works at redshift $1.5 < z < 2.5$. Combined with literature data for $z \sim 2$ (Cimatti et al. 2008; Szomoru et al. 2012; Cassata et al. 2010; Ryan et al. 2012; Zirm et al. 2012), we find that the mass-normalized effective radius scales with redshift as $r_e/M_\star^{0.56} \propto (1+z)^{-1.13}$. We confirm that their size distribution shows a large scatter: from normal size to ~ 5 times smaller compared to local ETGs with similar stellar masses (Shen et al. 2003). The 1-σ scatter $\sigma_{\log r_e}$ of the size distribution is 0.22 and 0.34 at $z \sim 1.6$ and $z \sim 2.1$, respectively. The observed large size scatter has to be carefully taken into account in galaxy evolution model predictions.

The structure of massive quiescent galaxies at z∼3 in the CANDELS-COSMOS field (Fan et al. 2013b)

In this work, we use a two-color $(J-L)$ vs. $(V-J)$ selection criteria to search massive, quiescent galaxy candidates at $2.5 \leq z \leq 4.0$ in the Cosmic Assembly Near-infrared Deep Extragalactic Legacy Survey (CANDELS)-Cosmic Evolution Survey (COSMOS)

[1] http://www.stsci.edu/~postman/CLASH/Home.html.

field (Scoville et al. 2007; Grogin et al. 2011; Koekemoer et al. 2011). We construct a $H_{\rm F160W}$-selected catalogue and complement it with public auxiliary data (van der Wel et al. 2012)[2]. We finally obtain 19 passive VJL-selected (hereafter pVJL) galaxies as the possible massive quiescent galaxy candidates at $z \sim 3$ by several constrains. We find the sizes of our pVJL galaxies are on average 3-4 times smaller than those of local ETGs with analogous stellar mass (Shen et al. 2003). The compact size of these $z \sim 3$ galaxies can be modelled by assuming their formation at $z_{form} \sim 4-6$ according to the dissipative collapse of baryons. Up to $z < 4$, the mass-normalized size evolution can be described by $r_e \propto (1+z)^{-1.0}$. Low Sérsic index and axis ratio, with median values n$\sim$ 1.5 and $b/a \sim 0.65$ respectively, indicate most of pVJL galaxies are disk-dominated. Despite large uncertainty, the inner region of the median mass profile of our pVJL galaxies is similar to those of quiescent galaxies (QGs) at $0.5 < z < 2.5$ and local Early-type galaxies (ETGs). It indicates local massive ETGs have been formed according to an inside-out scenario: the compact galaxies at high redshift make up the cores of local massive ETGs and then build up the outskirts according to dissipationless minor mergers.

Structure and morphology of x-ray selected agn hosts at $1 < z < 3$ in CANDELS-COSMOS field (Fan et al. 2014)

In this paper, we analyze morphologies of the host galaxies of 35 X-ray selected active galactic nucleus (AGNs) at $z \sim 2$ in the COSMOS field using HST/WFC3 imaging taken from the CANDELS survey. We build a control sample of 350 galaxies in total, by selecting ten non-active galaxies drawn from the same field with the similar stellar mass and redshift for each AGN host. By performing two dimensional fitting with GALFIT on the surface brightness profile, we find that the distribution of Sérsic index (n) of AGN hosts does not show a statistical difference from that of the control sample. We measure the nonparametric morphological parameters (the asymmetry index A, the Gini coefficient G, the concentration index C and the M_{20} index) based on point source subtracted images. All the distributions of these morphological parameters of AGN hosts are consistent with those of the control sample. We finally investigate the fraction of distorted morphologies in both samples by visual classification. Only $\sim$ 15% of the AGN hosts have highly

[2] ftp://cdsarc.u-strasbg.fr/pub/cats/J/ApJS/203/24/.

distorted morphologies, possibly due to a major merger or interaction. We find there is no significant difference in the distortion fractions between the AGN host sample and control sample. We conclude that the morphologies of X-ray selected AGN hosts are similar to those of nonactive galaxies and most AGN activity is not triggered by major merger.

6.2 Properties of Ultra-Luminous Infrared Galaxies

Selection and Mid-infrared Spectroscopy of Ultraluminous Star-Forming Galaxies at $z \sim 2$ (Fang et al. 2014)

In this paper, we use 3.6 to 8 μm color criteria to select Ultraluminous Infrared Galaxies (ULIRGs) at $z \sim 2$, from a sample of 24 μm sources in the Extended Groth Strip. Spectroscopy observation at 20–38 μm of 14 objects verifies their nature and gives their redshifts. Multi-wavelength data for these objects imply stellar masses $>10^{11}$ $M_{\odot}$ and star formation rates $\geq$410 $M_{\odot}$ yr^{-1}. Four objects of this sample observed at 1.6 μm (rest-frame visible) with HST/WFC3 show diverse morphologies, suggesting that multiple formation processes create ULIRGs. Four of the 14 objects show signs of active galactic nuclei, but the luminosity appears to be dominated by star formation in all cases.

6.3 Properties of high-redshift galaxies

Passive and star-forming galaxies at $1.4 \leq z \leq 2.5$ in the AEGIS field (Fang et al. 2012)

Using a simple two-color selection based on g-, z-, and K-band photometry, we pick out 1609 star-forming galaxies (sgzKs) and 422 passively evolving galaxies (pgzKs) at $z \sim 2$ from a K-band- selected sample ($K_{\rm AB} < 22.0$) in an area of ~ 0.44 deg^2 of the All-wavelength Extended Groth Strip International Survey (Davis et al. 2007)[3]. The number counts of pgzKs in our sample turn over at $K_{\rm AB} \sim 21.0$, and both the number of faint and bright objects (including sgzKs and pgzKs) exceed the predictions of a recent semi-

[3] http://aegis.ucolick.org/.

analytic model of galaxy formation, a more successful model is needed to explain this diversity. We also find that the star formation rate (SFR) and specific SFR (sSFR) of sgzKs increases with redshift at all masses, implying that star-forming galaxies were much more active on average in the past. Moreover, the sSFR of massive galaxies is lower at all redshifts, suggesting that star formation contributes more to the mass growth of low-mass galaxies than to high-mass galaxies. From HST/WFC3 near-infrared imaging data, we find that morphologies of $z \sim 2$ galaxies not only have diffuse structures with lower G and higher M_{20} values, but also have single-object morphologies (higher G and lower M_{20}), implying that there are morphological variety and different formation process for these galaxies at $z \sim 2$. Finally, we also study the fraction of active galactic nuclei (AGNs) in the gzKs, 82 of 828 gzKs with four IRAC bands can be classified as AGNs ($\sim 10\%$). Most of these AGN candidates have $L_{0.5-10\ \mathrm{keV}} > 10^{41}\,\mathrm{erg\,s^{-1}}$.

Chapter 7

Summary

In summary, during the period of my Ph.D., I have focused on extending the PARSEC data base on both the very low mass (Chen et al. 2014a) and very massive stars (Chen et al. 2015).

For the very low mass stars, we have replaced the Eddington $T-\tau$ relation used in PARSEC as the boundary conditions with those provided by the Phoenix atmosphere models. We extract the $T-\tau$ relations from Phoenix BT-Settl model atmospheres and use them as the outer boundary conditions in the PARSEC code. We find that this change alone reduces the discrepancy in the mass–radius relation from 8 to 5 per cent. We use the bolometric correction tables derived from atmosphere model spectra to convert the theoretical quantities into colors and magnitudes. Kurucz model spectra are used at $T_{\rm eff} > 6000$ K to derive the bolometric correction tables, while Phoenix model spectra are used below 6000 K. We then compare the models with multi–band photometries of clusters Praesepe, M 67, NGC 6397 and 47 Tuc. We show that the models with the Phoenix $T-\tau$ relations clearly improve the description of the optical colours and magnitudes. However, the models are still systematically fainter and bluer than the observations. We then apply a shift to the above $T-\tau$ relations, increasing from 0 at $T_{\rm eff} = 4730$ K to ∼14 per cent at $T_{\rm eff} = 3160$ K, to reproduce the observed mass–radius radius relation of dwarf stars. Taking this experiment as a calibration of the $T-\tau$ relations, we can reproduce the optical and near-infrared CMDs of low mass stars in the old metal–poor globular clusters NGC 6397 and 47 Tuc, and in the intermediate–age and young Solar–metallicity open clusters M 67 and Praesepe. Thus, we extend PARSEC models using this calibration, providing VLMS models more suitable for the lower main sequence stars over a wide range of metallicities

and wavelengths.

However, we also find that while all the other optical to near-infrared colors are reproduced well by our calibrated models, the $B-V$ color is exceptionally problematic for the very low mass stars. The model $B-V$ colors are bluer than the observation. We argue that part of the discrepancy can be attributed to the uncertainties brought by the linear extrapolation between different photometric systems. Yet a large portion of the disagreement may be originated from problems in the atmosphere model spectra of the B-band. Finally, we discuss the possible origin of the shift, e.g., starspots. Although the starspots can provide some justification on the shifted temperatures, it also worsens the problem in the $B-V$ color. Thus, it may not be the explanation we are seeking for.

For the massive stars, we focus on the most recent mass loss recipes of massive stars. These recipes indicate that mass loss is strongly enhanced when stars approach the Eddington luminosity (Vink et al. 2011), even at low metallicity (Gräfener & Hamann 2008). We implement new metallicity-dependent mass loss rate recipes, derived from Gräfener & Hamann (2008) and Vink et al. (2011), in the PARSEC code. We compute new evolutionary tracks of massive stars up to 350 $M_{\odot}$for $0.0001 \leq Z \leq 0.04$ and from the pre-main sequence to Carbon ignition as presented in Chen et al. (2015). The models reproduce the Humphreys-Davidson limit observed in the Galactic and LMC without ad hoc assumptions for the mass-loss rates. We also generate isochrones of a sufficiently wide range of ages useful for studying star-forming galaxies.

We also compute new stellar spectral library for O, B stars with WM-basic. The models are calculated at three mass loss rates: 10^{-7}, 10^{-6} and $10^{-5}\,\mathrm{M_{\odot}yr^{-1}}$. We use new high resolution Wolf-Rayet stellar spectral library provided at PoWR data base for the WR stars.

The work on the very low mass stars and very massive stars, together with the models for stars with mass between them, complete the PARSEC data base. From these evolutionary tracks, the isochrones can be derived, spanning from very young stellar populations to very old ages.

We also have assembled a large library of stellar atmosphere models: 1) the WM-basic atmosphere models with three mass loss rates computed by us for O, B stars on the main-sequence; 2) the PoWR data base for WR stars; 2) the Phoenix libraries appropriate for cool stars; 4) ATLAS models for intermediate type stars. They provide a fairly well

coverage for the theoretical models as well as the observation. They can be used for transforming theoretical quantities (e.g., luminosity, $T_{\rm eff}$, or $\log g$) to observable ones (e.g., magnitudes and colors). They can also be used for stellar population synthesis.

Finally, I also briefly describe my work on high-redshift galaxies. These work present results on the structure and stellar population evolution of the galaxies from redshift $z \sim 3$ to the present-day.

Appendix A

Table: Solar abundance

Table A.1: Solar abundance in mass fraction.

	PARSEC	Anders & Grevesse (1989)	Grevesse & Sauval (1998)	Caffau et al. (2011)	Asplund et al. (2009)
X	0.73626	0.70500	0.73329	0.73626	0.73741
Y	0.24850	0.27550	0.24965	0.24884	0.24922
Z	0.01524	0.01950	0.01706	0.01490	0.01337

Table A.2: Solar abundance of different sources in $\log(N_i/N_H) + 12$. -100.0 means the value is negligible.

N	element	PARSEC	Anders & Grevesse (1989)	Grevesse & Sauval (1998)	Caffau et al. (2011)	Asplund et al. (2009)
1	H	12.000	12.000	12.000	12.000	12.000
2	HE	10.926	10.990	10.930	10.930	10.930
3	LI	1.026	1.160	1.100	1.030	1.050
4	BE	1.395	1.150	1.400	1.380	1.380
5	B	2.547	2.600	2.550	2.700	2.700
6	C	8.496	8.560	8.520	8.500	8.430
7	N	7.856	8.050	7.920	7.860	7.830
8	O	8.756	8.930	8.830	8.760	8.690
9	F	4.557	4.560	4.560	4.560	4.560
10	Ne	8.016	8.090	8.080	7.930	7.930
11	NA	6.327	6.330	6.330	6.240	6.240
12	MG	7.577	7.580	7.580	7.600	7.600
13	AL	6.467	6.470	6.470	6.450	6.450
14	SI	7.546	7.550	7.550	7.510	7.510
15	P	5.456	5.450	5.450	5.460	5.410
16	S	7.156	7.210	7.330	7.160	7.120
17	CL	5.496	5.500	5.500	5.500	5.500
18	AR	6.397	6.560	6.400	6.400	6.400
19	K	5.106	5.220	5.120	5.110	5.030
20	CA	6.357	6.360	6.360	6.340	6.340
21	SC	3.167	3.100	3.170	3.150	3.150
22	TI	5.016	4.990	5.020	4.950	4.950
23	V	3.996	4.000	4.000	3.930	3.930
24	CR	5.668	5.670	5.670	5.640	5.640
25	MN	5.386	5.390	5.390	5.430	5.430
26	FE	7.516	7.670	7.500	7.520	7.500
27	CO	4.917	4.920	4.920	4.990	4.990
28	NI	6.246	6.250	6.250	6.220	6.220

29	CU	4.207	4.210	4.210	4.190	4.190
30	ZN	4.597	4.600	4.600	4.560	4.560
31	GA	2.876	2.880	2.880	3.040	3.040
32	GE	3.407	3.410	3.410	3.650	3.650
33	AS	2.367	2.370	-100.000	2.300	2.300
34	SE	3.406	3.350	-100.000	3.340	3.340
35	BR	2.626	2.630	-100.000	2.540	2.540
36	KR	3.307	3.230	-100.000	3.250	3.250
37	RB	2.596	2.600	2.600	2.520	2.520
38	SR	2.967	2.900	2.970	2.870	2.870
39	Y	2.236	2.240	2.240	2.210	2.210
40	ZR	2.596	2.500	2.600	2.580	2.580
41	NB	1.416	1.420	1.420	1.460	1.460
42	MO	1.916	1.920	1.920	1.880	1.880
43	TC	-100.000	-100.000	-100.000	-100.000	-100.000
44	RU	1.836	1.840	1.840	1.750	1.750
45	RH	1.116	1.120	1.120	0.910	0.910
46	PD	1.687	1.690	1.690	1.570	1.570
47	AG	0.936	0.940	0.940	0.940	0.940
48	CD	1.766	1.860	1.770	1.710	1.710
49	IN	1.657	1.460	1.660	0.800	0.800
50	SN	1.996	2.000	2.000	2.040	2.040
51	SB	0.996	1.000	1.000	1.010	1.010
52	TE	2.235	2.240	-100.000	2.180	2.180
53	I	1.507	1.510	-100.000	1.550	1.550
54	XE	2.167	2.230	-100.000	2.240	2.240
55	CS	1.126	1.120	-100.000	1.080	1.080
56	BA	2.127	2.130	2.130	2.180	2.180
57	LA	1.167	1.220	1.170	1.100	1.100
58	CE	1.576	1.550	1.580	1.580	1.580
59	PR	0.706	0.710	0.710	0.720	0.720
60	ND	1.497	1.500	1.500	1.420	1.420

61	Pm	-100.000	-100.000	-100.000	-100.000	-100.000
62	Sm	1.006	1.000	1.010	0.960	0.960
63	Eu	0.516	0.510	0.510	0.520	0.520
64	Gd	1.117	1.120	1.120	1.070	1.070
65	Tb	-100.000	0.100	-0.100	0.300	0.300
66	Dy	1.139	1.100	1.140	1.100	1.100
67	Ho	0.257	0.260	0.260	0.480	0.480
68	Er	0.926	0.930	0.930	0.920	0.920
69	Tm	-100.000	0.000	0.000	0.100	0.100
70	Yb	1.077	1.080	1.080	0.840	0.840
71	Lu	0.057	0.760	0.060	0.100	0.100
72	Hf	0.866	0.880	0.880	0.870	0.850
73	Ta	-100.000	0.130	-100.000	-0.120	-0.120
74	W	1.108	1.110	1.110	0.850	0.850
75	Re	0.276	0.270	-100.000	0.260	0.260
76	Os	1.357	1.450	1.450	1.360	1.400
77	Ir	1.346	1.350	1.350	1.380	1.380
78	Pt	1.797	1.800	1.800	1.620	1.620
79	Au	1.007	1.010	1.010	0.920	0.920
80	Hg	1.128	1.090	-100.000	1.170	1.170
81	Tl	0.896	0.900	0.900	0.900	0.900
82	Pb	1.946	1.850	1.950	1.750	1.750
83	Bi	0.707	0.710	-100.000	0.650	0.650
84	Po	-100.000	-100.000	-100.000	-100.000	-100.000
85	At	-100.000	-100.000	-100.000	-100.000	-100.000
86	Rn	-100.000	-100.000	-100.000	-100.000	-100.000
87	Fr	-100.000	-100.000	-100.000	-100.000	-100.000
88	Ra	-100.000	-100.000	-100.000	-100.000	-100.000
89	Ac	-100.000	-100.000	-100.000	-100.000	-100.000
90	Th	0.077	0.120	-100.000	0.080	0.020
91	Pa	-100.000	-100.000	-100.000	-100.000	-100.000
92	U	-100.000	-0.470	-0.450	-0.540	-0.540

Appendix B

Table: Notations of PARSEC models

Table B.1: Summary of the PARSEC models.

Model	BC_λ	$T-\tau$	BC_λ tables used for VLMS	basic description
v1.1	OBC	Gray atmosphere	Castelli & Kurucz (2003) and Allard et al. (2000)	previous version of PARSEC models and BC_λ tables
v1.1	NBC	Gray atmosphere	Castelli & Kurucz (2003) + Phoenix BT-Settl	PARSEC v1.1 models interpolated with our new BC_λ tables
v1.2	NBC	Phoenix BT-Settl	Castelli & Kurucz (2003) + Phoenix BT-Settl	new VLMS models with $T-\tau$ relation from Phoenix BT-Settl
v1.2S	NBC	Calibrated Phoenix BT-Settl	Castelli & Kurucz (2003) + Phoenix BT-Settl	new VLMS models with calibrated $T-\tau$ relation with respect to Phoenix BT-Settl

Appendix C

Table: observed stellar parameters (mass & radius) for very low mass stars

Table C.1: Mass-radius data. Notations used are AS: asteroseismic; SYN: spin-orbit synchronisation; SB1: single-lined binary; EH: exoplanet host. 2MASS04463285: 2MASS04463285+1901432. LP133-373: mass ratio=1 assumed.

Name	$M_*(M_\odot)$	$\sigma(M_*(M_\odot))$	$R_*(R_\odot)$	$\sigma(R_*(R_\odot))$	System type	Method	Ref.[1]	Com
KIC6521045	1.08	±0.06	1.49	±0.04	single	AS	[1]	EH
KIC3544595	0.91	±0.06	0.92	±0.02	single	AS	[1]	EH
KIC4914423	1.09	±0.07	1.44	±0.04	single	AS	[1]	EH
KIC8349582	1.08	±0.08	1.41	±0.04	single	AS	[1]	EH
KIC5094751	1.04	±0.06	1.32	±0.04	single	AS	[1]	EH
KIC4349452	1.19	±0.06	1.31	±0.02	single	AS	[1]	EH
KIC8478994	0.80	±0.07	0.77	±0.03	single	AS	[1]	EH
KIC11295426	1.08	±0.05	1.24	±0.02	single	AS	[1]	EH
KIC8753657	1.07	±0.06	1.07	±0.02	single	AS	[1]	EH
KIC10963065	1.08	±0.07	1.23	±0.03	single	AS	[1]	EH
KIC9955598	0.92	±0.06	0.89	±0.02	single	AS	[1]	EH
TrES-2	0.94	±0.05	0.95	±0.02	single	RV	[2]	EH
HATS550-016_P	0.97	$^{+0.05}_{-0.06}$	1.22	$^{+0.02}_{-0.03}$	binary	SYN	[3]	SB1

HATS550-016_S	0.110	$^{+0.005}_{-0.006}$	0.147	$^{+0.003}_{-0.004}$	binary SYN	[3]	SB1
HATS551-019_P	1.10	$^{+0.05}_{-0.09}$	1.70	$^{+0.09}_{-0.09}$	binary SYN	[3]	SB1
HATS551-019_S	0.17	$^{+0.01}_{-0.01}$	0.18	$^{+0.01}_{-0.01}$	binary SYN	[3]	SB1
HATS551-021_P	1.1	$^{+0.1}_{-0.1}$	1.20	$^{+0.08}_{-0.01}$	binary SYN	[3]	SB1
HATS551-021_S	0.132	$^{+0.014}_{-0.005}$	0.154	$^{+0.006}_{-0.008}$	binary SYN	[3]	SB1
HATS553-001_P	1.2	$^{+0.1}_{-0.1}$	1.58	$^{+0.08}_{-0.03}$	binary SYN	[3]	SB1
HATS553-001_S	0.20	$^{+0.01}_{-0.02}$	0.22	$^{+0.01}_{-0.01}$	binary SYN	[3]	SB1
HP_Aur_P	0.9543	±0.0041	1.0278	±0.0042	binary RV	[4]	
HP_Aur_S	0.8094	±0.0036	0.7758	±0.0034	binary RV	[4]	
V65_P	0.8035	±0.0086	1.1470	±0.0104	binary RV	[5]	
V65_S	0.6050	±0.0044	0.6110	±0.0092	binary RV	[5]	
V66_P	0.7842	±0.0045	0.9347	±0.0048	binary RV	[5]	
V66_S	0.7443	±0.0042	0.8298	±0.0053	binary RV	[5]	
V69_P	0.7665	±0.0053	0.8655	±0.0097	binary RV	[5]	
V69_S	0.7278	±0.0048	0.8074	±0.0080	binary RV	[5]	
HD181068_A	3.0	±0.1	12.46	±0.15	triple RV	[6]	
HD181068_Ba	0.915	±0.034	0.865	±0.010	triple RV	[6]	
HD181068_Bb	0.870	±0.043	0.800	±0.020	triple RV	[6]	
C4780Bb	0.096	±0.011	0.104	±0.0160	binary RV	[7]	primary: F-star
NSVS07394765_P	0.360	±0.005	0.463	±0.004	binary RV	[8]	
NSVS07394765_S	0.180	±0.004	0.496	±0.005	binary RV	[8]	
WTS19g-4-02069_P	0.53	±0.02	0.51	±0.01	binary RV	[9]	
WTS19g-4-02069_S	0.143	±0.006	0.174	±0.006	binary RV	[9]	
KOI-126A	1.3470	±0.0320	2.0254	±0.0098	triple RV	[10]	
KOI-126B	0.2413	±0.0030	0.2543	±0.0014	triple RV	[10]	
KOI-126C	0.2127	±0.0026	0.2318	±0.0013	triple RV	[10]	
KIC6131659_P	0.922	±0.007	0.8800	±0.0028	binary RV	[11]	
KIC6131659_S	0.685	±0.005	0.6395	±0.0061	binary RV	[11]	
MG1-78457_P	0.527	±0.002	0.505	$^{+0.008}_{-0.007}$	binary RV	[12]	
MG1-78457_S	0.491	±0.001	0.471	$^{+0.009}_{-0.007}$	binary RV	[12]	
MG1-116309_P	0.567	±0.002	0.552	$^{+0.004}_{-0.013}$	binary RV	[12]	

MG1-116309_S	0.532	±0.002	0.532	$^{+0.004}_{-0.008}$	binary	RV	[12]	
MG1-506664_P	0.584	±0.002	0.560	$^{+0.001}_{-0.004}$	binary	RV	[12]	
MG1-506664_S	0.544	±0.002	0.513	$^{+0.001}_{-0.008}$	binary	RV	[12]	
MG1-646680_P	0.499	±0.002	0.457	$^{+0.006}_{-0.004}$	binary	RV	[12]	
MG1-646680_S	0.443	±0.002	0.427	$^{+0.006}_{-0.002}$	binary	RV	[12]	
MG1-1819499_P	0.557	±0.001	0.569	$^{+0.002}_{-0.023}$	binary	RV	[12]	
MG1-1819499_S	0.535	±0.001	0.500	$^{+0.003}_{-0.014}$	binary	RV	[12]	
MG1-2056316_P	0.469	±0.002	0.441	$^{+0.002}_{-0.002}$	binary	RV	[12]	
MG1-2056316_S	0.382	±0.001	0.374	$^{+0.002}_{-0.002}$	binary	RV	[12]	
SDSSJ12120123	0.273	±0.002	0.306	±0.007	binary	RV	[13]	prima WD
GK-Vir	0.116	±0.003	0.155	±0.003	binary	RV	[13]	prima WD
SDSSJ0857+0342	0.087	±0.012	0.1096	±0.0038	binary	RV	[14]	prima WD
SDSS01380016	0.132	±0.003	0.165	±0.001	binary	RV	[15]	prima WD
Kepler-16_P	0.6897	$^{+0.0035}_{-0.0034}$	0.6489	$^{+0.0013}_{-0.0013}$	binary	RV	[16]	
Kepler-16_S	0.20255	$^{+0.00066}_{-0.000654}$	0.22623	$^{+0.00059}_{-0.00053}$	binary	RV	[16]	
CM-Dra_P	0.2310	±0.0009	0.2534	±0.0019	binary	RV	[17]	
CM-Dra_S	0.2141	±0.0010	0.2396	±0.0015	binary	RV	[17]	
T-Boo0-00080_P	1.49	±0.07	1.83	±0.03	binary	SYN	[18]	
T-Boo0-00080_S	0.315	±0.010	0.325	±0.005	binary	SYN	[18]	
T-Lyr1-01662_P	0.77	±0.08	1.14	±0.03	binary	SYN	[18]	
T-Lyr1-01662_S	0.198	±0.012	0.238	±0.007	binary	SYN	[18]	
T-Lyr0-08070_P	0.95	±0.11	1.36	±0.05	binary	SYN	[18]	
T-Lyr0-08070_S	0.240	±0.019	0.265	±0.010	binary	SYN	[18]	
T-Cyg1-01385_P	0.91	±0.15	1.63	±0.08	binary	SYN	[18]	
T-Cyg1-01385_S	0.345	±0.034	0.360	±0.017	binary	SYN	[18]	
HAT-TR-205-013_P	1.04	±0.13	1.28	±0.04	binary	RV	[19]	SB1
HAT-TR-205-013_S	0.124	±0.010	0.167	±0.006	binary	RV	[19]	SB1
ASAS-01A_P	0.612	±0.030	0.596	±0.020	multiple	RV	[20]	

ASAS-01A_P	0.445	±0.019	0.445	±0.024	multiple	RV [20]
LSPM-J1112+7626_P	0.3946	±0.0023	0.3860	$^{+0.0055}_{-0.0028}$	binary	RV [21]
LSPM-J1112+7626_S	0.2745	±0.0012	0.2978	$^{+0.0049}_{-0.0046}$	binary	RV [21]
WTS19b-2-01387_P	0.498	±0.019	0.496	±0.013	binary	RV [22]
WTS19b-2-01387_S	0.481	±0.017	0.479	±0.013	binary	RV [22]
WTS19c-3-01405_P	0.410	±0.023	0.398	±0.019	binary	RV [22]
WTS19c-3-01405_S	0.376	±0.024	0.393	±0.019	binary	RV [22]
WTS19e-3-08413_P	0.463	±0.025	0.480	±0.022	binary	RV [22]
WTS19e-3-08413_S	0.351	±0.019	0.375	±0.020	binary	RV [22]
V1061-Cyg_P	1.282	±0.016	1.616	±0.017	binary	RV [23]
V1061-Cyg_S	0.9315	±0.0074	0.967	±0.011	binary	RV [23]
RT-And_P	1.240	±0.030	1.256	±0.015	binary	RV [23]
RT-And_S	0.907	±0.017	0.906	±0.011	binary	RV [23]
FL-Lyr_P	1.218	±0.016	1.283	±0.028	binary	RV [23]
FL-Lyr_S	0.958	±0.012	0.962	±0.028	binary	RV [23]
ZZ-UMa_P	1.1386	±0.0052	1.513	±0.019	binary	RV [23]
ZZ-UMa_S	0.9691	±0.0048	1.1562	±0.0096	binary	RV [23]
α-Cen_P	1.105	±0.007	1.224	±0.003	binary	RV [23]
α-Cen_S	0.934	±0.006	0.863	±0.005	binary	RV [23]
V568-Lyr_P	1.0745	±0.0077	1.400	±0.016	binary	RV [23]
V568-Lyr_S	0.8273	±0.0042	0.7679	±0.0064	binary	RV [23]
V636Cen_P	1.0518	±0.0048	1.0186	±0.0043	binary	RV [23]
V636Cen_S	0.8545	±0.0030	0.8300	±0.0043	binary	RV [23]
CV-Boo_P	1.032	±0.013	1.263	±0.023	binary	RV [23]
CV-Boo_S	0.968	±0.012	1.174	±0.023	binary	RV [23]
V1174-Ori_P	1.006	±0.013	1.338	±0.011	binary	RV [23]
V1174-Ori_S	0.7271	±0.0096	1.063	±0.011	binary	RV [23]
UV-Psc_P	0.9829	±0.0077	1.110	±0.023	binary	RV [23]
UV-Psc_S	0.7644	±0.0045	0.835	±0.018	binary	RV [23]
CG-Cyg_P	0.941	±0.014	0.893	±0.012	binary	RV [23]
CG-Cyg_S	0.814	±0.013	0.838	±0.011	binary	RV [23]
RW-Lac_P	0.9263	±0.0057	1.1864	±0.0038	binary	RV [23]

RW-Lac_S	0.8688	±0.0040	0.9638	±0.0040	binary RV	[23]	
HS-Aur_P	0.898	±0.019	1.004	±0.024	binary RV	[23]	
HS-Aur_S	0.877	±0.017	0.874	±0.024	binary RV	[23]	
GU-Boo_P	0.6101	±0.0064	0.627	±0.016	binary RV	[23]	
GU-Boo_S	0.5995	±0.0064	0.624	±0.016	binary RV	[23]	
YY-Gem_P	0.5992	±0.0047	0.6194	±0.0057	binary RV	[23]	
YY-Gem_S	0.5992	±0.0047	0.6194	±0.0057	binary RV	[23]	
CU-Cnc_P	0.4349	±0.0012	0.4323	±0.0055	binary RV	[23]	
CU-Cnc_S	0.39922	±0.00089	0.3916	±0.0094	binary RV	[23]	
CM-Dra_P	0.23102	±0.00089	0.2534	±0.0019	binary RV	[23]	
CM-Dra_S	0.21409	±0.00083	0.2398	±0.0018	binary RV	[23]	
LP133-373	0.34	±0.02	0.330	±0.014	binary RV	[24]	
ASAS-04_P	0.8338	±0.0036	0.848	±0.005	binary RV	[25]	
ASAS-04_S	0.8280	±0.0040	0.833	±0.005	binary RV	[25]	
GJ3236_P	0.376	±0.016	0.3795	±0.0064	binary RV	[26]	
GJ3236_S	0.281	±0.015	0.2996	±0.0064	binary RV	[26]	
AP-And_P	1.211	±0.024	1.218	±0.013	binary RV	[27]	
AP-And_S	1.222	±0.024	1.226	±0.061	binary RV	[27]	
VZ-Cep_P	1.376	±0.027	1.622	±0.019	binary RV	[27]	
VZ-Cep_S	1.073	±0.023	0.934	±0.025	binary RV	[27]	
V881-Per_P	0.912	±0.039	0.975	±0.020	binary RV	[27]	
V881-Per_S	0.748	±0.035	0.708	±0.018	binary RV	[27]	
IM-Vir_P	0.981	±0.012	1.061	±0.016	binary RV	[28]	
IM-Vir_S	0.6644	±0.0048	0.681	±0.013	binary RV	[28]	
RXJ0239.1_P	0.730	±0.009	0.741	±0.004	binary RV	[29]	
RXJ0239.1_S	0.693	±0.006	0.703	±0.002	binary RV	[29]	
NSVS0103_P	0.5428	±0.0027	0.5260	±0.0028	binary RV	[30]	
NSVS0103_S	0.4982	±0.0025	0.5088	±0.0030	binary RV	[30]	
2MASS04463285_P	0.47	±0.05	0.56	±0.02	binary RV	[31]	
2MASS04463285_S	0.19	±0.02	0.21	±0.01	binary RV	[31]	
KIC1571511_P	1.265	$^{+0.036}_{-0.030}$	1.343	$^{+0.012}_{-0.010}$	binary RV	[32]	SB1
KIC1571511_S	0.141	$^{+0.005}_{-0.004}$	0.1783	$^{+0.0014}_{-0.0017}$	binary RV	[32]	SB1

RR-Cae	0.1825	±0.0131	0.2090	±0.0143	binary RV	[33]	primary: WD
OGLE-TR-123_P	1.29	±0.26	1.55	±0.10	binary RV	[34]	SB1
OGLE-TR-123_S	0.085	±0.011	0.133	±0.009	binary RV	[34]	SB1
OGLE-TR-122_P	0.98	±0.14	1.05	$^{+0.20}_{-0.09}$	binary RV	[35]	SB1
OGLE-TR-122_S	0.092	±0.009	0.120	$^{+0.024}_{-0.013}$	binary RV	[35]	SB1
OGLE-TR-125_S	0.209	±0.033	0.211	±0.027	binary RV	[36]	SB1
OGLE-TR-120_S	0.47	±0.04	0.42	±0.02	binary RV	[36]	SB1
OGLE-TR-114_P	0.82	±0.08	0.73	±0.09	triple RV	[36]	
OGLE-TR-114_S	0.82	±0.08	0.72	±0.09	triple RV	[36]	
OGLE-TR-106_S	0.116	±0.021	0.181	±0.013	binary RV	[36]	SB1
OGLE-TR-78_S	0.243	±0.015	0.24	±0.013	binary RV	[36]	SB1
OGLE-TR-65_P	1.15	±0.03	1.58	±0.07	triple RV	[36]	
OGLE-TR-65_S	1.11	±0.03	1.59	±0.05	triple RV	[36]	
KIC7871531	0.84	±0.02	0.874	±0.008	single AS	[37]	
KIC8006161	1.04	±0.02	0.947	±0.007	single AS	[37]	
KIC8394589	0.94	±0.04	1.116	±0.019	single AS	[37]	
KIC8694723	0.96	±0.03	1.436	±0.024	single AS	[37]	
KIC8760414	0.77	±0.01	1.006	±0.004	single AS	[37]	
KIC9098294	1.00	±0.03	1.154	±0.009	single AS	[37]	
KIC9955598	0.89	±0.02	0.883	±0.008	single AS	[37]	

[1]References: [1] Marcy et al. (2014) table 1; [2] Barclay et al. (2012) table 1; [3] Zhou et al. (2014) table 4; [4] Sandberg Lacy et al. (2014) table 7; [5] Kaluzny et al. (2013) table 12; [6] Borkovits et al. (2013) table 4; [7] Tal-Or et al. (2013) table 4; [8] Çakırlı (2013) table 5; [9] Nefs et al. (2013) table 5; [10] Carter et al. (2011) table 1; [11] Bass et al. (2012) table 6; [12] Kraus et al. (2011) table 8; [13] Parsons et al. (2012a) table 9; [14] Parsons et al. (2012c) table 5; [15] Parsons et al. (2012b) table 4; [16] Doyle et al. (2011) table 1; [17] Morales et al. (2009b) table 9; [18] Fernandez et al. (2009) table 13; [19] Beatty et al. (2007) table 8; [20] Hełminiak et al. (2012) table 5; [21] Irwin et al. (2011) table 10; [22] Birkby et al. (2012) table 11; [23] Torres et al. (2010) table 1; [24] Vaccaro et al. (2007) table 1; [25] Hełminiak & Konacki (2011) table3; [26] Irwin et al. (2009) table 9; [27] Zola et al. (2014) table 6; [28] Morales et al. (2009a) table 11; [29] López-Morales & Shaw (2007) table 2; [30] Lopez-Morales et al. (2006) table 5; [31] Hebb et al. (2006) table 2; [32] Ofir et al. (2012) table 3; [33] Maxted et al. (2007) table 5; [34] Pont et al. (2006) table 2; [35] Pont et al. (2005b) table 2; [36] Pont et al. (2005a) table 7; [37] Metcalfe et al. (2014) table 1.

Appendix D

WM-basic grids for Z=0.02 and $\dot{M} = 10^{-5}\, M_{\odot}/\mathrm{yr}$

Table D.1: The WM-basic grids for Z=0.02 and $\dot{M} = 10^{-5}\, M_{\odot}/\mathrm{yr}$.

T_{eff} (K)	$\log g$	$R(R_{\odot})$	$\dot{M}$ ($10^{-5}\, M_{\odot}/\mathrm{yr}$)	v_{∞}	κ	α	δ
19953.00	2.5000	15.00	1.000	500.0	0.648	0.750	0.1
19953.00	3.0000	18.00	1.000	900.0	0.995	0.690	0.1
19953.00	3.5000	10.00	1.100	610.0	0.990	0.960	0.1
19953.00	4.0000	15.00	0.110	3500.0	2.000	0.600	0.1
21135.00	2.5000	15.00	0.990	580.0	0.485	0.760	0.1
21135.00	3.0000	18.00	1.000	1000.0	0.850	0.680	0.1
21135.00	3.5000	10.00	1.100	3800.0	1.140	0.900	0.1
21135.00	4.0000	14.00	1.100	3300.0	5.430	0.600	0.1
22387.00	2.5000	30.00	1.100	680.0	0.167	0.750	0.1
22387.00	3.0000	18.00	1.000	1100.0	0.730	0.670	0.1
22387.00	3.5000	10.00	0.980	3200.0	1.000	0.870	0.1
22387.00	4.0000	14.00	1.100	3300.0	4.390	0.600	0.1
23714.00	2.5000	30.00	1.100	400.0	0.135	0.700	0.1
23714.00	3.0000	18.00	1.000	1100.0	0.620	0.660	0.1
23714.00	3.5000	10.00	1.000	4700.0	0.880	0.860	0.1
23714.00	4.0000	15.00	1.100	4100.0	2.540	0.650	0.1
25119.00	3.0000	18.00	1.000	1000.0	0.520	0.650	0.1

25119.00	3.5000	17.00	1.100	1700.0	1.110	0.650	0.1
25119.00	4.0000	20.00	1.100	4300.0	1.810	0.620	0.1
25119.00	4.5000	14.00	1.100	4300.0	8.840	0.500	0.1
26607.00	3.0000	18.00	1.100	960.0	0.440	0.640	0.1
26607.00	3.5000	15.80	0.990	2100.0	0.790	0.660	0.1
26607.00	4.0000	18.00	1.200	4500.0	0.980	0.695	0.1
26607.00	4.5000	14.00	1.100	4300.0	7.100	0.500	0.1
28184.00	3.0000	18.00	1.100	1100.0	0.330	0.640	0.1
28184.00	3.5000	14.90	0.990	1900.0	0.750	0.640	0.1
28184.00	4.0000	16.00	1.200	4200.0	0.990	0.683	0.1
28184.00	4.5000	14.00	0.110	4200.0	2.280	0.500	0.1
29854.00	3.0000	18.00	1.100	740.0	0.260	0.630	0.1
29854.00	3.5000	14.20	1.000	1700.0	0.660	0.630	0.1
29854.00	4.0000	15.00	1.200	3900.0	0.950	0.666	0.1
29854.00	4.5000	14.00	0.110	4200.0	1.830	0.500	0.1
31623.00	3.0000	18.00	1.100	490.0	0.170	0.630	0.1
31623.00	3.5000	15.00	1.200	1600.0	0.630	0.600	0.1
31623.00	4.0000	14.00	1.100	3800.0	0.930	0.650	0.1
31623.00	4.5000	14.00	1.100	4300.0	3.700	0.500	0.1
33497.00	3.5000	13.00	0.980	1400.0	0.498	0.600	0.1
33497.00	4.0000	13.00	1.100	3400.0	0.830	0.642	0.1
33497.00	4.5000	14.00	1.100	5000.0	2.230	0.550	0.1
35481.00	3.5000	12.50	1.000	1700.0	0.425	0.580	0.1
35481.00	4.0000	12.80	1.100	3000.0	0.828	0.605	0.1
35481.00	4.5000	14.00	1.000	5000.0	1.790	0.550	0.1
37584.00	3.5000	10.00	0.960	1200.0	0.310	0.650	0.1
37584.00	4.0000	12.00	1.100	3000.0	0.728	0.595	0.1
37584.00	4.5000	14.00	1.100	5000.0	1.440	0.550	0.1
39811.00	3.5000	11.50	1.100	920.0	0.270	0.570	0.1
39811.00	4.0000	11.50	0.970	2400.0	0.620	0.570	0.1
39811.00	4.5000	14.00	1.100	5000.0	1.160	0.550	0.1
42170.00	3.5000	11.00	0.990	600.0	0.160	0.570	0.1

42170.00	4.0000	11.00	0.980	2200.0	0.495	0.570	0.1
42170.00	4.5000	14.00	1.100	4900.0	0.925	0.550	0.1
44668.00	4.0000	10.00	1.000	1900.0	0.445	0.550	0.1
44668.00	4.5000	14.00	1.100	4800.0	0.740	0.550	0.1
47315.00	4.0000	10.00	1.000	1800.0	0.315	0.560	0.1
47315.00	4.5000	14.00	1.100	4500.0	0.660	0.530	0.1
50119.00	4.0000	10.00	1.200	1800.0	0.270	0.570	0.1
50119.00	4.5000	14.00	1.100	3900.0	0.430	0.540	0.1
53088.00	4.0000	10.00	0.980	1600.0	0.151	0.580	0.1
53088.00	4.5000	14.00	1.100	3800.0	0.370	0.530	0.1
56234.00	4.0000	10.00	1.200	1300.0	0.128	0.580	0.1
56234.00	4.5000	14.00	1.100	3500.0	0.350	0.500	0.1
56234.00	5.0000	5.00	1.100	4700.0	0.990	0.565	0.1
59566.00	4.5000	14.00	1.100	3200.0	0.325	0.470	0.1
59566.00	5.0000	5.00	1.100	4600.0	0.890	0.550	0.1
63096.00	4.5000	14.00	1.100	2900.0	0.280	0.450	0.1
63096.00	5.0000	5.00	1.100	4400.0	0.800	0.535	0.1
66834.00	4.5000	14.00	1.100	2700.0	0.225	0.440	0.1
66834.00	5.0000	5.00	1.100	4000.0	0.700	0.510	0.1
70795.00	4.5000	14.00	1.100	2400.0	0.173	0.430	0.1
70795.00	5.0000	5.00	1.100	3900.0	0.610	0.500	0.1
74989.00	4.5000	14.00	0.900	1800.0	0.110	0.410	0.1
74989.00	5.0000	5.00	1.100	3800.0	0.530	0.490	0.1
79433.00	5.0000	5.00	1.100	3700.0	0.450	0.480	0.1
79433.00	6.0000	1.00	1.000	5000.0	7.350	0.420	0.1
84140.00	5.0000	5.00	1.100	3300.0	0.380	0.460	0.1
84140.00	5.5000	2.80	1.100	4800.0	0.910	0.480	0.1
84140.00	6.0000	1.00	1.000	5000.0	5.850	0.420	0.1
89125.00	5.0000	5.00	1.100	2900.0	0.285	0.450	0.1
89125.00	5.5000	2.60	1.100	4400.0	0.870	0.460	0.1
89125.00	6.0000	1.00	1.000	4700.0	4.970	0.400	0.1
94406.00	5.0000	5.00	1.100	2600.0	0.210	0.440	0.1

94406.00	5.5000	2.40	1.100	4300.0	0.840	0.451	0.1
94406.00	6.0000	1.00	1.000	4800.0	3.850	0.410	0.1
100000.00	5.0000	5.00	0.980	2200.0	0.161	0.420	0.1
100000.00	5.5000	2.30	1.100	4000.0	0.760	0.435	0.1

Bibliography

Alexander, D. R., & Ferguson, J. W. 1994, ApJ, 437, 879

Allard, F., & Hauschildt, P. H. 1995, ApJ, 445, 433

Allard, F., Hauschildt, P. H., Alexander, D. R., Ferguson, J. W., & Tamanai, A. 2000, in Astronomical Society of the Pacific Conference Series, Vol. 212, From Giant Planets to Cool Stars, ed. C. A. Griffith & M. S. Marley, 127

Allard, F., Hauschildt, P. H., Alexander, D. R., & Starrfield, S. 1997a, ARA&A, 35, 137

Allard, F., Hauschildt, P. H., Alexander, D. R., & Starrfield, S. 1997b, ARA&A, 35, 137

Allard, F., & Homeier, D. 2012, ArXiv e-prints, arXiv:1206.1021 [astro-ph.SR]

Allard, F., Homeier, D., & Freytag, B. 2012, Royal Society of London Philosophical Transactions Series A, 370, 2765

Alongi, M., Bertelli, G., Bressan, A., & Chiosi, C. 1991a, A&A, 244, 95

Alongi, M., Bertelli, G., Bressan, A., & Chiosi, C. 1991b, A&A, 244, 95

Alongi, M., Bertelli, G., Bressan, A., et al. 1993, A&AS, 97, 851

An, D., Johnson, J. A., Clem, J. L., et al. 2008, ApJS, 179, 326

Anders, E., & Grevesse, N. 1989, Geochim. Cosmochim. Acta, 53, 197

Arnaboldi, M., Rejkuba, M., Retzlaff, J., et al. 2012, The Messenger, 149, 7

Arnett, W. D., Meakin, C., Viallet, M., et al. 2015, ApJ, 809, 30

Asplund, M., Grevesse, N., Sauval, A. J., & Scott, P. 2009, ARA&A, 47, 481

Ayres, T. R. 2010, ApJS, 187, 149

Bailey, J. E., Nagayama, T., Loisel, G. P., et al. 2015, Nature, 517, 56

Baraffe, I., Chabrier, G., Allard, F., & Hauschildt, P. H. 1997, A&A, 327, 1054

Baraffe, I., Chabrier, G., Allard, F., & Hauschildt, P. H. 1998, A&A, 337, 403

Baraffe, I., Homeier, D., Allard, F., & Chabrier, G. 2015, ArXiv e-prints, arXiv:1503.04107 [astro-ph.SR]

Barclay, T., Huber, D., Rowe, J. F., et al. 2012, ApJ, 761, 53

Barsukova, E. A., Goranskij, V. P., Valeev, A. F., & Kaisin, S. S. 2014, ArXiv e-prints, arXiv:1412.7090 [astro-ph.SR]

Bass, G., Orosz, J. A., Welsh, W. F., et al. 2012, ApJ, 761, 157

Bastian, N., Covey, K. R., & Meyer, M. R. 2010, ARA&A, 48, 339

Basu, S., Chaplin, W. J., Elsworth, Y., New, R., & Serenelli, A. M. 2009, ApJ, 699, 1403

Basu, S., Pinsonneault, M. H., & Bahcall, J. N. 2000, ApJ, 529, 1084

Beatty, T. G., Fernández, J. M., Latham, D. W., et al. 2007, ApJ, 663, 573

Bergemann, M., & Nordlander, T. 2014, ArXiv e-prints, arXiv:1403.3088 [astro-ph.SR]

Bertelli, G., Bressan, A. G., & Chiosi, C. 1985, A&A, 150, 33

Bertelli, G., Nasi, E., Girardi, L., & Marigo, P. 2009, A&A, 508, 355

Bertin, E. 2011, in Astronomical Society of the Pacific Conference Series, Vol. 442, Astronomical Data Analysis Software and Systems XX, ed. I. N. Evans, A. Accomazzi, D. J. Mink, & A. H. Rots, 435

Bessel, M. S. 1990, A&AS, 83, 357

Bessell, M. S. 1990, PASP, 102, 1181

Bestenlehner, J. M., Vink, J. S., Gräfener, G., et al. 2011, A&A, 530, L14

Birkby, J., Nefs, B., Hodgkin, S., et al. 2012, MNRAS, 426, 1507

Bohlin, R. C. 2007, in Astronomical Society of the Pacific Conference Series, Vol. 364, The Future of Photometric, Spec-

trophotometric and Polarimetric Standardization, ed. C. Sterken, 315
Böhm-Vitense, E. 1958, ZAp, 46, 108
Borkovits, T., Derekas, A., Kiss, L. L., et al. 2013, MNRAS, 428, 1656
Borucki, W. J., Koch, D. G., Basri, G., et al. 2011, ApJ, 736, 19
Bossini, D., Miglio, A., Salaris, M., et al. 2015, ArXiv e-prints, arXiv:1507.07797 [astro-ph.SR]
Boyajian, T. S., von Braun, K., van Belle, G., et al. 2012, ApJ, 757, 112
Brandt, T. D., & Huang, C. X. 2015, ApJ, 807, 25
Bressan, A., Fagotto, F., Bertelli, G., & Chiosi, C. 1993, A&AS, 100, 647
Bressan, A. G., Chiosi, C., & Bertelli, G. 1981, A&A, 102, 25
Bressan, A., Marigo, P., Girardi, L., et al. 2012, ArXiv e-prints, arXiv:1208.4498 [astro-ph.SR]
Brott, I., de Mink, S. E., Cantiello, M., et al. 2011, A&A, 530, A115
Bruzual, G., & Charlot, S. 2003, MNRAS, 344, 1000
Çakırlı, Ö. 2013, New A, 22, 15
Caffau, E., Ludwig, H.-G., Steffen, M., Freytag, B., & Bonifacio, P. 2011, Sol. Phys., 268, 255
Cai, Z.-Y., Lapi, A., Bressan, A., et al. 2014, ApJ, 785, 65
Campos, F., Kepler, S. O., Bonatto, C., & Ducati, J. R. 2013, MNRAS, 433, 243
Carpenter, K. G., & Ayres, T. R. 2015, in Cambridge Workshop on Cool Stars, Stellar Systems, and the Sun, Vol. 18, 18th Cambridge Workshop on Cool Stars, Stellar Systems, and the Sun, ed. G. T. van Belle & H. C. Harris, 1041
Carrera, R., & Pancino, E. 2011, A&A, 535, A30
Carretta, E., Bragaglia, A., Gratton, R. G., et al. 2010, A&A, 516, A55
Carter, J. A., Fabrycky, D. C., Ragozzine, D., et al. 2011, Science, 331, 562
Casagrande, L., Flynn, C., & Bessell, M. 2008, MNRAS, 389, 585
Cassata, P., Giavalisco, M., Guo, Y., et al. 2010, ApJ, 714, L79
Castelli, F., & Kurucz, R. L. 2003, in IAU Symposium, Vol. 210, Modelling of Stellar Atmospheres, ed. N. Piskunov, W. W. Weiss, & D. F. Gray, 20P
Castelli, F., & Kurucz, R. L. 2004, ArXiv Astrophysics e-prints, astro-ph/0405087
Castor, J. I., Abbott, D. C., & Klein, R. I. 1975, ApJ, 195, 157
Chabrier, G. 2001, ApJ, 554, 1274
Chen, Y., Bressan, A., Girardi, L., et al. 2015, ArXiv e-prints, arXiv:1506.01681 [astro-ph.SR]
Chen, Y., Girardi, L., Bressan, A., et al. 2014a, MNRAS, 444, 2525
Chen, Y.-P., Trager, S. C., Peletier, R. F., et al. 2014b, A&A, 565, A117
Chieffi, A., Domínguez, I., Höflich, P., Limongi, M., & Straniero, O. 2003, MNRAS, 345, 111
Chieffi, A., & Limongi, M. 2013, ApJ, 764, 21
Chiosi, C., Bertelli, G., & Bressan, A. 1992, ARA&A, 30, 235
Cimatti, A., Cassata, P., Pozzetti, L., et al. 2008, A&A, 482, 21
Copeland, H., Jensen, J. O., & Jorgensen, H. E. 1970, A&A, 5, 12
Cordero, M. J., Pilachowski, C. A., Johnson, C. I., et al. 2014, ApJ, 780, 94
Crowther, P. A. 2007, ARA&A, 45, 177
Crowther, P. A. 2015, ArXiv e-prints, arXiv:1509.00495 [astro-ph.SR]
Crowther, P. A., De Marco, O., & Barlow, M. J. 1998, MNRAS, 296, 367
Crowther, P. A., Schnurr, O., Hirschi, R., et al. 2010, MNRAS, 408, 731
Cutri, R. M., Skrutskie, M. F., van Dyk, S., et al. 2003, 2MASS All Sky Catalog of point sources. (NASA/IPAC)
Cyburt, R. H., Amthor, A. M., Ferguson, R., et al. 2010, ApJS, 189, 240
Dahn, C. C., Harris, H. C., Vrba, F. J., et al. 2002, AJ, 124, 1170
Dale, J. E., Ercolano, B., & Bonnell, I. A. 2012, MNRAS, 424, 377
Dale, J. E., Ercolano, B., & Bonnell, I. A. 2013, MNRAS, 430, 234
D'Antona, F., Di Criscienzo, M., Decressin, T., et al. 2015, ArXiv e-prints, arXiv:1508.01932 [astro-ph.SR]
Davis, M., Guhathakurta, P., Konidaris, N. P., et al. 2007, ApJ, 660, L1
de Jager, C., Nieuwenhuijzen, H., & van der Hucht, K. A. 1988, A&AS, 72, 259

Decressin, T., Mathis, S., Palacios, A., et al. 2009, A&A, 495, 271
Deheuvels, S., Michel, E., Goupil, M. J., et al. 2010, A&A, 514, A31
Dewitt, H. E., Graboske, H. C., & Cooper, M. S. 1973, ApJ, 181, 439
di Criscienzo, M., Ventura, P., & D'Antona, F. 2010, Ap&SS, 328, 167
Dotter, A., Chaboyer, B., Jevremović, D., et al. 2008, ApJS, 178, 89
Doyle, L. R., Carter, J. A., Fabrycky, D. C., et al. 2011, Science, 333, 1602
Eggleton, P. P. 1971, MNRAS, 151, 351
Eker, Z., Bilir, S., Soydugan, F., et al. 2014, ArXiv e-prints, arXiv:1403.1583 [astro-ph.SR]
Ekström, S., Georgy, C., Eggenberger, P., et al. 2012, A&A, 537, A146
Evans, C. J., Smartt, S. J., Lee, J.-K., et al. 2005, A&A, 437, 467
Ezer, D., & Cameron, G. W. 1963, Icarus, 1, 422
Fagotto, F., Bressan, A., Bertelli, G., & Chiosi, C. 1994, A&AS, 104, 365
Fan, L., Chen, Y., Er, X., et al. 2013a, MNRAS, 431, L15
Fan, L., Fang, G., Chen, Y., et al. 2014, ApJ, 784, L9
Fan, L., Fang, G., Chen, Y., et al. 2013b, ApJ, 771, L40
Fang, G., Huang, J.-S., Willner, S. P., et al. 2014, ApJ, 781, 63
Fang, G., Kong, X., Chen, Y., & Lin, X. 2012, ApJ, 751, 109
Feiden, G. A., & Chaboyer, B. 2012, ApJ, 757, 42
Feiden, G. A., & Chaboyer, B. 2013, ApJ, 779, 183
Ferguson, J. W., Alexander, D. R., Allard, F., et al. 2005, ApJ, 623, 585
Fernandez, J. M., Latham, D. W., Torres, G., et al. 2009, ApJ, 701, 764
Frischknecht, U., Hirschi, R., Meynet, G., et al. 2010, A&A, 522, A39
Fu, X., Bressan, A., Molaro, P., & Marigo, P. 2015, MNRAS, 452, 3256
Girardi, L., Bertelli, G., Bressan, A., et al. 2002a, A&A, 391, 195
Girardi, L., Bertelli, G., Bressan, A., et al. 2002b, A&A, 391, 195
Girardi, L., Bressan, A., Bertelli, G., & Chiosi, C. 2000, A&AS, 141, 371
Girardi, L., Eggenberger, P., & Miglio, A. 2011, MNRAS, 412, L103
Girardi, L., Rubele, S., & Kerber, L. 2009, MNRAS, 394, L74
Goudfrooij, P., Girardi, L., Kozhurina-Platais, V., et al. 2014, ApJ, 797, 35
Graboske, H. C., Dewitt, H. E., Grossman, A. S., & Cooper, M. S. 1973, ApJ, 181, 457
Gräfener, G., & Hamann, W.-R. 2008, A&A, 482, 945
Gräfener, G., Koesterke, L., & Hamann, W.-R. 2002, A&A, 387, 244
Green, G. M., Schlafly, E. F., Finkbeiner, D. P., et al. 2014, ApJ, 783, 114
Greggio, L., & Renzini, A. 2011, Stellar Populations. A User Guide from Low to High Redshift
Grevesse, N., & Noels, A. 1993, in Origin and Evolution of the Elements, ed. N. Prantzos, E. Vangioni-Flam, & M. Casse, 15
Grevesse, N., & Sauval, A. J. 1998, Space Sci. Rev., 85, 161
Grogin, N. A., Kocevski, D. D., Faber, S. M., et al. 2011, ApJS, 197, 35
Gustafsson, B., Edvardsson, B., Eriksson, K., et al. 2008, A&A, 486, 951
Haft, M., Raffelt, G., & Weiss, A. 1994, ApJ, 425, 222
Hainich, R., Rühling, U., Todt, H., et al. 2014, A&A, 565, A27
Hamann, W.-R., & Gräfener, G. 2003, A&A, 410, 993
Hamann, W.-R., & Gräfener, G. 2004, A&A, 427, 697
Hamann, W.-R., Gräfener, G., & Liermann, A. 2006, A&A, 457, 1015
Hansen, B. M. S., Kalirai, J. S., Anderson, J., et al. 2013, Nature, 500, 51
Hebb, L., Wyse, R. F. G., Gilmore, G., & Holtzman, J. 2006, AJ, 131, 555
Hełminiak, K. G., & Konacki, M. 2011, A&A, 526, A29
Hełminiak, K. G., Konacki, M., RóŻyczka, M., et al. 2012, MNRAS, 425, 1245
Henyey, L. G., Forbes, J. E., & Gould, N. L. 1964, ApJ, 139, 306

Herwig, F. 2000, A&A, 360, 952
Hillier, D. J., & Miller, D. L. 1998, ApJ, 496, 407
Hofmeister, E., Kippenhahn, R., & Weigert, A. 1964, ZAp, 59, 215
Hollenbach, D. J., & Tielens, A. G. G. M. 1999, Reviews of Modern Physics, 71, 173
Hummer, D. G., & Mihalas, D. 1988, ApJ, 331, 794
Humphreys, R. M., & Davidson, K. 1979, ApJ, 232, 409
Hunter, I., Brott, I., Lennon, D. J., et al. 2008, ApJ, 676, L29
Iglesias, C. A., & Rogers, F. J. 1996, ApJ, 464, 943
Irwin, A. W. 2012, FreeEOS: Equation of State for stellar interiors calculations, Astrophysics Source Code Library, ascl:1211.002
Irwin, J. M., Quinn, S. N., Berta, Z. K., et al. 2011, ApJ, 742, 123
Irwin, J., Charbonneau, D., Berta, Z. K., et al. 2009, ApJ, 701, 1436
Itoh, N., & Kohyama, Y. 1983, ApJ, 275, 858
Itoh, N., Uchida, S., Sakamoto, Y., Kohyama, Y., & Nozawa, S. 2008, ApJ, 677, 495
Ivezić, Ž., Beers, T. C., & Jurić, M. 2012, ARA&A, 50, 251
Jackson, R. J., & Jeffries, R. D. 2014, ArXiv e-prints, arXiv:1404.0683 [astro-ph.SR]
Jurić, M., Ivezić, Ž., Brooks, A., et al. 2008, ApJ, 673, 864
Kalirai, J. S., Richer, H. B., Anderson, J., et al. 2012, AJ, 143, 11
Kaluzny, J., Thompson, I. B., Rozyczka, M., et al. 2013, AJ, 145, 43
Kamai, B. L., Vrba, F. J., Stauffer, J. R., & Stassun, K. G. 2014, AJ, 148, 30
Kamath, D., Wood, P. R., Soszyński, I., & Lebzelter, T. 2010, MNRAS, 408, 522
Kato, S. 1966, PASJ, 18, 374
Kennicutt, Jr., R. C. 1998, ARA&A, 36, 189
Kiminki, M. M., Kim, J. S., Bagley, M. B., Sherry, W. H., & Rieke, G. H. 2015, ArXiv e-prints, arXiv:1509.00081 [astro-ph.SR]
Kimm, T., & Cen, R. 2014, ApJ, 788, 121
Kippenhahn, R., Weigert, A., & Weiss, A. 2013, Stellar Structure and Evolution (Springer-Verlag Berlin Heidelberg)
Koekemoer, A. M., Faber, S. M., Ferguson, H. C., et al. 2011, ApJS, 197, 36
Komatsu, E., Smith, K. M., Dunkley, J., et al. 2011, ApJS, 192, 18
Korn, A., Grundahl, F., Richard, O., et al. 2006, The Messenger, 125, 6
Kraus, A. L., Tucker, R. A., Thompson, M. I., Craine, E. R., & Hillenbrand, L. A. 2011, ApJ, 728, 48
Krishna Swamy, K. S. 1966, ApJ, 145, 174
Kroupa, P. 2001, MNRAS, 322, 231
Kudritzki, R.-P., & Puls, J. 2000, ARA&A, 38, 613
Kurucz, R. L. 1995, private communication
Lamers, H. J. G. L. M. 1989, in Astrophysics and Space Science Library, Vol. 157, IAU Colloq. 113: Physics of Luminous Blue Variables, ed. K. Davidson, A. F. J. Moffat, & H. J. G. L. M. Lamers, 135
Lawrence, A., Warren, S. J., Almaini, O., et al. 2007, MNRAS, 379, 1599
Ledoux, P. 1947, ApJ, 105, 305
Leggett, S. K. 1992, ApJS, 82, 351
Lejeune, T., Cuisinier, F., & Buser, R. 1997, A&AS, 125, 229
Lester, J. B., & Neilson, H. R. 2008, A&A, 491, 633
Li, A. 2005, in American Institute of Physics Conference Series, Vol. 761, The Spectral Energy Distributions of Gas-Rich Galaxies: Confronting Models with Data, ed. C. C. Popescu & R. J. Tuffs, 123
Li, C., de Grijs, R., & Deng, L. 2014, Nature, 516, 367
Loli Martínez-Aldama, M., Dultzin, D., Marziani, P., et al. 2015, ApJS, 217, 3
Lopez-Morales, M., Orosz, J. A., Shaw, J. S., et al. 2006, ArXiv Astrophysics e-prints, astro-ph/0610225
López-Morales, M., & Shaw, J. S. 2007, in Astronomical Society of the Pacific Conference Series, Vol. 362, The Seventh Pacific Rim Conference on Stellar Astrophysics, ed. Y. W. Kang, H.-W. Lee, K.-C. Leung, & K.-S. Cheng, 26

MacDonald, J., & Mullan, D. J. 2013, ApJ, 765, 126
Mackey, J., Langer, N., Mohamed, S., et al. 2014, ASTRA Proceedings, 1, 61
Maeder, A. 1987, A&A, 173, 247
Maeder, A. 1992, in Instabilities in Evolved Super- and Hypergiants, ed. C. de Jager & H. Nieuwenhuijzen, 138
Maeder, A., & Meynet, G. 2011, ArXiv e-prints, arXiv:1109.6171 [astro-ph.SR]
Maeder, A., & Meynet, G. 2015, in IAU Symposium, Vol. 307, IAU Symposium, ed. G. Meynet, C. Georgy, J. Groh, & P. Stee, 9
Marcy, G. W., Isaacson, H., Howard, A. W., et al. 2014, ApJS, 210, 20
Marigo, P., & Aringer, B. 2009, A&A, 508, 1539
Marigo, P., Girardi, L., Bressan, A., et al. 2008, A&A, 482, 883
Martínez-Aldama, M. L., Dultzin, D., Marziani, P., et al. 2014, Advances in Space Research, 54, 1375
Martins, F., & Palacios, A. 2013, A&A, 560, A16
Massey, P. 2013, New A Rev., 57, 14
Maxted, P. F. L., O'Donoghue, D., Morales-Rueda, L., Napiwotzki, R., & Smalley, B. 2007, MNRAS, 376, 919
Melis, C., Reid, M. J., Mioduszewski, A. J., Stauffer, J. R., & Bower, G. C. 2014, Science, 345, 1029
Metcalfe, T., Creevey, O., Dogan, G., et al. 2014, arXiv, arXiv:1402.3614
Meynet, G., & Maeder, A. 1997, A&A, 321, 465
Meynet, G., & Maeder, A. 2000, A&A, 361, 101
Meynet, G., Chomienne, V., Ekström, S., et al. 2015, A&A, 575, A60
Mihalas, D. 1978, Stellar atmospheres /2nd edition/ (W. H. Freeman and Co.)
Mihalas, D., Hummer, D. G., Mihalas, B. W., & Daeppen, W. 1990, ApJ, 350, 300
Milone, A. P., Piotto, G., Bedin, L. R., et al. 2012, ApJ, 744, 58
Mokiem, M. R., de Koter, A., Vink, J. S., et al. 2007, A&A, 473, 603
Morales, J. C., Torres, G., Marschall, L. A., & Brehm, W. 2009a, ApJ, 707, 671
Morales, J. C., Ribas, I., Jordi, C., et al. 2009b, ApJ, 691, 1400
Muijres, L. E., Vink, J. S., de Koter, A., Müller, P. E., & Langer, N. 2012a, A&A, 537, A37
Muijres, L., Vink, J. S., de Koter, A., et al. 2012b, A&A, 546, A42
Munakata, H., Kohyama, Y., & Itoh, N. 1985, ApJ, 296, 197
Nanni, A., Bressan, A., Marigo, P., & Girardi, L. 2013, MNRAS, 434, 2390
Nanni, A., Bressan, A., Marigo, P., & Girardi, L. 2014, MNRAS, 438, 2328
Navarro, J. F., Frenk, C. S., & White, S. D. M. 1996, ApJ, 462, 563
Nefs, S. V., Birkby, J. L., Snellen, I. A. G., et al. 2013, MNRAS, 431, 3240
Niederhofer, F., Georgy, C., Bastian, N., & Ekström, S. 2015, ArXiv e-prints, arXiv:1507.07561 [astro-ph.SR]
Nikolaev, S., & Weinberg, M. D. 2000, ApJ, 542, 804
Noebauer, U. M., & Sim, S. A. 2015, ArXiv e-prints, arXiv:1508.03644 [astro-ph.SR]
Noels, A. 2015, ArXiv e-prints, arXiv:1507.03387 [astro-ph.SR]
Nugis, T., & Lamers, H. J. G. L. M. 2000, A&A, 360, 227
Oey, M. S., & Clarke, C. J. 2007, ArXiv Astrophysics e-prints, astro-ph/0703036
Ofir, A., Gandolfi, D., Buchhave, L., et al. 2012, MNRAS, 423, L1
Owocki, S. 2013, Stellar Winds, ed. T. D. Oswalt & M. A. Barstow (Springer), 735
Parsons, S. G., Marsh, T. R., Gänsicke, B. T., et al. 2012a, MNRAS, 420, 3281
Parsons, S. G., Gänsicke, B. T., Marsh, T. R., et al. 2012b, MNRAS, 426, 1950
Parsons, S. G., Marsh, T. R., Gänsicke, B. T., et al. 2012c, MNRAS, 419, 304
Pauldrach, A., Puls, J., & Kudritzki, R. P. 1986, A&A, 164, 86
Paxton, B., Bildsten, L., Dotter, A., et al. 2011, ApJS, 192, 3
Peng, C. Y., Ho, L. C., Impey, C. D., & Rix, H.-W. 2002, AJ, 124, 266
Pietrinferni, A., Cassisi, S., Salaris, M., & Castelli, F. 2004, ApJ, 612, 168
Pietrinferni, A., Molinaro, M., Cassisi, S., et al. 2014, Astronomy and Computing, 7, 95
Plez, B. 2011, Journal of Physics Conference Series, 328, 012005

Pont, F., Bouchy, F., Melo, C., et al. 2005a, A&A, 438, 1123
Pont, F., Melo, C. H. F., Bouchy, F., et al. 2005b, A&A, 433, L21
Pont, F., Moutou, C., Bouchy, F., et al. 2006, A&A, 447, 1035
Postman, M., Coe, D., Benítez, N., et al. 2012, ApJS, 199, 25
Puls, J., Springmann, U., & Lennon, M. 2000, A&AS, 141, 23
Puls, J., Vink, J. S., & Najarro, F. 2008, A&A Rev., 16, 209
Quintana, E. V., Barclay, T., Raymond, S. N., et al. 2014, Science, 344, 277
Rajpurohit, A. S., Reylé, C., Allard, F., et al. 2013, A&A, 556, A15
Randich, S., Sestito, P., Primas, F., Pallavicini, R., & Pasquini, L. 2006, A&A, 450, 557
Rayner, J. T., Cushing, M. C., & Vacca, W. D. 2009, ArXiv e-prints, arXiv:0909.0818 [astro-ph.SR]
Richer, H. B., Dotter, A., Hurley, J., et al. 2008, AJ, 135, 2141
Rogers, F. J., & Nayfonov, A. 2002, ApJ, 576, 1064
Rogers, F. J., Swenson, F. J., & Iglesias, C. A. 1996, ApJ, 456, 902
Ryan, Jr., R. E., McCarthy, P. J., Cohen, S. H., et al. 2012, ApJ, 749, 53
Salaris, M., & Weiss, A. 1998, A&A, 335, 943
Salasnich, B., Bressan, A., & Chiosi, C. 1999, A&A, 342, 131
Sánchez-Blázquez, P., Peletier, R. F., Jiménez-Vicente, J., et al. 2006, MNRAS, 371, 703
Sandberg Lacy, C. H., Torres, G., Wolf, M., & Burks, C. L. 2014, AJ, 147, 1
Sander, A., Hamann, W.-R., & Todt, H. 2012, A&A, 540, A144
Sandquist, E. L. 2004, MNRAS, 347, 101
Sarajedini, A., Dotter, A., & Kirkpatrick, A. 2009, ApJ, 698, 1872
Sarajedini, A., Bedin, L. R., Chaboyer, B., et al. 2007, AJ, 133, 1658
Sarangi, A., & Cherchneff, I. 2015, A&A, 575, A95
Saumon, D., Chabrier, G., & van Horn, H. M. 1995, ApJS, 99, 713
Schaerer, D., Hayes, M., Verhamme, A., & Teyssier, R. 2011, A&A, 531, A12
Schmutz, W., Leitherer, C., & Gruenwald, R. 1992, PASP, 104, 1164
Schneider, R., Ferrara, A., & Salvaterra, R. 2004, MNRAS, 351, 1379
Schwarzschild, M. 1958, Structure and evolution of the stars (Princeton University Press)
Scoville, N., Aussel, H., Brusa, M., et al. 2007, ApJS, 172, 1
Sérsic, J. L. 1963, Boletin de la Asociacion Argentina de Astronomia La Plata Argentina, 6, 41
Shen, S., Mo, H. J., White, S. D. M., et al. 2003, MNRAS, 343, 978
Siegel, M. H., Majewski, S. R., Reid, I. N., & Thompson, I. B. 2002, ApJ, 578, 151
Skrutskie, M. F., Cutri, R. M., Stiening, R., et al. 2006, AJ, 131, 1163
Smith, L. F., & Maeder, A. 1991, A&A, 241, 77
Smith, N. 2009, in Massive Stars: From Pop III and GRBs to the Milky Way, ed. M. Livio & E. Villaver, Space Telescope Science Institute Symposium Series No. 20 (Cambridge University Press), 187
Smith, N. 2014, ARA&A, 52, 487
Smith, N., & Owocki, S. P. 2006, ApJ, 645, L45
Sobolev, V. V. 1960, Moving envelopes of stars (Cambridge: Harvard University Press)
Somers, G., & Pinsonneault, M. H. 2015, ArXiv e-prints, arXiv:1506.01393 [astro-ph.SR]
Spada, F., Demarque, P., Kim, Y.-C., & Sills, A. 2013, ApJ, 776, 87
Spruit, H. C. 2013, A&A, 552, A76
Spruit, H. C., & Weiss, A. 1986, A&A, 166, 167
Straniero, O., Chieffi, A., & Limongi, M. 1997, ApJ, 490, 425
Szomoru, D., Franx, M., & van Dokkum, P. G. 2012, ApJ, 749, 121
Tal-Or, L., Mazeh, T., Alonso, R., et al. 2013, A&A, 553, A30
Tang, J., Bressan, A., Rosenfield, P., et al. 2014, MNRAS, 445, 4287
Tassoul, J.-L. 2000, Stellar Rotation (Cambridge University Press)
Taylor, M. B. 2006, in Astronomical Society of the Pacific Conference Series, Vol. 351, Astronomical Data Analysis Software

and Systems XV, ed. C. Gabriel, C. Arviset, D. Ponz, & S. Enrique, 666
Torres, G., Andersen, J., & Giménez, A. 2010, A&A Rev., 18, 67
Torres, G., Vaz, L. P. R., Sandberg Lacy, C. H., & Claret, A. 2014, AJ, 147, 36
Vaccaro, T. R., Rudkin, M., Kawka, A., et al. 2007, ApJ, 661, 1112
van der Wel, A., Bell, E. F., Häussler, B., et al. 2012, ApJS, 203, 24
van Leeuwen, F. 2009, A&A, 497, 209
van Loon, J. T., Cioni, M.-R. L., Zijlstra, A. A., & Loup, C. 2005, A&A, 438, 273
VandenBerg, D. A., Edvardsson, B., Eriksson, K., & Gustafsson, B. 2008a, ApJ, 675, 746
VandenBerg, D. A., Edvardsson, B., Eriksson, K., & Gustafsson, B. 2008b, ApJ, 675, 746
VandenBerg, D. A., & Stetson, P. B. 2004, PASP, 116, 997
Vink, J. S., de Koter, A., & Lamers, H. J. G. L. M. 2000, A&A, 362, 295
Vink, J. S., de Koter, A., & Lamers, H. J. G. L. M. 2001, A&A, 369, 574
Vink, J. S., & Gräfener, G. 2012, ApJ, 751, L34
Vink, J. S., Muijres, L. E., Anthonisse, B., et al. 2011, A&A, 531, A132
Wang, P. F., Chen, W. P., Lin, C. C., et al. 2014, ArXiv e-prints, arXiv:1401.7424 [astro-ph.SR]
Watkins, L. L., van der Marel, R. P., Bellini, A., & Anderson, J. 2015, ArXiv e-prints, arXiv:1509.00513
Wright, E. L., Eisenhardt, P. R. M., Mainzer, A. K., et al. 2010, AJ, 140, 1868
Yadav, R. K. S., Bedin, L. R., Piotto, G., et al. 2008, A&A, 484, 609
Yu, N., Wang, J.-J., & Li, N. 2015, MNRAS, 446, 2566
Zasowski, G., Johnson, J. A., Frinchaboy, P. M., et al. 2013, AJ, 146, 81
Zaussinger, F., & Spruit, H. C. 2013, A&A, 554, A119
Zemskova, V., Garaud, P., Deal, M., & Vauclair, S. 2014, ApJ, 795, 118
Zentner, A. R., & Hearin, A. P. 2011, Phys. Rev. D, 84, 101302
Zhou, G., Bayliss, D., Hartman, J. D., et al. 2014, MNRAS, 437, 2831
Zirm, A. W., Toft, S., & Tanaka, M. 2012, ApJ, 744, 181
Zola, S., Şenavcı, H. V., Liakos, A., Nelson, R. H., & Zakrzewski, B. 2014, MNRAS, 437, 3718